F ´ S

Institut de Physique des Hautes Énergies

$B^0\overline{B}^0$ mixing measurement at Belle using dilepton events tagged with a soft pion

Thèse de Doctorat

présentée à la Faculté des Sciences
de l'Université de Lausanne

par

Frédéric Ronga

Physicien diplômé
de l'Université de Lausanne

Jury

P^{r} Jean H, président
P^{r} Olivier S, directeur de thèse
P^{r} Kazuo A, expert externe
P^{r} Thomas S, expert interne

LAUSANNE
2003

UNIVERSITE DE LAUSANNE

Faculté des sciences

Imprimatur

Vu le rapport présenté par le jury d'examen, composé de

Président	Monsieur	Prof.	Jean **Hernandez**
Directeur de thèse	Monsieur	Prof.	Olivier **Schneider**
Rapporteur			
Experts	Monsieur	Prof.	Kazuo **Abe**
	Monsieur	Prof.	Thomas **Schietinger**

le Conseil de Faculté autorise l'impression de la thèse de

Monsieur Frédéric Ronga

Physicien diplômé de l'Université de Lausanne

intitulée

$B^0\,\overline{B}^0$ mixing measurement at Belle using dilepton events tagged with a soft pion

Lausanne, le 21 novembre 2003

Le Doyen de la Faculté des Sciences

Prof. Jean Hernandez

Abstract

THE Belle experiment is located in the KEK research centre (Japan) and is primarily devoted to the study of CP violation in the B meson sector. Belle is placed on the KEKB collider, one of the two currently running "B meson factories", which produce $B\overline{B}$ pairs. KEKB has created more than 150 million pairs in total, a world record for this kind of colliders. This large sample allows very precise measurements in the physics of beauty mesons. The present analysis falls within the framework of these precise measurements.

One of the most remarkable phenomena in high-energy physics is the ability of weak interactions to couple a neutral meson to its anti-meson. In this work, we study the B^0–$\overline{B}^0$ meson coupling, which induces an oscillation of frequency Δm_d we can measure accurately. Besides the interest of this phenomenon itself, this measurement plays an important role in the quest for the origin of CP violation. The standard model of electro-weak interactions does not include CP violation in a fully satisfactory way. The search for yet unexplained physical phenomena is, therefore, the main motivation of the Belle collaboration.

Many measurements of Δm_d have previously been performed. The present work, however, leads to a precision on Δm_d that has never been reached before. This is the result of the excellent performance of KEKB, and of an original approach that allows a considerable reduction of background contamination from unwanted events. This approach was already successfully used by other collaborations, in slightly different conditions than here.

The method we employed consists in the partial reconstruction of one of the B mesons through the decay channel $B^0 \to D^*(D^0\pi)\,\ell\,\nu_\ell$, where only the information on the lepton ℓ and the pion π is used. The information on the other B meson of the initial $B\overline{B}$ pair is extracted from a single high-energy lepton. The available sample of $B^0\overline{B}^0$ pairs thus does not suffer from large reductions due to complete reconstructions, nor does it suffer from large charged B mesons background, as in fully inclusive analyses.

We finally obtain the following result on the 150 million pairs:

$$\Delta m_d = 0.513 \pm 0.006 \pm 0.008 \text{ ps}^{-1},$$

where the first error is statistical, and the second systematic.

Résumé

L'EXPÉRIENCE Belle, située dans le centre de recherche du KEK, au Japon, est consacrée principalement à l'étude de la violation de CP dans le système des mésons B. Elle est placée sur le collisionneur KEKB, qui produit des paires $B\overline{B}$. KEKB, l'une des deux « usines à B » actuellement en fonction, détient le record du nombre d'événements produits avec plus de 150 millions de paires. Cet échantillon permet des mesures d'une grande précision dans le domaine de la physique du méson B. C'est dans le cadre de ces mesures de précision que s'inscrit cette analyse.

L'un des phénomènes remarquables de la physique des hautes énergies est la faculté qu'a l'interaction faible de coupler un méson neutre avec son anti-méson. Dans le présent travail, nous nous intéressons au méson B^0 couplé au méson $\overline{B}^0$, avec une fréquence d'oscillation Δm_d mesurable précisément. Outre la beauté de ce phénomène lui-même, une telle mesure trouve sa place dans la quête de l'origine de la violation de CP. Cette dernière n'est incluse que d'une façon peu satisfaisante dans le modèle standard des interactions électro-faibles. C'est donc la recherche de phénomènes physiques encore inexpliqués qui motive en premier lieu la collaboration Belle.

Il existe déjà de nombreuses mesures de Δm_d antérieures. Celle que nous présentons ici est cependant d'une précision encore jamais atteinte grâce, d'une part, à l'excellente performance de KEKB et, d'autre part, à une approche originale qui permet de réduire considérablement la contamination de la mesure par des événements indésirés. Cette approche fut déjà mise à profit par d'autres expériences, dans des conditions quelque peu différentes de celles de Belle.

La méthode employée consiste à reconstruire partiellement l'un des mésons dans le canal $B^0 \to D^*(D^0\pi)\,\ell\,\nu_\ell$ en n'utilisant que les informations relatives au lepton ℓ et au pion π. L'information concernant l'autre méson de la paire $B\overline{B}$ initiale n'est tirée que d'un seul lepton de haute énergie. Ainsi, l'échantillon à disposition ne souffre pas de grandes réductions dues à une reconstruction complète, tandis que la contamination due aux mésons B chargés est fortement diminuée en comparaison d'une analyse inclusive.

Nous obtenons finalement le résultat suivant sur les 150 millions de paires :

$$\Delta m_d = 0.513 \pm 0.006 \pm 0.008 \text{ ps}^{-1},$$

la première erreur étant l'erreur statistique et la deuxième, l'erreur systématique.

Remerciements

J'aimerais tout d'abord exprimer ma profonde gratitude envers le professeur Olivier Schneider qui m'a dirigé durant ce travail de thèse avec toute la rigueur scientifique qui font sa renommée, avec une disponibilité que son cahier des charges ne laisserait pas présager ! Mes remerciements vont ensuite au Docteur Jean-Pierre Perroud, à qui fut laissé le soin de m'éduquer dans mes premières années de thèse. J'y ai énormément appris en peu de temps ; ceux qui l'ont côtoyé ne s'en étonneront pas. Le professeur Aurelio Bay, directeur de l'IPHE, y est aussi pour beaucoup, et je l'en remercie.

Je souhaite également adresser de vifs remerciements au professeur Kazuo Abe, qui fut à la source de ce sujet de thèse et qui m'a suivi avec beaucoup de paternalisme, ainsi qu'au professeur Thomas Schietinger, dont les commentaires et encouragements ont été pour beaucoup dans la finalisation de ce travail.

Mes séjours japonais m'ont fait travailler avec des gens du monde entier. Il me faut en particulier remercier Nick Hastings, maître des dileptons, et le professeur Yoshihide Sakai. Que soient aussi remerciés, dans le désordre, Tim Gershon, Soeren Lange et Ichiro Adachi.

Le plus clair de mon temps, je l'ai cependant passé au sixième étage du BSP. J'aimerais remercier ici Olivier Dormond, que je quitte après dix ans de parcours commun, Patrick Koppenburg, pionnier des boursiers lausannois au Japon, et Luc Hinz, mon compagnon de route au pays du soleil levant.

L'ambiance si chaleureuse de l'IPHE ne serait pas la même si ses chevilles ouvrières, Erika Lüthi, Monique Romaniszin et Marianne Chave, n'y travaillaient pas. Que tous les habitants de cet étage, des doctorants aux professeurs honoraires, qui contribuent à en faire une famille accueillante, reçoivent ici mes plus vifs remerciements.

Enfin, pour leur soutien affectif, administratif et même parfois scientifique, j'aimerais adresser mes remerciements à mes parents et à Joëlle.

Contents

Introduction **1**

1 The theoretical framework **5**

1.1 $B^0 - \overline{B}^0$ mixing 5

1.1.1 CPT invariance 6

1.1.2 CP invariance 7

1.1.3 Time evolution 7

1.2 Mixing in the Standard Model 8

1.2.1 The CKM Matrix 8

1.2.2 Mixing amplitudes 9

1.2.3 Standard Model predictions 10

1.3 Semi-leptonic B meson decays at $\Upsilon(4S)$ 11

1.3.1 Correlated B meson pairs 11

1.3.2 Flavour-specific decays 12

2 The experimental apparatus **15**

2.1 B-factories 15

2.1.1 The $\Upsilon(4S)$ resonance 15

2.1.2 The asymmetric KEKB collider 17

2.2 The Belle Detector 20

2.2.1 Beam pipe and silicon vertex detector 20

2.2.2 The central drift chamber 22

2.2.3 Aerogel Cherenkov counter 26

2.2.4 Time-of-flight counters 26

2.2.5 Electromagnetic calorimeter 27

2.2.6 K-long and muon detector . . . 29
2.2.7 Extreme forward calorimeter . . . 30
2.3 Trigger . . . 31
2.4 Data acquisition and data processing . . . 32
2.4.1 Data acquisition . . . 32
2.4.2 Level-4 filter . . . 33
2.4.3 Full reconstruction . . . 33
2.5 Detector simulation . . . 35

3 Reconstruction **37**
3.1 Partial reconstruction . . . 38
3.1.1 Extraction of the missing mass squared . . . 38
3.1.2 Generator study . . . 39
3.2 Event selection and reconstruction . . . 40
3.2.1 Data set . . . 44
3.2.2 Event preselection . . . 46
3.2.3 Event selection . . . 47
3.2.4 Particle identification . . . 49
3.2.5 First lepton selection . . . 52
3.2.6 Soft pion selection . . . 52
3.2.7 Lepton-pion pair selection . . . 53
3.2.8 Second lepton selection . . . 53
3.2.9 Dilepton selection . . . 56
3.2.10 Δz measurement . . . 57
3.2.11 Selection result . . . 57

4 Fit design and results **59**
4.1 Event classification . . . 60
4.1.1 Definitions . . . 60
4.1.2 Fractions of categories . . . 61
4.1.3 Missing mass squared fit . . . 63
4.2 Time evolution . . . 65
4.3 Detector response function . . . 67
4.3.1 Detector resolution . . . 67
4.3.2 Non-primary decays . . . 68

4.3.3 Response function 71
4.4 List of likelihood terms 72
4.4.1 Same-sign events 72
4.4.2 Opposite-sign events 78
4.5 Corrections to the Monte Carlo 79
4.5.1 Branching fractions 80
4.5.2 Lepton and pion momentum distributions 80
4.6 Summary and results 80
4.6.1 Consistency check 82
4.6.2 Fit result 83
4.6.3 Additional checks 83
4.7 Systematic errors 90
4.7.1 Physics parameters 90
4.7.2 Detector resolution 90
4.7.3 Non-primary decays 91
4.7.4 Event fractions 92
4.7.5 Summary 92
4.8 Discussion of the result 94

Conclusion **99**

A The Micromegas detector **101**
A.1 The micromesh gaseous structure 101
A.2 Breakdown study 104
A.2.1 Experimental setup 104
A.2.2 Model of breakdown mechanism 105
A.2.3 Highly ionising particles and discharges 107
A.2.4 Detection efficiency 109
A.3 Conclusion 110

Bibliography **112**

Introduction

MORE than twenty years ago, the *Standard Model of electro-weak interactions* earned a Nobel Prize to S. Glashow, A. Salam and S. Weinberg. This model is still used to describe most of the interactions between elementary particles, in particular those responsible for *mixing*. Precisely measuring mixing, therefore, offers a way to improve this model, or perhaps disprove it. We shall explain this in more detail here, as simply as possible.

The Standard Model

The model of Glashow, Salam and Weinberg is part of a more general 'standard model' used in particle physics to help answer two fundamental questions about matter: "What is matter made of?" and "How does it hold together?".

It was already discovered a long time ago that atoms are not elementary: they are made of electrons, protons and neutrons. As far as physicists know today, electrons are elementary particles and belong to a family of six *leptons* (λέπτον means "light" in Greek). Protons and neutrons, however, are composite particles made of elementary bricks we call *quarks*.

Quarks and leptons may be classified according to their charge and mass. Because nature seems to like order and symmetry, they appear in three "generations" of increasing mass, as shown in Table 1 on the following page. In addition, for each lepton or quark there exist an anti-lepton or an anti-quark with same mass and opposite charge. Altogether, this represents 24 elementary bricks of matter.

Quarks appear either by triplets or in association with an anti-quark. Composite particles made of three quarks are called *baryons* (βάρυς means "heavy" in Greek), while the combination of a quark and an anti-quark is a *meson*. These combinations allow an amazing variety of particles. For example, the proton is made of two u quarks and one d quark, whereas the neutron is made of one u quark and two d quarks.

TABLE 1 – *Elementary constituents of matter.*

	Charge	*Particles*			*Anti-particles*			*Charge*	
Quarks	$+\frac{2}{3}$	u	c	t	$\overline{u}$	$\overline{c}$	$\overline{t}$	$-\frac{2}{3}$	*Anti-quarks*
	$-\frac{1}{3}$	d	s	b	$\overline{d}$	$\overline{s}$	$\overline{b}$	$+\frac{1}{3}$	
Leptons	-1	e^-	μ^-	τ^-	e^+	μ^+	τ^+	$+1$	*Anti-leptons*
	0	ν_e	ν_μ	ν_τ	$\overline{\nu}_e$	$\overline{\nu}_\mu$	$\overline{\nu}_\tau$	0	

There are four interactions holding things together: gravity, electromagnetism, strong force and weak force. These forces are enabled by the exchange of mediator particles, the *intermediate bosons*. The strong force, which binds quarks together, is mediated by gluons. The charged bosons W^+ and W^-, and the neutral boson Z^0 mediate weak interactions, which mainly appear in nuclear decays. The electromagnetic force, which appears in everyday-life phenomena, is mediated by photons. Finally, gravity may be mediated by gravitons, yet to be observed. Table 2 gives the list of interactions and corresponding mediators.

TABLE 2 – *Fundamental interactions.*

Interaction	*Mediator*
Gravitation	Graviton G
Electromagnetism	Photon γ
Weak force	$W^\pm$ and Z^0
Strong force	Gluons g

Mixing and weak interaction

Weak interaction is of paramount importance in this work. Contrary to all other interactions, it may couple quarks of different generations. The quark t, for instance, may "decay" weakly into a quark d, although it preferentially decays to a b. This phenomenon is called *quark mixing*.

As already mentioned, quarks never come alone. In the case of neutral mesons, quark mixing has remarkable consequences. Let us consider for example the neutral B meson, made of one d and one anti-b: $B^0 = (d\overline{b})$. Thanks to weak interaction, the B^0 is coupled to its anti-particle, made of one anti-d and one b: $\overline{B}^0 = (\overline{d}b)$. This leads to a particle–anti-particle oscillation. As a result, we cannot measure the mass of the B^0 or the $\overline{B}^0$ alone, but rather the mass of mixtures of B^0 and $\overline{B}^0$. Oscillation then gives birth to two states of definite mass, but with mixed quark content. The mass difference between these two states, we write Δm_d, proves to be equal to the frequency of this oscillation.

Δm_d, the quantity we measure in this work, is thus linked to one of the most puzzling features of weak interactions.

CP violation

There is yet another striking feature of weak interactions we must mention here. Table 1 on the facing page shows how important symmetries are in physics. One of the most fundamental symmetries one could expect to see in nature is the particle–anti-particle symmetry. It seems, indeed, that $\overline{B}^0$ is called an *anti*-B^0 by mere convention. At a macroscopic level, however, we know that matter, which is made of particles, completely dominates over anti-matter, made of anti-particles.

The operation that mathematically transforms a particle into its anti-particle is called “CP”. The observed asymmetry between matter and anti-matter requires violation of CP by some physical process. And, indeed, it was observed, a few decades ago, that weak interactions do not conserve CP [1].

In the Standard Model, CP violation is accommodated by a mathematical object called the *CKM matrix*. Since it is the only place that holds such an important phenomenon as CP violation, the CKM matrix is one of the favourite probes of the Standard Model. Precise measurements of its elements may shed light on the origin of CP violation, by revealing new physical phenomena.

The measurement of Δm_d enters this “quest” for CP violation in a two-fold way: first, as an input for many precise measurements of CP-violating processes; second, because Δm_d is directly related to one of the CKM elements that primarily include CP violation.

About this work

This work was achieved within the Belle collaboration. The Belle detector, located at the KEKB collider in Tsukuba (Japan), is mainly devoted to the study of CP violation in the B meson sector. KEKB produces pairs of $B^0\overline{B}^0$ mesons at a rate never reached before, thus providing an outstanding environment for B physics, including CP violation and mixing.

Several techniques have already been used to measure Δm_d at Belle[1]. They fall into two categories, namely *inclusive* and *exclusive* reconstructions of B mesons. The former

[1] See [2] for a review of measurements at Belle

category includes the dilepton analysis, which is well-known for its unsurpassable amount of statistics. The dilepton analysis, however, suffers from significant systematic uncertainties due to a large background contribution, whereas exclusive analyses have a much better background rejection, but also a much smaller amount of available data.

There is hope to purify the dilepton sample while retaining many of its nice features. The total semi-leptonic branching fraction of the neutral B meson is 10.5% (electron or muon), of which 36% obey the following cascade:

$$\begin{aligned} B^0 \longrightarrow D^{*-}\, \ell^+\, \nu_\ell & \\ D^{*-} \longrightarrow \overline{D}^0\, \pi^- & \end{aligned} \tag{1}$$

The charged pion has a very low momentum in the D^* rest frame, so its measured 4-momentum can be used to calculate an approximate 4-momentum of the D^*. Because no similar decay exists at first order for charged B mesons, this soft pion "tag" allows a great reduction of the charged B background. This method was first used in time-integrated mixing studies by the CLEO collaboration in 1983; it was then applied by the B B collaboration to time-dependent mixing measurements, which remained at a preliminary stage (see References [3–6]). This work, however, was performed on a much larger sample of neutral B mesons, thanks to KEKB's excellent operation.

We first introduce the theoretical framework underlying mixing measurements (Chapter 1). The experimental tools are described in Chapter 2. The last two chapters mainly describe the contribution of the author, namely, event reconstruction and extraction of Δm_d from the data. The results are finally summarised and discussed.

Addendum

There has been a long way from Lausanne to Tsukuba. More than half of this way was spent among the LHCb collaboration at Cern, in the development of the "inner tracker" of the LHCb experiment. This very enriching work is briefly presented in Appendix A.

> La preuve scientifique [...] s'affirme dans l'expérience aussi bien que dans le raisonnement, à la fois dans un contact avec la réalité et dans une référence à la raison.
>
> — G. Bachelard, *Le nouvel esprit scientifique*, Introduction

Chapter 1

The theoretical framework

THE theoretical tools necessary to understand the experimental results of this work are introduced in this chapter. We first give the formalism of particle mixing in quantum mechanics. Predictions in the context of the Standard Model are then given and applied to the analysis method used here[1].

Ὥστε ἐι πᾶσα διάνοια ἤ πρακτική ἠ ποιητικὴ
ἢ ϑεωρητική, ἡ φυσικὴ ϑεωρητική τις ἂν ἔιη.

— Aristotle, *Metaphysics*, 1025b

1.1 $B^0 - \overline{B}^0$ mixing

The $|B_d^0\rangle$ and $|\overline{B}_d^0\rangle$ states of neutral B mesons are eigenstates of the strong and electromagnetic interactions, with definite flavour content. Since both interactions conserve flavour, oscillation from one state to the other can only occur through weak interactions, which are also responsible for the decay of B_d^0 and $\overline{B}_d^0$.

The time evolution of a general state $|\psi(t)\rangle$ is greatly simplified if one uses the Wigner–Weisskopf approximations[2]: the initial state is a pure combination of $|B_d^0\rangle$ and $|\overline{B}_d^0\rangle$; time-dependent decay rates to common final states are disregarded; the time scale is much higher

[1]This chapter is mainly based on References [7–9]

[2]Developed for the calculation of natural line width in light emission by atoms [10, 11].

than the typical strong-interaction scale. The wave function describing the $B_d^0 - \overline{B}_d^0$ system then takes the following form:

$$|\psi(t)\rangle = a(t)|B_d^0\rangle + b(t)|\overline{B}_d^0\rangle \tag{1.1}$$

and satisfies the simplified Schrödinger equation:

$$\imath\frac{\partial}{\partial t}\begin{pmatrix} a(t) \\ b(t) \end{pmatrix} = \mathbf{R}\cdot\begin{pmatrix} a(t) \\ b(t) \end{pmatrix}. \tag{1.2}$$

Because of the above approximations, the 2×2 matrix $\mathbf{R}$ is not hermitian. It may, however, be written in terms of a dispersive and an absorptive part:

$$\mathbf{R} = \mathbf{M} - \frac{\imath}{2}\mathbf{\Gamma}, \tag{1.3}$$

where $\mathbf{M}$, the mass matrix, and $\mathbf{\Gamma}$, the decay matrix, are hermitian. Virtual intermediate states contribute to $\mathbf{M}$, while physical decay channels common to B_d^0 and $\overline{B}_d^0$ contribute to $\mathbf{\Gamma}$.

1.1.1 CPT invariance

CPT invariance follows from very general properties of quantum field theory, such as Lorentz invariance. It is therefore usually assumed that CPT is a good symmetry of nature. On this assumption the diagonal elements of $\mathbf{M}$ and $\mathbf{\Gamma}$ are equal, and Equation (1.2) becomes:

$$\imath\frac{\partial}{\partial t}\begin{pmatrix} a(t) \\ b(t) \end{pmatrix} = \left[\begin{pmatrix} M_d & M_{12} \\ M_{12}^* & M_d \end{pmatrix} - \frac{\imath}{2}\begin{pmatrix} \Gamma_d & \Gamma_{12} \\ \Gamma_{12}^* & \Gamma_d \end{pmatrix}\right]\cdot\begin{pmatrix} a(t) \\ b(t) \end{pmatrix}. \tag{1.4}$$

The eigenvalues of the effective Hamiltonian $\mathbf{R}$ are then given by:

$$\lambda_\pm = \left(M_d - \frac{\imath}{2}\Gamma_d\right) \pm \frac{q}{p}\left(M_{12} - \frac{\imath}{2}\Gamma_{12}\right), \tag{1.5}$$

with the corresponding physical eigenstates:

$$|B_\pm\rangle = p|B_d^0\rangle \pm q|\overline{B}_d^0\rangle, \tag{1.6}$$

where the coefficients obey the normalisation $|p|^2 + |q|^2 = 1$. Since the $|B_\pm\rangle$ states have definite mass, they can be labelled $|B_H\rangle$ for the heavier state and $|B_L\rangle$ for the lighter one. We then define:

$$\Delta m_d = m_H - m_L, \quad m = \frac{m_H + m_L}{2} \tag{1.7}$$

$$\Delta\Gamma_d = \Gamma_H - \Gamma_L, \quad \Gamma = \frac{\Gamma_H + \Gamma_L}{2}. \tag{1.8}$$

With these conventions, we have:

$$\frac{q}{p} = \sqrt{\frac{M_{12}^* - \frac{\imath}{2}\Gamma_{12}^*}{M_{12} - \frac{\imath}{2}\Gamma_{12}}} \tag{1.9}$$

Δm_d and $\Delta\Gamma_d$ are also related to the off-diagonal matrix elements:

$$\begin{aligned} \Delta m_d{}^2 - \frac{1}{4}\Delta\Gamma_d^2 &= 4\,|M_{12}|^2 - |\Gamma_{12}|^2 & (1.10)\\ \Delta m_d\,\Delta\Gamma_d &= -4\mathcal{R}\left(M_{12}\Gamma_{12}^*\right) & (1.11)\end{aligned}$$

1.1.2 CP invariance

The CP operation transforms $|B_d^0\rangle$ into $|\overline{B}_d^0\rangle$:

$$\begin{aligned} \mathcal{CP}|B_d^0\rangle &= e^{\imath\xi}|\overline{B}_d^0\rangle & (1.12)\\ \mathcal{CP}|\overline{B}_d^0\rangle &= e^{-\imath\xi}|B_d^0\rangle, & (1.13)\end{aligned}$$

where ξ is an arbitrary phase. CP conservation implies $M_{12}^* = e^{2\imath\xi}M_{12}$ and $\Gamma_{12}^* = e^{2\imath\xi}\Gamma_{12}$, or, from Equation (1.9):

$$\left|\frac{q}{p}\right|^2 = 1 \tag{1.14}$$

In other words, CP violation in the mixing may be quantified by the difference:

$$1 - \left|\frac{q}{p}\right|^2, \tag{1.15}$$

which vanishes if CP is conserved.

1.1.3 Time evolution

The time evolution of the mass eigenstates is simply given by:

$$|B_{H/L}(t)\rangle = e^{-\imath m_{H/L}t}e^{-\Gamma_{H/L}t/2}|B_{H/L}\rangle. \tag{1.16}$$

From this equation and Equation (1.6) on the preceding page we get the time evolution of initially pure (tagged) $|B_d^0\rangle$ and $|\overline{B}_d^0\rangle$ states:

$$\begin{aligned} |B_d^0(t)\rangle &= g_+(t)|B_d^0\rangle + \frac{q}{p}g_-(t)|\overline{B}_d^0\rangle \\ |\overline{B}_d^0(t)\rangle &= g_+(t)|\overline{B}_d^0\rangle + \frac{p}{q}g_-(t)|B_d^0\rangle & (1.17)\end{aligned}$$

where:

$$g_{\pm}(t) = \frac{1}{2}\left(e^{-\imath\lambda_{+}t} \pm e^{-\imath\lambda_{-}t}\right). \tag{1.18}$$

The time-dependent mixing probability is then given by:

$$\begin{aligned}\left|\langle B_d^0|\overline{B}_d^0(t)\rangle\right|^2 &= \left|\frac{p}{q}\right|^2 |g_{-}(t)|^2 = \left|\frac{p}{q}\right|^2 \frac{e^{-\Gamma t}}{2}\left[\cosh\left(\frac{\Delta\Gamma_d}{2}t\right) - \cos(\Delta m_d\, t)\right] \\ &= \left|\frac{q}{p}\right|^4 \left|\langle \overline{B}_d^0|B_d^0(t)\rangle\right|^2, \end{aligned} \tag{1.19}$$

while the probability of remaining unchanged values:

$$\left|\langle B_d^0|B_d^0(t)\rangle\right|^2 = |g_{+}(t)|^2 = \frac{e^{-\Gamma t}}{2}\left[\cosh\left(\frac{\Delta\Gamma_d}{2}t\right) + \cos(\Delta m_d\, t)\right] = \left|\langle \overline{B}_d^0|\overline{B}_d^0(t)\rangle\right|^2. \tag{1.20}$$

1.2 Mixing in the Standard Model

1.2.1 The CKM Matrix

Quark mixing is accommodated in the framework of the Standard Model by the Cabibbo–Kobayashi–Maskawa (CKM) unitary matrix [12, 13], which connects the weak eigenstates (d', s', b') to the corresponding mass eigenstates:

$$\begin{pmatrix} d' \\ s' \\ b' \end{pmatrix} = \underbrace{\begin{pmatrix} V_{ud} & V_{us} & V_{ub} \\ V_{cd} & V_{cs} & V_{cb} \\ V_{td} & V_{ts} & V_{tb} \end{pmatrix}}_{\equiv \hat{V}_{\mathrm{CKM}}} \begin{pmatrix} d \\ s \\ b \end{pmatrix}. \tag{1.21}$$

The charged current has the following form:

$$J^W = W_\mu^+ (\overline{u}, \overline{c}, \overline{t})\gamma^\mu \hat{V}_{\mathrm{CKM}} \begin{pmatrix} d \\ s \\ b \end{pmatrix} + W_\mu^- (\overline{d}, \overline{s}, \overline{b})\gamma^\mu \hat{V}^\dagger_{\mathrm{CKM}} \begin{pmatrix} u \\ c \\ t \end{pmatrix} \tag{1.22}$$

The unitary condition and an appropriate choice of relative quark fields phases reduce the parameters of $\hat{V}_{\mathrm{CKM}}$ to three angles and one phase. The most commonly used parameterisation, introduced by L. Wolfenstein [14], expresses the matrix elements in terms of powers of $\lambda = |V_{us}| \approx 0.22$:

$$\hat{V}_{\mathrm{CKM}} = \begin{pmatrix} 1-\frac{1}{2}\lambda^2 & \lambda & A\lambda^3(\rho - \imath\eta) \\ -\lambda & 1-\frac{1}{2}\lambda^2 & A\lambda^2 \\ A\lambda^3(1-\rho-\imath\eta) & -A\lambda^2 & 1 \end{pmatrix} + O\left(\lambda^4\right). \tag{1.23}$$

From the expression of the charged current (1.22) on the facing page, it can be derived that CP conservation in quark weak interactions requires all elements of $\hat{V}_{\mathrm{CKM}}$ to be real. In other words, CP violation may occur in the Standard Model if and only if there exist irreducible complex phases in the CKM matrix. Historically, the third generation of quark was exactly introduced by Kobayashi and Maskawa to allow for CP violation in the Standard Model. The above parameterisation shows that, up to the order λ^3, V_{td} and V_{ub} are responsible for CP violation[3].

1.2.2 Mixing amplitudes

In the Standard Model, $B_d^0 - \overline{B}_d^0$ mixing is described at lowest order by box diagrams involving up-type quark loops (see Figure 1.1). The contributions from the three different quark types are quantified by $\lambda_\alpha = V_{\alpha b}^* V_{\alpha d}$, where α is up, charm or top. The unitarity of the CKM matrix implies:

$$\lambda_u + \lambda_c + \lambda_t = 0. \tag{1.24}$$

This relation can be used to replace up-quark loops contributions in terms of charm and top quarks contributions, assuming $m_u = 0$. Further, we can use the fact that $m_t \sim m_W \gg m_c$ to neglect functions of m_c^2/m_W^2. The dispersive part of the box diagrams, which corresponds

[3]This is not true at higher orders. For example, V_{ts} also contributes at order λ^4.

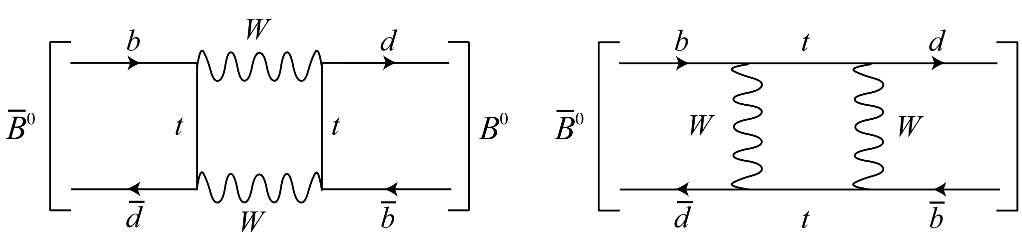

FIGURE 1.1 – *Dominant box diagrams for $B_d^0 - \overline{B}_d^0$ oscillations. Other diagrams have u or c quarks instead of t.*

to M_{12}, then reduces to:

$$\begin{aligned} M_{12} &\approx \frac{G_F^2 m_W^2}{4\pi^2}\langle B_d^0|(\overline{d}\gamma^\mu\gamma_L b)(\overline{d}\gamma_\mu\gamma_L b)|\overline{B}_d^0\rangle \eta_B S_0\left(m_t^2/m_W^2\right)\left(V_{tb}V_{td}^*\right)^2 \\ &= -\frac{G_F^2 m_W^2 m_B B_B f_B^2}{12\pi^2}\eta_B S_0\left(m_t^2/m_W^2\right)\left(V_{tb}V_{td}^*\right)^2 \end{aligned} \tag{1.25}$$

where G_F is the Fermi coupling constant, m_W the W boson mass, and $m_B = M_d$ the B_d^0 mass. The "bag parameter" B_B is a correction factor to account for QCD corrections in the loops. The weak decay constant f_B is related to the creation of a B_d^0 from the vacuum and is defined by:

$$\langle 0|\overline{d}\gamma^\mu\gamma_L b|B_d^0(E,\vec{p})\rangle = -\imath p^\mu f_B \tag{1.26}$$

with $p = (E, \vec{p})$. The coefficient η_B accounts for QCD corrections in the initial and final states, i.e., the fact that box diagrams couple $b\overline{d}$ and $d\overline{b}$ instead of B_d^0 and $\overline{B}_d^0$. Finally, S_0 is a known function of the reduced mass $x_t^2 = m_t^2/m_W^2$.

1.2.3 Standard Model predictions

Let us now consider the absorptive part of the box diagrams, Γ_{12}. Only up and charm quark loops contribute to Γ_{12}, since it corresponds to transitions to physical states into which both B_d^0 and $\overline{B}_d^0$ may decay. As a result, the value of the absorptive part must be dominated by the available mass, $m_B \approx m_b$. Since $M_{12} \propto S_0 \propto m_t^2$, we obtain the following prediction in the framework of the Standard Model:

$$\left|\frac{\Gamma_{12}}{M_{12}}\right| \sim \frac{m_b^2}{m_t^2} \sim 10^{-3}. \tag{1.27}$$

Combining this equation with Equation (1.11) on page 7, we can write:

$$\Delta m_d \approx 2\,|M_{12}| \propto (V_{tb}V_{td}^*)^2, \tag{1.28}$$

where clearly appears the link between the mixing parameter, Δm_d, and one of the favourite probes for CP violation in the Standard Model, V_{td}.

Finally, the decay rate difference becomes:

$$\Delta\Gamma_d \approx \frac{2\mathcal{R}(M_{12}^*\Gamma_{12})}{|M_{12}|} \ll \Delta m_d. \tag{1.29}$$

and by expanding the CP-violating parameter (1.15) on page 7 in powers of $|q/p|^2$ we get:

$$1 - \left|\frac{q}{p}\right|^2 \approx \mathcal{I}\left(\frac{\Gamma_{12}}{M_{12}}\right) \sim \mathcal{O}(10^{-4}). \tag{1.30}$$

From now on, we will assume that $\Delta\Gamma = 0$ and CP is conserved in the mixing. Under these assumptions, Equations (1.17) to (1.20) on pages 7–8 become:

$$
\begin{aligned}
|B_d^0(t)\rangle &= g_+(t)|B_d^0\rangle + g_-(t)|\overline{B}_d^0\rangle \\
|\overline{B}_d^0(t)\rangle &= g_+(t)|\overline{B}_d^0\rangle + g_-(t)|B_d^0\rangle \qquad (1.31)\\
g_\pm(t) &= \frac{1}{2}e^{-\frac{\Gamma}{2}t}\left(e^{-\imath m_H t} \pm e^{-\imath m_L t}\right) \qquad (1.32)\\
\mathcal{P}(B_d^0 \to \overline{B}_d^0; t) &= \mathcal{P}(\overline{B}_d^0 \to B_d^0; t) = \frac{e^{-\Gamma t}}{2}\left[1 - \cos(\Delta m_d\, t)\right] \equiv \mathcal{P}^{\mathrm{mix}}(t) \qquad (1.33)\\
\mathcal{P}(B_d^0 \to B_d^0; t) &= \mathcal{P}(\overline{B}_d^0 \to \overline{B}_d^0; t) = \frac{e^{-\Gamma t}}{2}\left[1 + \cos(\Delta m_d\, t)\right] \equiv \mathcal{P}^{\mathrm{unm}}(t) \qquad (1.34)
\end{aligned}
$$

1.3 Semi-leptonic *B* meson decays at $\Upsilon(4S)$

In the present work, we study B mesons produced by the KEKB collider (see Chapter 2) through the decay of the $\Upsilon(4S)$ resonance. The $\Upsilon(4S)$ resonance is a $b\overline{b}$ bound state of quantum numbers $J^{PC} = 1^{--}$. B meson pairs produced through the (strong) decay of $\Upsilon(4S)$ then appear in a correlated, antisymmetric wave function Φ^-.

1.3.1 Correlated *B* meson pairs

At initial time, we have:

$$|\Phi^-\rangle = \frac{1}{\sqrt{2}}\left[|B_d^0\rangle \otimes |\overline{B}_d^0\rangle - |\overline{B}_d^0\rangle \otimes |B_d^0\rangle\right]. \qquad (1.35)$$

The terms $|B_d^0\rangle \otimes |B_d^0\rangle$ and $|\overline{B}_d^0\rangle \otimes |\overline{B}_d^0\rangle$ are forbidden by the Bose–Einstein symmetry. This antisymmetry is preserved at any time by the linearity of oscillation. In other words, one B meson is at any time the charged-conjugate of the other B meson.

The amplitude for one B meson decaying at time t_1 into the final state f_1, and the other B meson decaying at time t_2 into the final state f_2 is:

$$\langle f_1, t_1; f_2, t_2|T|\Phi^-\rangle = \frac{1}{\sqrt{2}}\left\{\langle f_1, t_1|T|B_d^0\rangle\langle f_2, t_2|T|\overline{B}_d^0\rangle - \langle f_1, t_1|T|\overline{B}_d^0\rangle\langle f_2, t_2|T|B_d^0\rangle\right\}, \qquad (1.36)$$

where T is the transition matrix. We define:

$$A_{f_1} = \langle f_1|T|B_d^0\rangle, \qquad \overline{A}_{f_1} = \langle f_1|T|\overline{B}_d^0\rangle, \tag{1.37}$$

$$A_{f_2} = \langle f_2|T|B_d^0\rangle, \qquad \overline{A}_{f_2} = \langle f_2|T|\overline{B}_d^0\rangle, \tag{1.38}$$

$$a_- = \overline{A}_{f_1}\overline{A}_{f_2} - A_{f_1}A_{f_2}, \qquad b_- = A_{f_1}\overline{A}_{f_2} - \overline{A}_{f_1}A_{f_2} \tag{1.39}$$

Then, using Equation (1.31) on the previous page, we get:

$$\begin{aligned}\langle f_1, t_1; f_2, t_2|T|\Phi^-\rangle = \frac{1}{\sqrt{2}}\Big\{ & a_- \left[g_-(t_1)g_+(t_2) + g_+(t_1)g_-(t_2)\right] \\ & + b_- \left[g_-(t_1)g_+(t_2) + g_+(t_1)g_-(t_2)\right]\Big\},\end{aligned} \tag{1.40}$$

and the decay rate is proportional to:

$$\begin{aligned}\left|\langle f_1, t_1; f_2, t_2|T|\Phi^-\rangle\right|^2 = e^{-\Gamma(t_1+t_2)} \Bigg[& \frac{|a_- + b_-|^2 + |a_- - b_-|^2}{8} \\ & + \frac{|b_-|^2 - |a_-|^2}{4}\cos(\Delta m_d\,\Delta t) \\ & + \frac{\mathcal{I}(a_- b_-^*)}{2}\sin(\Delta m_d\,\Delta t)\Bigg],\end{aligned} \tag{1.41}$$

where $\Delta t = t_1 - t_2$. Since $t_1 + t_2$ is usually not measurable, we integrate over it and get [15]:

$$\begin{aligned}\left|\langle f_1; f_2; \Delta t|T|\Phi^-\rangle\right|^2 = \frac{e^{-\Gamma|\Delta t|}}{2\Gamma} \Bigg[& \frac{|a_- + b_-|^2 + |a_- - b_-|^2}{8} + \frac{|b_-|^2 - |a_-|^2}{4}\cos(\Delta m_d\,\Delta t) \\ & + \frac{\mathcal{I}(a_- b_-^*)}{2}\sin(\Delta m_d\,\Delta t)\Bigg].\end{aligned} \tag{1.42}$$

1.3.2 Flavour-specific decays

In the case of B mesons decaying semi-leptonically, the charge of the lepton unequivocally identifies the flavour of the B meson it comes from (see Figure 1.2).

Let us first consider the case where the B mesons both decay into positively charged leptons. We have the following

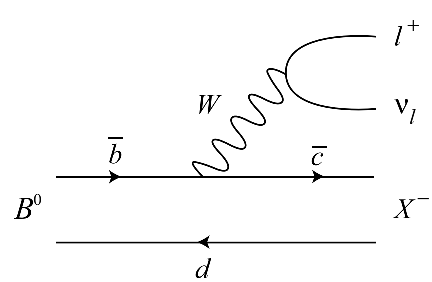

FIGURE 1.2 – *Semi-leptonic decay* $B^0 \to X^-\ell^+\nu_\ell$

decay amplitudes:

$$A_{f_1} = \langle X^-\ell^+|T|B_d^0\rangle = A_{\ell^+}, \quad \overline{A}_{f_1} = \langle X^-\ell^+|T|\overline{B}_d^0\rangle = 0, \tag{1.43}$$
$$A_{f_2} = \langle X^-\ell^+|T|B_d^0\rangle = A_{\ell^+}, \quad \overline{A}_{f_2} = \langle X^-\ell^+|T|\overline{B}_d^0\rangle = 0, \tag{1.44}$$
$$\Rightarrow a_- = -A_{\ell^+}^2, \quad b_- = 0, \tag{1.45}$$

which, replacing into (1.42) on the facing page, leads to the decay rate:

$$\Gamma_{\Upsilon(4S)\to\ell^+\ell^+}(\Delta t) \propto \frac{|A_{\ell^+}|^4}{8\Gamma} e^{-\Gamma|\Delta t|}\left[1 - \cos\left(\Delta m_d\, \Delta t\right)\right]. \tag{1.46}$$

Similarly, for B mesons decaying into negatively charged leptons:

$$A_{f_1} = \langle X^+\ell^-|T|B_d^0\rangle = 0, \quad \overline{A}_{f_1} = \langle X^-\ell^+|T|\overline{B}_d^0\rangle = A_{\ell^-}, \tag{1.47}$$
$$A_{f_2} = \langle X^+\ell^-|T|B_d^0\rangle = 0, \quad \overline{A}_{f_2} = \langle X^-\ell^+|T|\overline{B}_d^0\rangle = A_{\ell^-}, \tag{1.48}$$
$$\Rightarrow a_- = A_{\ell^-}^2, \quad b_- = 0, \tag{1.49}$$

and:

$$\Gamma_{\Upsilon(4S)\to\ell^-\ell^-}(\Delta t) \propto \frac{|A_{\ell^+}|^4}{8\Gamma} e^{-\Gamma|\Delta t|}\left[1 - \cos\left(\Delta m_d\, \Delta t\right)\right]. \tag{1.50}$$

Assuming that there is no direct CP violation in semi-leptonic decays, we have $\mathcal{B}(B^0 \to X^-l^+\nu_l) = \mathcal{B}(\overline{B}^0 \to X^+l^-\overline{\nu}_l)$, i.e. $|A_{\ell^+}| = |A_{\ell^-}| \equiv |A_\ell|$. The total decay rate for same-flavour events is then given by:

$$\Gamma_{\Upsilon(4S)\to\ell^\pm\ell^\pm}(\Delta t) \propto \frac{|A_\ell|^4}{4\Gamma} e^{-\Gamma|\Delta t|}\left[1 - \cos\left(\Delta m_d\, \Delta t\right)\right]. \tag{1.51}$$

Let us now consider the cases where the produced leptons have opposite charge. The two possible cases are:

$$A_{f_1} = \langle X^-\ell^+|T|B_d^0\rangle = A_\ell, \quad \overline{A}_{f_1} = \langle X^-\ell^+|T|\overline{B}_d^0\rangle = 0, \tag{1.52}$$
$$A_{f_2} = \langle X^+\ell^-|T|B_d^0\rangle = 0, \quad \overline{A}_{f_2} = \langle X^+\ell^-|T|\overline{B}_d^0\rangle = A_\ell, \tag{1.53}$$
$$\Rightarrow a_- = 0, \quad b_- = A_\ell^2, \tag{1.54}$$

and:

$$A_{f_1} = \langle X^+\ell^-|T|B_d^0\rangle = 0, \quad \overline{A}_{f_1} = \langle X^+\ell^-|T|\overline{B}_d^0\rangle = A_\ell, \tag{1.55}$$
$$A_{f_2} = \langle X^-\ell^+|T|B_d^0\rangle = A_\ell, \quad \overline{A}_{f_2} = \langle X^-\ell^+|T|\overline{B}_d^0\rangle = 0, \tag{1.56}$$
$$\Rightarrow a_- = 0, \quad b_- = -A_\ell^2. \tag{1.57}$$

Combining the two, we get the total decay rate for opposite-flavour events:

$$\Gamma_{\Upsilon(4S)\to\ell^\pm\ell^\mp}(\Delta t) \propto \frac{|A_\ell|^4}{4\Gamma} e^{-\Gamma|\Delta t|} \left[1 + \cos\left(\Delta m_d\, \Delta t\right)\right]. \tag{1.58}$$

Thus, the probabilities for having a same-flavour (SF) or an opposite-flavour (OF) event, as a function of Δt, are given by:

$$\mathcal{P}^{\mathrm{SF/OF}}(\Delta t) = \frac{\exp\left(\frac{-|\Delta t|}{\tau_0}\right)}{4\tau_0} \left[1 \mp \cos(\Delta m_d\, \Delta t)\right], \tag{1.59}$$

where $\tau_0 = 1/\Gamma$ is the B_d^0 lifetime. We finally define the integrated mixing probability χ_d:

$$\chi_d = \frac{x_d^2}{2(1+x_d^2)}, \quad \text{with} \quad x_d = \Delta m_d \tau_0 \tag{1.60}$$

Chapter 2

The experimental apparatus

HIGH energy physics analyses make use of various tools, from the accelerator to the detection devices and the software environment. In this work, they are called *KEKB*, *Belle* and *BASF*. We summarise here their main characteristics.

2.1 *B*-factories

There has been a long way from the first observation of a $b\bar{b}$ resonance by the CFS collaboration in 1977 [16] to the production of more than 10 $B\overline{B}$ pairs per second at KEK in 2003. This major achievement was made possible by the discovery of an other bound state of bottom quarks called $\Upsilon(4S)$.

2.1.1 The $\Upsilon(4S)$ resonance

The resonance discovered at Fermilab, $\Upsilon(9460)$, was the first of a series of "bottomonium" systems. Figure 2.1 on the next page shows the total electron-positron annihilation cross-section as a function of the centre-of-mass energy. The three first resonances are very narrow: their width on this figure is largely dominated by the energy resolution. The last one, the $\Upsilon(4S)$, is significantly broader because it lies just 20 MeV above the threshold of B mesons production, where the suppression of hadronic decays by the OZI rule does not hold anymore [17]. Masses and widths of Υ mesons are summarised in Table 2.1. Heavier resonances have been discovered.

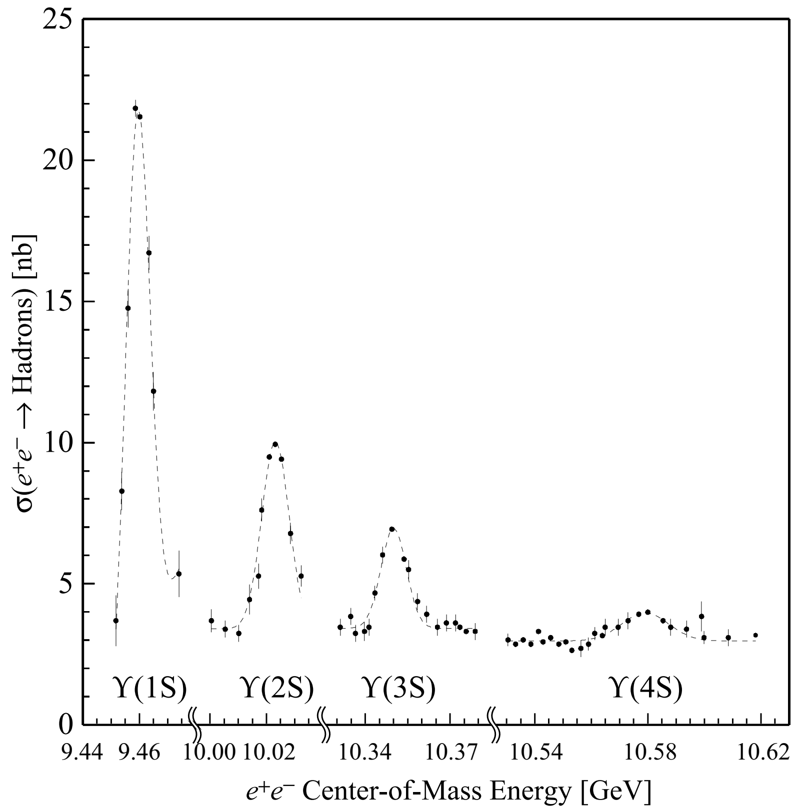

Figure 2.1 – *Cross-section of e^+e^- into hadrons measured by CLEO and CUSB (from [18]). The series of $b\bar{b}$ resonances are clearly visible.*

Table 2.1 – *Masses and widths of the Υ resonances [19].*

Meson	*Mass [GeV]*	*Width [MeV]*
$\Upsilon(1S)$	9.46030±0.00026	0.0530 ±0.0015
$\Upsilon(2S)$	10.02326±0.00031	0.043 ±0.006
$\Upsilon(3S)$	10.3552 ±0.0005	0.0263 ±0.0034
$\Upsilon(4S)$	10.5800 ±0.0035	14 ±5

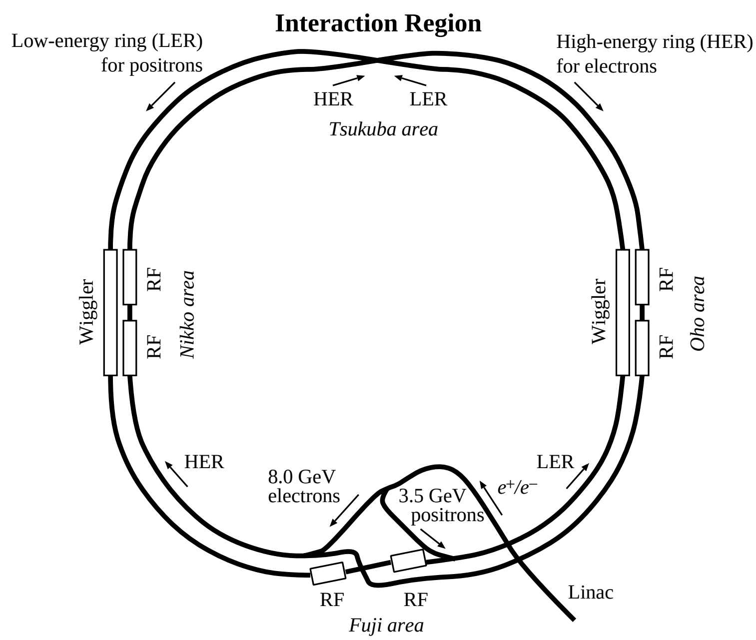

FIGURE 2.2 – *Configuration of the KEKB accelerator system.*

The $\Upsilon(4S)$ is a spin 1 $b\bar{b}$ bound state of parity -1 and mass 10.58 GeV. It decays into $B\overline{B}$ pairs more than 96% of the time, with a partial width ratio $\Gamma(B^+B^-)/\Gamma(B^0\overline{B}^0)$ of 1.04 ± 0.07 [19]. In other words, $\Upsilon(4S)$ produces neutral and charged B mesons almost exclusively and in equal quantities. This feature was first exploited by the CLEO and ARGUS collaborations using the "*B*-factories" CESR and DORIS in the late seventies.

The $\Upsilon(4S)$, however, only accounts for one fourth of the total electron-positron cross-section, as can be seen on Figure 2.1 on the facing page; most collisions produce pairs of lighter quarks u, d, s or c. The resulting events are designated as *continuum* events.

2.1.2 The asymmetric KEKB collider

The *KEKB B-Factory Design Report* [20] was published in June 1995. The construction started in 1994 already and was completed in November 1998. Commissioning then began in December of the same year.

As shown on Figure 2.2, KEKB consists of two storage rings: one high-energy ring (HER) containing electrons of 8.0 GeV, and one low-energy ring (LER) containing positrons of 3.5 GeV. The two 3-kilometres long rings are fed by a linear accelerator. The total energy

TABLE 2.2 – *Main parameters of the KEKB asymmetric collider on May 13, 2003 (luminosity record).*

	LER	HER	
Beam current	1377	1050	mA
Crossing angle	± 11		mrad
Beta functions at IP β_x^*/β_y^*	59/0.58	58/0.7	cm
Estimated σ_y^* at IP	2.2	2.2	μm
Number of bunches	1284		
Bunch spacing	2.4		m
Beam lifetime	127@1377	256@1050	min.@mA
Luminosity	10.567		$\times 10^{33}$ cm^{-2}s^{-1}

in the centre-of-mass system is:

$$\sqrt{s} = \sqrt{4E_{\text{HER}}E_{\text{LER}}} = 10.58 \text{ GeV} \tag{2.1}$$

which exactly corresponds to the $\Upsilon(4S)$ mass.

Hence, in contrast with previous B-factories already mentioned, KEKB collides electrons and positrons at a unequal energies. As a consequence of this asymmetry, the $\Upsilon(4S)$ centre-of-mass experiences a boost $\beta\gamma$ with respect to the laboratory:

$$\beta\gamma = \frac{E_{\text{HER}} - E_{\text{LER}}}{\sqrt{s}} = 0.425 \tag{2.2}$$

Because of this boost, B mesons produced by the decay of the $\Upsilon(4S)$ travel along the beam direction before decaying, thus allowing time-dependent analyses in spite of the short B meson lifetime. With this value of $\beta\gamma$, the average path length of a B meson is 200 μm. The chosen value of the boost is a compromise between the detector acceptance and the vertex separation needed to distinguish the two mesons. Studies have shown that the required integrated luminosity for observing CP violation is minimal for $\beta\gamma$ between 0.4 and 0.9 [20, chapter 1].

The number of B mesons produced each second is given by the product of the hadronic cross-section σ and the luminosity $\mathcal{L}$. The maximum σ is reached by operating the collider at the centre of the $\Upsilon(4S)$ resonance, where $\sigma = 1.1$ nb. Energy scans were performed to find this maximum. The design luminosity of KEKB is $\mathcal{L} = 10^{34}$ cm^{-2}s^{-1}. It was achieved

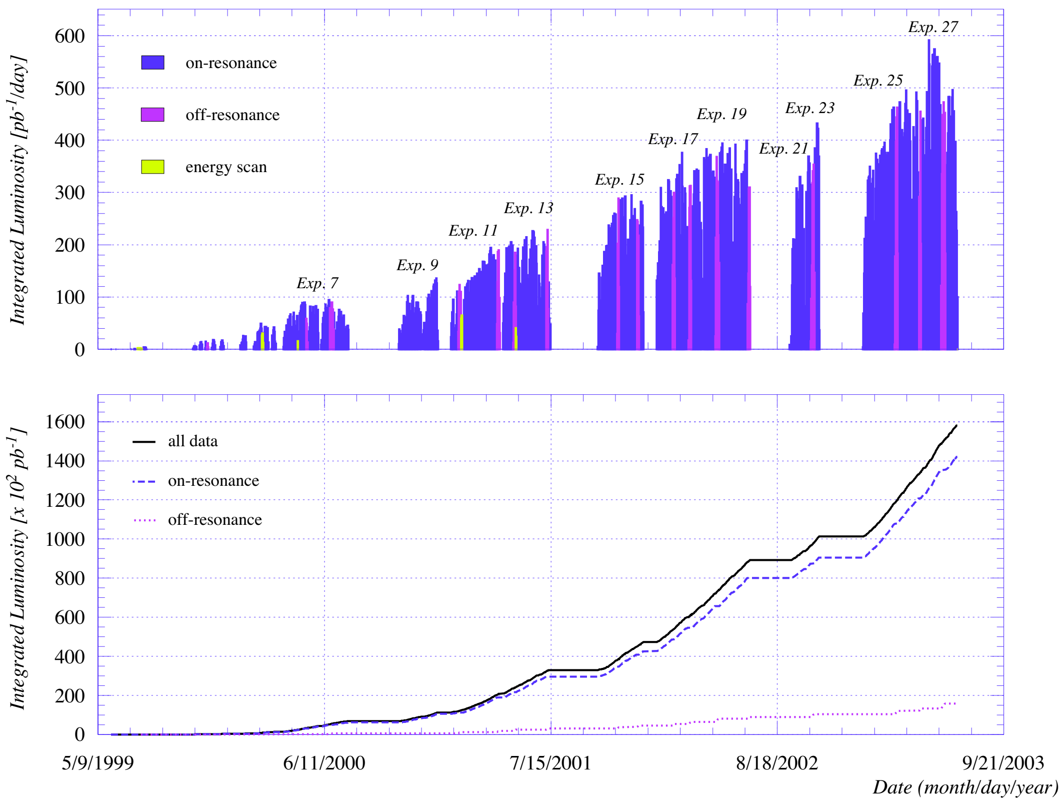

FIGURE 2.3 – *History of KEKB's luminosity. The integrated luminosity per day (top) and total integrated luminosity (bottom) are shown. Run periods are also indicated.*

during May 2003, thanks to large beam currents and small beam sizes, two salient features of KEKB.

Another feature of KEKB is the fact that the beams do not collide head-on, but at a small angle $\theta = 22$ mrad. The resulting reduction of the luminosity with respect to a head-on collision is compensated by the reduction of beam-beam interactions. In addition, the interaction region design is greatly simplified by this configuration and final-focus quadrupoles can be placed relatively far from the collision point.

Finally, KEKB also operates off-resonance, about 60 MeV below the $\Upsilon(4S)$ peak (more than four standard deviations away from the resonance). The data collected off-resonance is used to study continuum events.

Table 2.2 on the facing page summarises the main parameters of KEKB. Run periods, referred to as "experiments", are represented in Figure 2.3.

2.2 The Belle Detector

"Belle" means "beautiful" in French. It is also the concatenation of "B" (for B meson) with the palindrome "elle" (for electron – anti-electron). A suitable name for an experiment devoted to B physics and running at a positron-electron collider!

The configuration of the Belle detector is shown in Figure 2.4 on the facing page. The detector is a toroidal apparatus surrounding the interaction region [21]. A superconducting solenoidal magnet immerses the device in a 1.5 Tesla field. A silicon vertex detector (SVD) measures the position of B meson decays. A wire drift chamber (the central drift chamber—CDC) provides charged particles tracking and dE/dx information. Kaons and charged pions are discriminated using an aerogel Cherenkov counter (ACC). Time-of-flight (TOF) counters give further information for particle identification. An electromagnetic calorimeter (ECL) collects electromagnetic showers produced by electrons and photons. Muons and long-lived neutral kaons are detected in arrays of resistive plate counters (KLM) inserted throughout the iron yoke. Finally, a pair of BGO crystal arrays (the extreme forward calorimeter—EFC) covers the small-angle region in the forward and backward directions.

The standard coordinate system is defined in the following way:

- the x axis is in the horizontal plane and points outward from the ring;
- the y axis is vertical;
- the z axis is anti-parallel to the low-energy beam so that lower-momentum particles are aligned with the magnetic field.

The azimuthal angle ϕ and the polar angle θ with respect to the z axis are also used. Finally, the radial distance is defined by $r = \sqrt{x^2 + y^2}$.

The following sections give a brief description of the various detector subsystems listed above.

2.2.1 Beam pipe and silicon vertex detector

The beam pipe separates the vacuum region of the rings from the detection region (see Figure 2.5 on the next page). It is made of a thin double-wall cylinder of Beryllium in order to minimise multiple Coulomb scattering, the main limiting factor on the determination of decay vertexes positions. The small gap between the 0.5 mm walls is filled with a continuous flow of gaseous helium. This ensures an active cooling of the walls, which

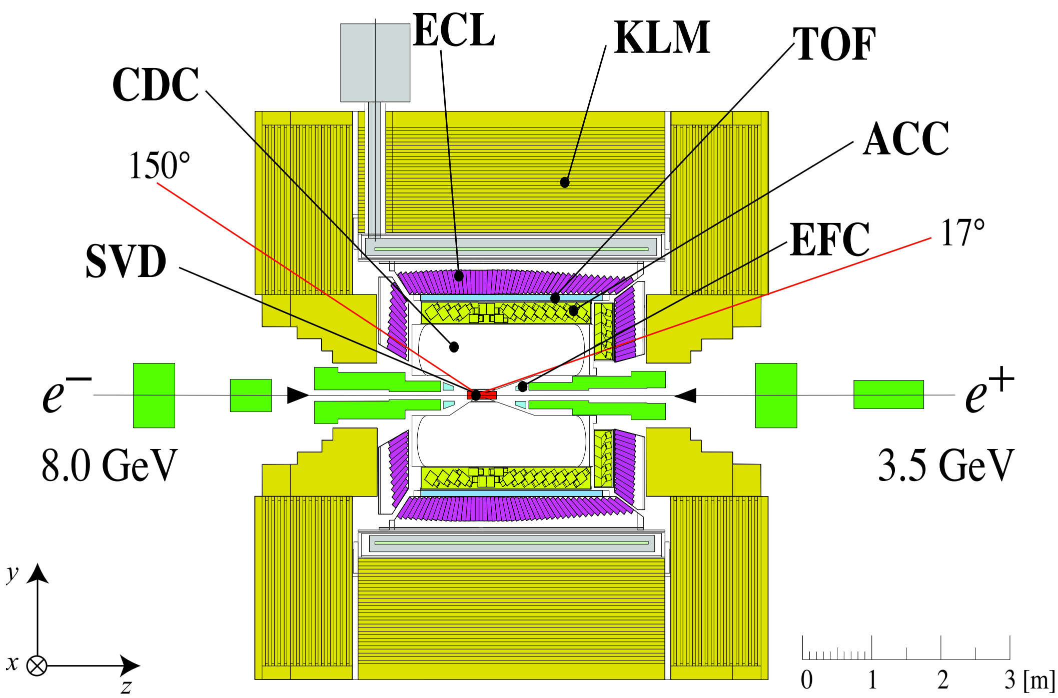

FIGURE 2.4 – *Side view of the Belle detector showing the various sub-detectors and the standard coordinate system.*

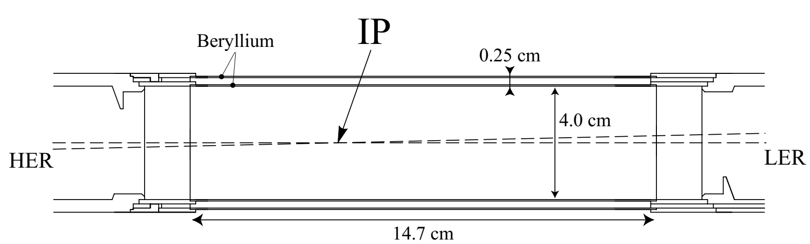

FIGURE 2.5 – *Schematic picture of the beam pipe.*

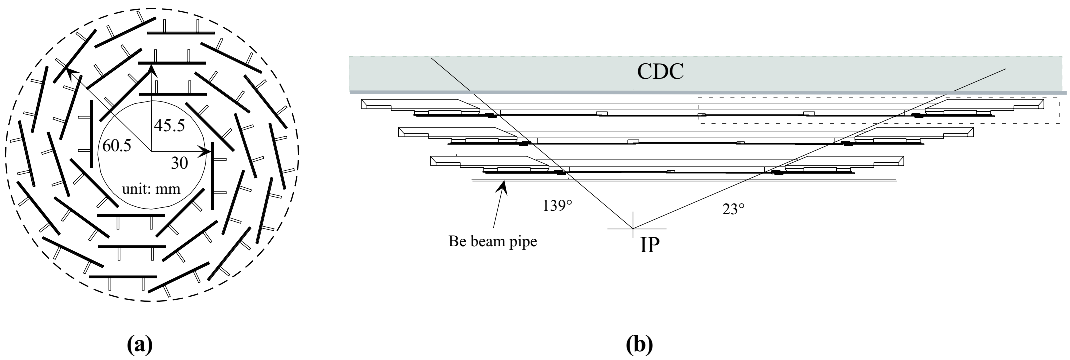

Figure 2.6 – *The silicon vertex detector: (a) cross-section view and (b) side view.*

endure beam-induced heating of the order of 100 W. The first layer of the vertex detector can therefore be put as close as possible to the interaction point (IP), thus allowing better precision on the vertex position measurement.

As its name suggests, the vertex detector is designed for precise measurements of the decay vertex position of primary particles, i.e., in our case, B mesons travelling along the z axis. It also helps tracking decay particles.

The configuration of the vertex detector around the beam pipe is shown on Figure 2.6. It consists of three layers arranged on a cylindrical structure at 30 mm, 45.5 mm and 60.5 mm from the interaction point. It covers the region $23° < \theta < 139°$, which corresponds to 86 % of the full solid angle. Layers are made of 8, 10 and 14 "ladders" respectively. Each ladder is divided into two electronically independent parts containing one (for short ladders) or two (for long ladders) double-sided silicon strip detectors (DSSDs).

A DSSD has 1280 strips and 640 read-out pads on each side, each second strip being read out. Charge collected on floating strips is determined through capacitive charge division on adjacent strips. The n-side of the DSSD has strips along the beam axis to measure z, with a strip pitch of 42 μm. ϕ strips are located on the p-side and have a pitch of 25 μm. Each side of the DSSD is read out by five 128-channel integrated circuits mounted on ceramic hybrids. The overall size of a DSSD is 57.5×33.5 mm^2.

More details can be found in [22].

2.2.2 The central drift chamber

The central drift chamber (CDC) is the core part of the tracking system. It provides essential information for the reconstruction of charged particle tracks and the determination

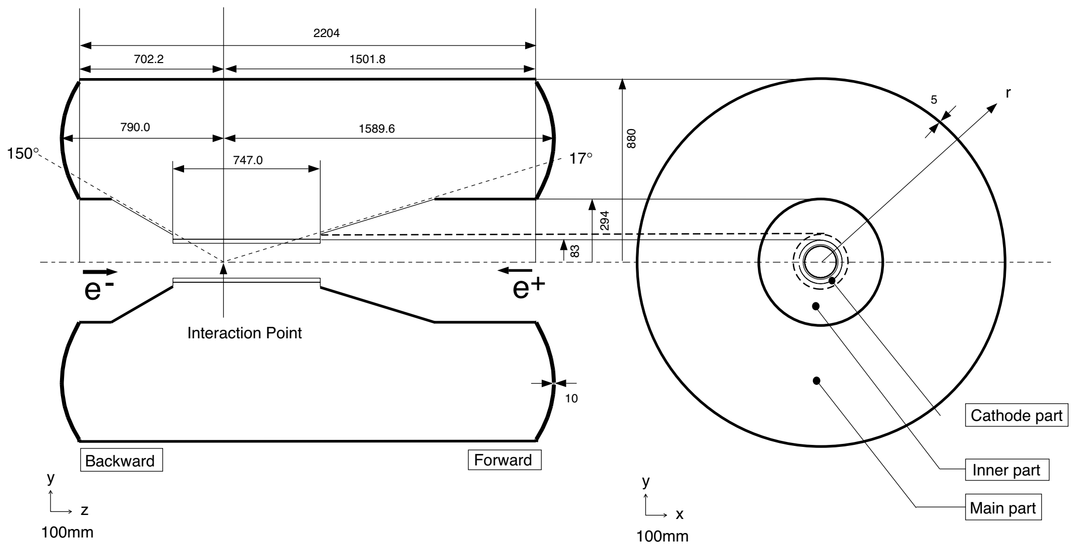

FIGURE 2.7 – *Overview of the CDC structure. Lengths are in millimetres.*

of their momenta. In addition, the energy loss (dE/dx) can be determined to help identify charged particles.

The structure of the CDC is shown on Figure 2.7. It has an asymmetric shape along z, in order to cope with the asymmetry of the beams, and covers $17° < \theta < 150°$ (about 92% of the full solid angle). It is a cylindrical wire drift chamber filled with a mixture of 50% helium and 50% ethane gas, chosen to minimize multiple scattering and provide good dE/dx resolution.

The chamber contains 50 layers of anode wires (32 axial and 18 small-angle-stereo) in the inner and main parts, and three cathode strip layers in the cathode part. It has a total of 8400 drift cells made of six field wires and one sense wire (see Figure 2.8 on the following page). Axial wires provide information in the bending plane to determine the transverse momentum $p_\perp$. Stereo wires used in conjunction with axial layers provide information on the z coordinate. Cathode strips are set along the ϕ direction and therefore greatly improve the z coordinate measurement. They are however only used as a fast trigger because of the higher background near to the beam.

Charged particles moving in a magnetic field follow the path of a helix. The track is then defined by five parameters [23]: the slope of the helix axis, the (signed) curvature and the position of the helix with respect to a reference point, the “pivot”. These parameters are first determined in the CDC. The pivot is chosen as the wire position of the innermost hit

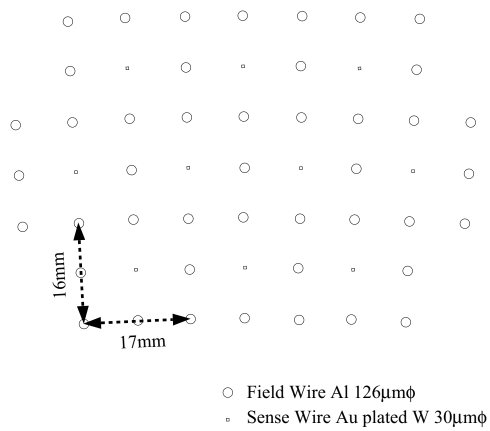

Figure 2.8 – *Structure of a drift cell in the CDC.*

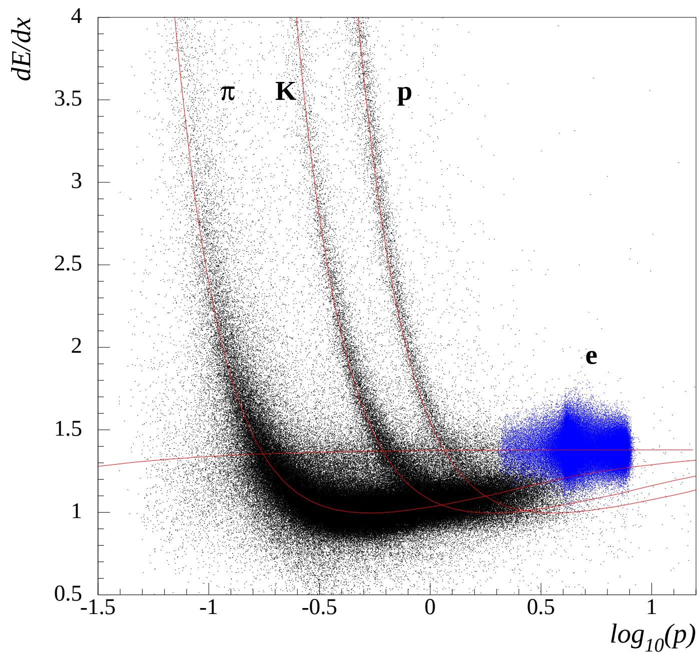

Figure 2.9 – *Truncated mean of dE/dx vs. momentum (in GeV) measured in collision data. Expected curves for pions, kaons, protons and electrons are superimposed.*

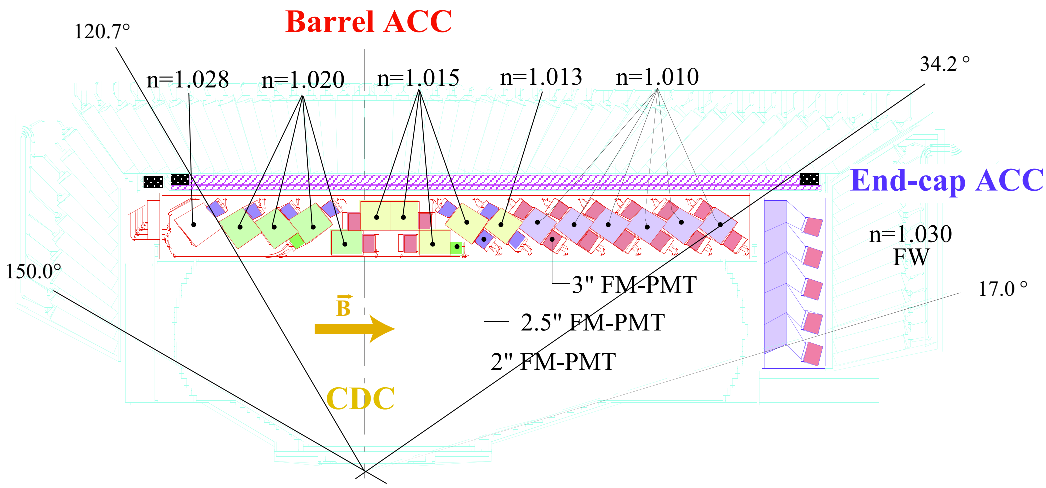

FIGURE 2.10 – *The aerogel Cherenkov counter system (ACC).*

used in the track fit. The track is then matched with SVD information to improve the determination of the pivot location and related parameters. Finally, the track is fitted backward to optimise the parameters at the outermost CDC point [24]. The resulting resolutions on track information are found to be:

$$
\begin{aligned}
\frac{\sigma_{p_\perp}}{p_\perp} &= (0.19 p_\perp \oplus 0.30)\% \\
\sigma_{xy} &= \left(\frac{49}{p\beta \sin^{3/2}\theta}\right) \oplus 19\ \mu\text{m} \\
\sigma_z &= \left(\frac{54}{p\beta \sin^{5/2}\theta}\right) \oplus 36\ \mu\text{m}
\end{aligned}
\tag{2.3}
$$

where p is the total momentum of the track in GeV and $\oplus$ indicates a quadratic sum.

In addition to track reconstruction, each hit in the CDC provides information on the energy deposited in the gas by the charged particle. Since dE/dx mainly depends on β, particles of different mass have a different dE/dx for a same value of β. An average dE/dx is obtained from the track hits using a truncated-mean method in order to remove Landau tails subjected to large fluctuations. The result is shown in Figure 2.9 on the preceding page.

Appendix A on page 101 gives more details on the operation of gas chambers. Reference [25] provides additional information on the CDC.

2.2.3 Aerogel Cherenkov counter

The separation between kaons and pions is essential for B physics. In Belle, this is achieved by the silica aerogel Cherenkov counter (ACC) shown on Figure 2.10 on the previous page. It consists of 960 counter modules in the barrel part (around the CDC) and 228 modules in the forward end-cap region of the detector.

In order to obtain a good kaon/pion separation, modules have refractive indexes between 1.01 and 1.03 depending on the polar angle they cover. A particle travelling at velocity v through a medium with refractive index n will emit Cherenkov light if v is greater than the speed of light in this medium: $v > c/n$. Since kaons are more massive than pions ($m_{K^\pm} \approx 3.5 m_{\pi^\pm}$), a kaon of given momentum will travel more slowly than a pion of the same momentum. The latter would then emit light in the aerogel, the former would not. The refractive indexes were chosen to cover momenta from 1.2 to 3.5 GeV/c.

An ACC module is made of five aerogel tiles stacked in a thin aluminium box. The Cherenkov light is detected by one or two fine mesh-type photomultiplier tubes attached directly on the box. For particles under 4 GeV, the kaon identification efficiency exceeds 80%, while the pion fake rate remains below 10%. Finally, electron identification is also possible below the pion threshold (about 1 GeV/c).

More details can be found in [26].

2.2.4 Time-of-flight counters

The time-of-flight counters system (TOF) adds a piece of information in the particle identification and provides fast trigger signals. It consists of 128 TOF counters and 64 trigger scintillation counters (TSC) made of fast scintillators and fine-mesh photo-multiplier tubes. Figure 2.11 on the facing page shows how TOF and TSC modules are configured. The TOF system covers $33^\circ < \theta < 121^\circ$ (corresponding to the barrel ACC region).

The signal of a particle crossing the TSC is used in coincidence with the two adjacent TOF counters to create a trigger signal (less than 3.5 ns time jitter, 0.5 ns after correction).

The TOF is used to measure the time T elapsed between a collision at the interaction point and the passage of a decay particle through a TOF module. The time resolution is better than 100 ps. The mass of the particle can then be calculated using the CDC information:

$$m = p\sqrt{\left(\frac{cT}{L}\right)^2 - 1} \tag{2.4}$$

where p is the momentum of the particle and L is the path length from the interaction point

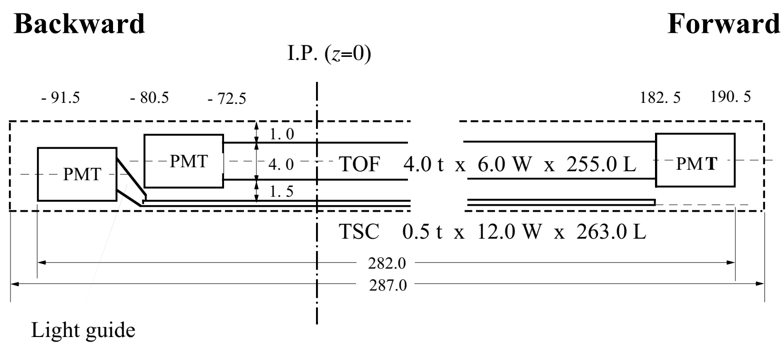

FIGURE 2.11 – *Configuration of two time-of-flight (TOF) and one trigger scintillation counter (TSC) modules.*

to the TOF module the particle crossed. The mass distribution reconstructed by this method is shown on Figure 2.12 on the next page.

More details on the TOF system can be found in Reference [27].

2.2.5 Electromagnetic calorimeter

The main purpose of the electromagnetic calorimeter (ECL) is the detection of photons coming from *B* mesons decay products with high efficiency, good resolutions in energy and position, and over a wide range of energy. In addition, the ECL is the main component of electron identification.

The ECL is an array of 8736 tower-shaped CsI (Tl) crystals that roughly project to the interaction point. The ECL consists of a barrel part (6624 crystals) and two end-cap parts, as shown in Figure 2.13 on the next page. Each crystal is 30 cm in depth and approximately 5×5 cm^2 in cross-section. The ECL covers $12° < \theta < 155°$ (91% of the full solid angle). Scintillation light from each crystal is read out by a pair of silicon PIN photodiodes mounted at the rear end of the crystal.

Electromagnetic showers are produced by incident electrons through bremsstrahlung and pair creation. The shape and total energy of these showers differ greatly from hadronic showers induced by pions and other hadrons, which only deposit a small amount of their total energy. The comparison of the deposited energy and the reconstructed momentum of the incident particle also helps identifying electrons.

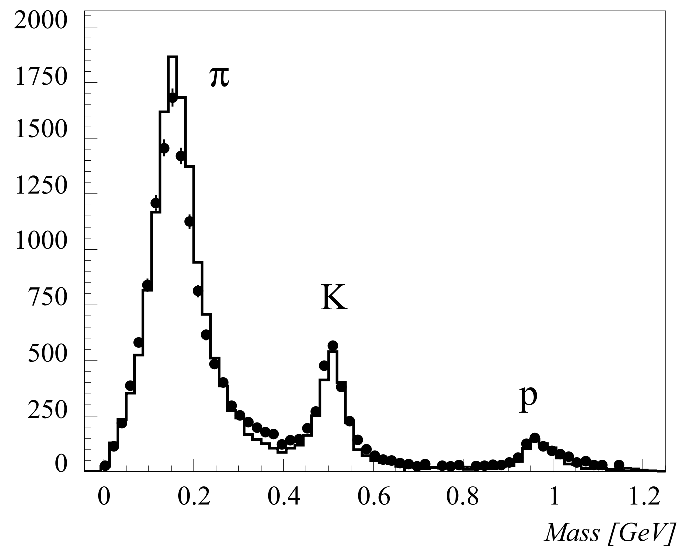

Figure 2.12 – *Mass distribution of particles crossing the TOF system calculated using Equation 2.4 on page 26. Distinct mass peaks appear. The histogram represents Monte Carlo predictions assuming a time resolution of 100 ps.*

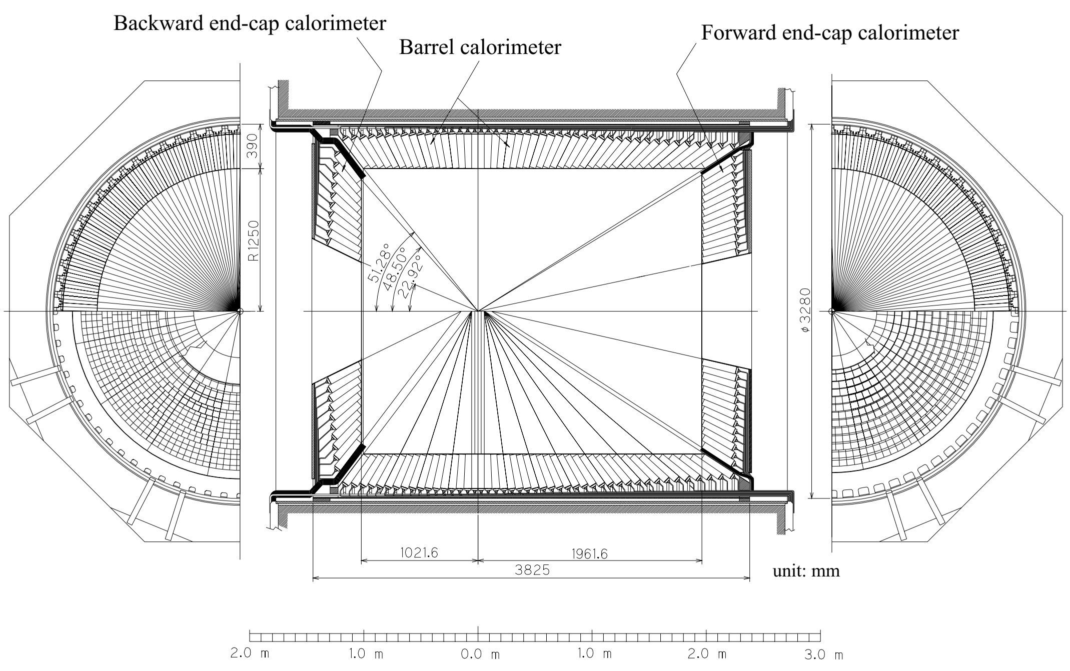

Figure 2.13 – *Configuration of the electromagnetic calorimeter (ECL).*

The energy (in GeV) and position resolutions are given by:

$$\frac{\sigma_E}{E} = \frac{0.066\%}{E} \oplus \frac{0.81\%}{E^{1/4}} \oplus 1.34\%$$

$$\sigma_{\text{pos}} = 0.27 + \frac{3.4}{E^{1/2}} + \frac{1.8}{E^{1/4}} \text{ [mm]}$$

A more complete description can be found in [28].

2.2.6 K-long and muon detector

Neutral long-lived kaons K_L only deposit a small amount of their energy in interactions with the above sub-detectors and live long enough to decay outside of the detector. The same is true for muons, which interact very little with matter. An additional massive detection system was therefore put at the outermost layer of the detector: the K-long and muon detector (KLM).

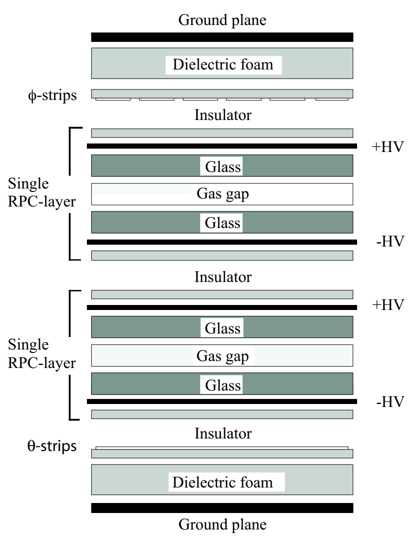

FIGURE 2.14 – *Cross-section of a super-layer in the K-long and muon detector (KLM).*

The KLM detection system was designed to identify K_Ls and muons with high efficiency in a large momentum range above 600 MeV. It consists of alternating layers of resistive-plate chambers (RPC) and 4.7-cm thick iron plates covering $20° < \theta < 155°$. The barrel region ($45° < \theta < 125°$) contains 15 detector layers and 14 iron plates, while 14 detector layers and iron layers compose the forward and backward end-caps. See Figure 2.4 on page 21 for a general view of the KLM system.

Detector layers are grouped in “super-layers”, as shown on Figure 2.14. A super-layer is made of θ and ϕ cathode strips surrounding two RPCs. Resistive-plate counters have two parallel-plate electrodes separated by a gas-filled gap. An ionising particle traversing the gap initiates a streamer in the gas that results in a local discharge. This discharge induces a signal on the external cathode strips which can be used to record the location and the time of the ionisation.

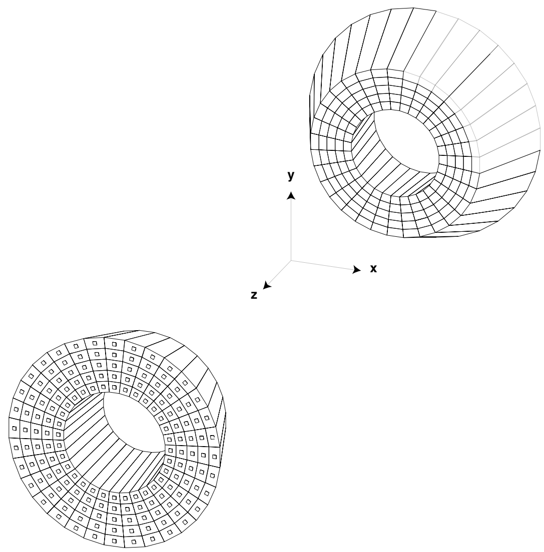

Figure 2.15 – *Isometric view of the crystal arrangement in the extreme forward calorimeter (EFC).*

The iron plates provide a total of 3.9 interaction lengths of material, in addition to the 0.8 interaction lengths provided by the ECL. K_L interact with this material and produce a shower of ionising particles that allows to determine the direction of the K_L from the IP. However, no useful information on the energy can be inferred from the shower.

The range and transverse scattering of charged particles crossing the multiple layers of RPCs can be used to distinguish muons from pions or (charged) kaons. Muons indeed travel much farther and with smaller deflections since they do not interact strongly. The muon detection efficiency above 1.5 GeV is better than 90%, with a fake rate of less than 5%.

More details can be found in [29].

2.2.7 Extreme forward calorimeter

The extreme "forward" calorimeter covers the forward region $6.4° < \theta < 11.5°$ and the backward region $163.3° < \theta < 171.2°$. It extends the angular coverage of the ECL to improve the sensitivity to some very specific physics processes. It also serves as a beam mask to protect the CDC. Finally, it is used as a beam monitor for KEKB and a luminosity monitor for Belle.

Both parts of the ECL are made of 160 BGO crystals arranged in 32 ϕ segments and 5 θ segments (see Figure 2.15 on the facing page). The scintillation light emitted after passage of a charged particle is collected by photo-diodes glued to the rear side of the crystals. The energy resolution of the forward EFC was measured to be 7.3% at 8 GeV, while the backward EFC has 5.8% resolution at 3.5 GeV.

Reference [30] gives more details on the performance of the crystals.

2.3 Trigger

Although the Belle collaboration has interest in a wide range of physics processes, it is known *a priori* that many beam collisions will not produce "interesting" events. In particular, since beam currents are high, a considerable beam background is expected. The role of the trigger is to recognise events of interest, and activate the data acquisition.

The Belle trigger system primarily consists of the Level-1 hardware trigger and the Level-3 software trigger (see sub-section 2.4 on the next page). An additional level of filters, sometimes called Level-4 trigger, acts during off-line reconstruction (see section 2.4.2 on page 33). The signal delivered by the TOF to the SVD can be considered a Level-0 trigger. There is, however, no Level-2 trigger, which would use part of the data during acquisition.

The Level-1 trigger typically runs at 500 MHz at a luminosity of 10^{34} cm^{-2}s^{-1}. An overview of the system is shown in Figure 2.16 on the next page. It consists of sub-detector triggers and a central trigger system called Global Decision Logic (GDL). The sub-trigger signals must have arrived at the GDL less than 1.85 μs after the collision; the global decision signal is issued within a fixed time of 2.2 μs. An accurate trigger timing is given by the TOF trigger (see sub-section 2.2.4 on page 26), or by the ECL if the former is not available.

Sub-detector triggers are based on track or energy information. The CDC and TOF are used to trigger on charged particles. The ECL trigger system is based on the total energy deposit and the number of cluster hits. Additional information on muons can be gathered from the KLM trigger, while the EFC triggers help tagging two-photons and Bhabha events (mainly used for detector calibration). The GDL then combines this information to characterise the event.

The triggers for on-resonance events are of four kinds: 1) three-track triggers, 2) total

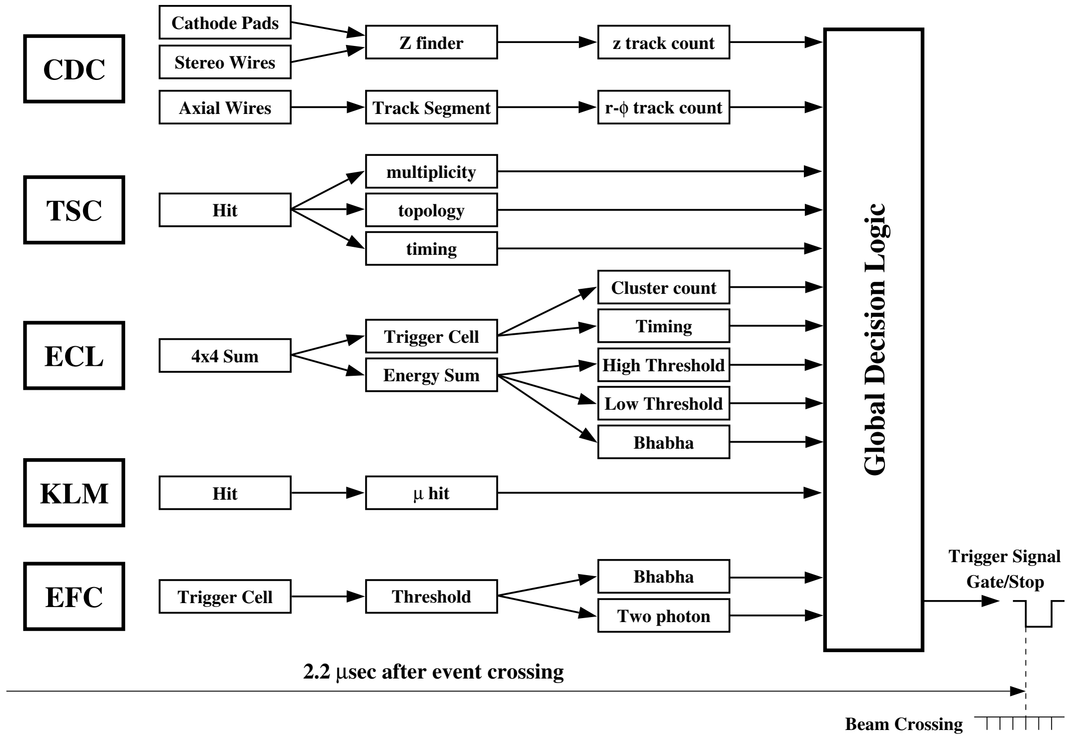

Figure 2.16 – *Level-1 trigger system.*

energy triggers, 3) cluster triggers and 4) a combination of all three first triggers. The total efficiency on this category of events is better than 99.5%.

See Reference [31] for more details.

2.4 Data acquisition and data processing

2.4.1 Data acquisition

The data acquisition (DAQ) of the Belle detector relies on a distributed-parallel system. As shown on Figure 2.17 on page 34, the system is segmented into 7 subsystems running in parallel and corresponding to the different sub-detectors.

In most sub-detectors, the pulse recorded after the crossing of a particle has an integrated charge proportional to the energy deposited by the particle. This charge is converted into time by Q-to-T modules and digitised by time-to-digital converters (TDC). Since the KLM energy information is not used, KLM strip signals are directly read-out by TDCs. TDC pulses are then decoded to reconstruct hit strips. The read-out of SVD signals is performed by on-board chips through flash analog-to-digital converters (FADCs).

When the sequence control receives a GDL signal, sub-detector data is sent to an event-builder. The event-builder combines parallel sub-detectors' data into event-by-event data. The output is then sent to the on-line computer farm. The role of the on-line software is to format event data into the off-line event format and perform further background reduction on hadronic events (Level-3 trigger) using a fast tracking program. It keeps only events with at least one track having a z distance to the IP smaller than 5 cm. Event data is finally sent to the tape library through a 2-kilometre long optical fibre.

2.4.2 Level-4 filter

The purpose of the Level-4 filter is to reduce the background just before the full event reconstruction. The main background is caused by beam interactions with residual gases in the beam pipe. A fast track and cluster reconstruction algorithm was developed to reject these events.

The energy measured in the ECL is required to be greater than 4 GeV. Cosmic-ray events are suppressed. Events are required to contain at least one track with $p_\perp$ greater than 300 MeV, a radial distance to the IP less than 1.0 cm and a z distance to the IP less than 4.0 cm.

2.4.3 Full reconstruction

Events that have passed all levels of trigger, including level 4, are fully reconstructed and stored on data summary tapes (DST). Raw data from the sub-detectors are converted into 4-momentum vectors, closest approach distances to the IP and particle identification probabilities or likelihoods. Additionally, various flags and variables characterising the event are calculated.

After full reconstruction, events are classified into categories called "skims". These include for example the standard hadronic events (`HadronB`), events with J/ψs (`HadronJ`) or Bhabha events. Most physics analyses are based on the `HadronB` sample.

Useful information for users is stored in mini-DST files. The DST files follow the PANTHER table format [32]. The reconstruction software as well as any analysis code is

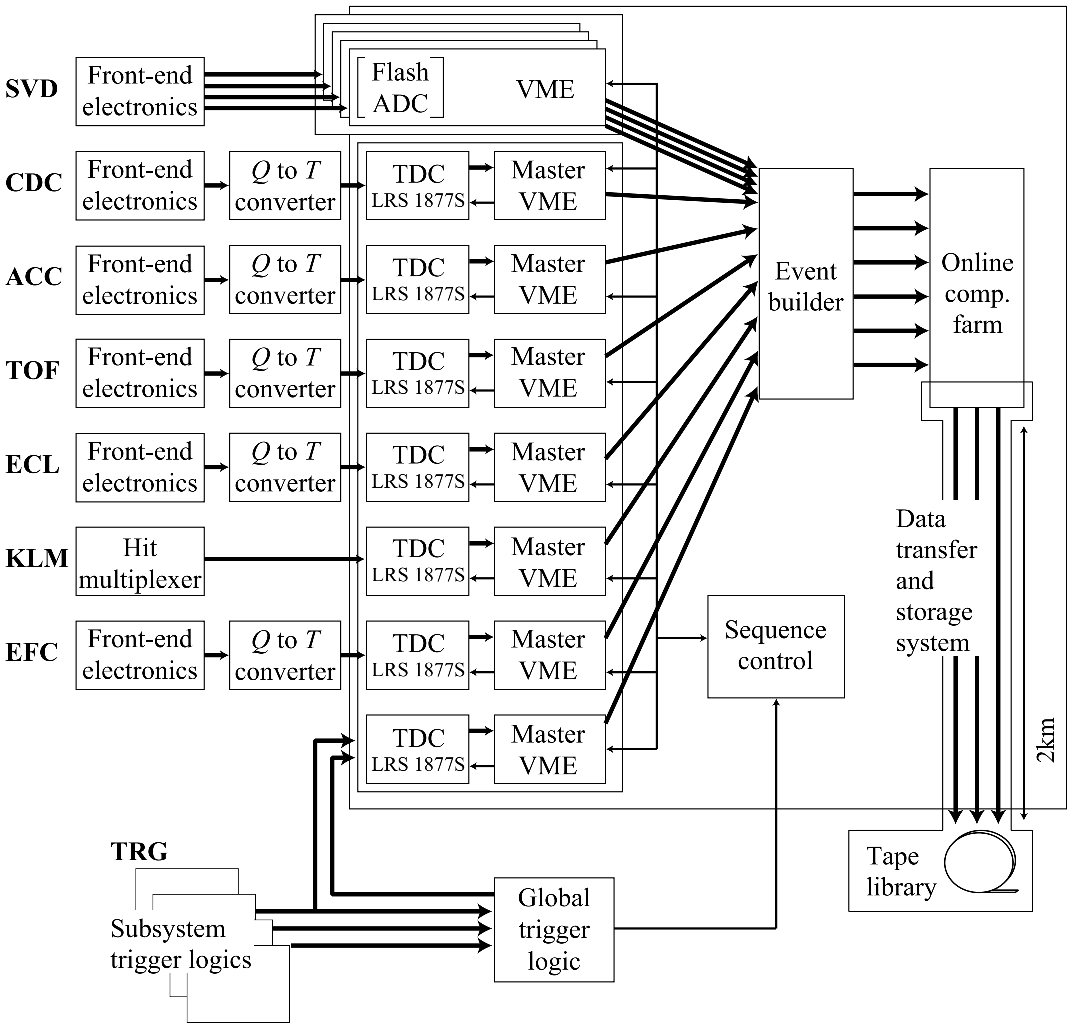

Figure 2.17 – *Overview of the data acquisition system.*

based on B , the Belle analysis framework.

Technical information on the DST production can be found in [33] and references therein.

2.5 Detector simulation

A full simulation of the Belle detector based on Monte Carlo techniques has been developed. Simulated events undergo exactly the same reconstruction as real events.

The simulation is broken into two successive steps: the generation of physics processes in the beam pipe vacuum; the simulation of particle interactions with the detector.

The first step uses the `QQ` event generator [34] developed by the CLEO collaboration and adapted to the needs of Belle. Some specific decays (in particular the decays of D^* mesons) are performed in `EvtGen`, another event generator called inside `QQ` when needed. Branching fractions, masses and lifetimes are set to the PDG 2000 values [35].

The detector is described in a B module called `gsim`, based on the Cern package GEANT3 [36]. Final state particles from the event generator are passed to `gsim` in order to simulate the detector response. The background is simulated by random trigger events from real data embedded in the Monte Carlo sample.

Chapter 3

Reconstruction

THIS analysis is may be regarded as a refinement of the dilepton analysis, where two leptons are reconstructed. In order to improve the background rejection, additional constraints are put on one of the reconstructed leptons. These constraints are chosen to favour the following decay:

$$\begin{aligned} B^0 &\longrightarrow D^{*-}\,\ell^+\,\nu_\ell \\ &\quad D^{*-} \longrightarrow \overline{D}^0\,\pi^- \end{aligned} \tag{3.1}$$

The main background in the dilepton analysis is due to charged B meson decays. Since no decay similar to (3.1) exists at first order for charged B mesons, favouring this decay amounts to suppressing charged semi-leptonic decays.

In this chapter, we first present the idea of the partial reconstruction used to reduce the background. The event selection procedure is then described in detail.

> The physicist, in his study of natural phenomena, has two methods of making progress: (1) the method of experiment and observation, and (2) the method of mathematical reasoning. The former is just the collection of selected data; [...].
>
> — P.A.M. Dirac, *The Relation between Mathematics and Physics*, February 6, 1939

3.1 Partial reconstruction

In principle, all the particles in decay (3.1) on the previous page, except the neutrino, can be reconstructed. From these particles, one can then compute the "missing mass squared" (MMS) of the neutrino[1]:

$$\begin{aligned} M_\nu^2 &= {E_\nu}^2 - {\vec{P}_\nu}^2 \\ &= (E_B - E_\ell - E_{D^*})^2 - \left(\vec{P}_B - \vec{P}_\ell - \vec{P}_{D^*}\right)^2 \\ &= (E_B - E_\ell - E_{D^*})^2 - \vec{P}_B^2 - \left(\vec{P}_\ell + \vec{P}_{D^*}\right)^2 + 2\vec{P}_B \cdot (\vec{P}_\ell + \vec{P}_{D^*}), \end{aligned} \tag{3.2}$$

which should peak at—or very close to—zero.

3.1.1 Extraction of the missing mass squared

Equation (3.2) can be greatly simplified using the two following empirical observations:

1. The B meson is almost at rest in the $\Upsilon(4S)$ centre-of-mass frame.
2. The pion is almost at rest in the D^* centre-of-mass frame.

The first observation allows us to neglect the B meson momentum $\vec{P}_B$, while its energy E_B is known from the $\Upsilon(4S)$ mass. The second observation allows us to reconstruct the momentum and the energy of the D^*, $\vec{P}_{D^*}$ and E_{D^*}, from the slow pion only.

The total energy of the pion in the D^* rest frame, $E_\pi^{D^*}$, is approximately equal to the mass difference between the D^* and the D^0, which has been measured to be 0.145 GeV [19]. If we neglect the momentum of the pion in the D^* rest frame, we get:

$$E_\pi = \gamma E_\pi^{D^*}, \tag{3.3}$$

where γ is such that:

$$E_{D^*} = \gamma M_{D^*}.$$

The energy of the D^* in the $\Upsilon(4S)$ rest frame can then be expressed using the pion energy:

$$E_{D^*} = \frac{E_\pi}{E_\pi^{D^*}} M_{D^*}, \tag{3.4}$$

with $E_\pi^{D^*} = 0.145$ GeV and $M_{D^*} = 2010$ GeV.

[1] In this chapter, all kinematic variables are calculated in the $\Upsilon(4S)$ rest frame, unless otherwise stated.

The D^* momentum can also be expressed using the pion information. Indeed, if the second assumption holds, the pion and the D^* momenta are collinear in the $\Upsilon(4S)$ rest frame. We can then write:

$$\vec{P}_{D^*} = \frac{\vec{P}_\pi}{\left|\vec{P}_\pi\right|}\left|\vec{P}_{D^*}\right| = \hat{P}_\pi \sqrt{E_{D^*}{}^2 - M_{D^*}^2}$$

and using Equation (3.4) on the preceding page:

$$\vec{P}_{D^*} = \hat{P}_\pi M_{D^*} \sqrt{\left(\frac{E_\pi}{E_\pi^{D^*}}\right)^2 - 1} \tag{3.5}$$

Finally, the missing mass squared reduces approximately to:

$$M_\nu^2 \approx (E_{\text{beam}} - E_\ell - \gamma M_{D^*})^2 - \left(\sqrt{\gamma^2 - 1}\, M_{D^*}\hat{P}_\pi + \vec{P}_\ell\right)^2 \tag{3.6}$$

where γ is calculated using Equation (3.3) on the facing page and E_{beam} is the beam energy in the $\Upsilon(4S)$ frame, $E_{\text{beam}} = \sqrt{s}/2$. All the terms of this equation can be calculated from a lepton, a pion, and the centre-of-mass energy.

3.1.2 Generator study

A sample of 500 thousand $\Upsilon(4S)$ decays was generated to evaluate the effect of the various approximations on the D^* 4-momentum calculation and the final missing mass squared distribution. The $\Upsilon(4S)$ is forced to decay into neutral B mesons, which in turn decay into $D^* X \ell \nu_\ell$. In addition, charged D^* decay through the $D^0\pi$ channel only. For this study, however, we only select $B^0 \to D^{*-}\ell^+\nu_\ell$ and charge conjugate decays. These represent about 700 thousand B meson decays.

Figure 3.1 on the next page shows the resolution on the D^* energy, namely:

$$\frac{E_{D^*}^{\text{rec}} - E_{D^*}^{\text{true}}}{E_{D^*}^{\text{true}}},$$

where $E_{D^*}^{\text{rec}}$ is calculated using Equation (3.4) on the facing page, with the generated pion energy, and $E_{D^*}^{\text{true}}$ is the generated D^* energy. The distribution is approximately centred on zero, with a range of 20% on both sides.

The generated angle between the pion and the D^* momenta is shown in Figure 3.2 on page 41. The assumption of collinear momenta is justified by the clear peak around 20 degrees.

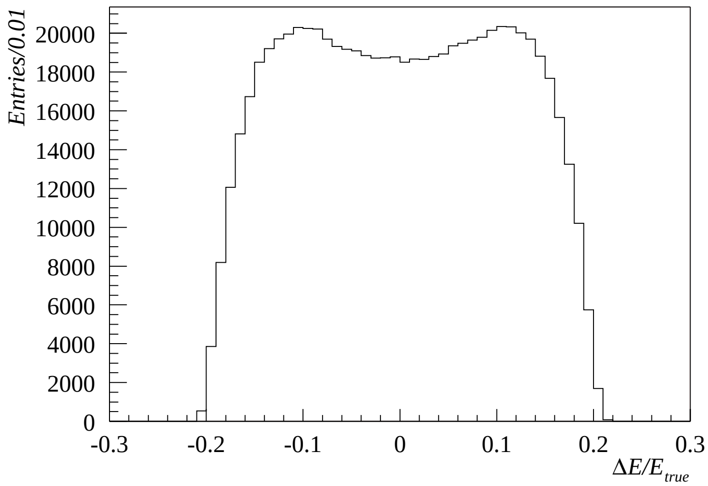

Figure 3.1 – *Resolution on the D^* energy:* $(E^{rec}_{D^*} - E^{true}_{D^*})/E^{true}_{D^*}$.

Figure 3.3 on the facing page presents the vector difference between the reconstructed and the generated D^* momenta in the $\Upsilon(4S)$ frame. The various assumptions used to reconstruct the D^* result in a mean shift of about 600 MeV in momentum (to be compared with an average D^* momentum of 1.4 GeV).

Finally, Figure 3.4 on page 42 shows the effect of the above assumptions on the missing mass squared resolution. Using Equation (3.6) on the previous page, which includes all approximations, results in a broadening of the distribution by about 5 GeV^2, from which 1.5 GeV^2 are due to the B meson momentum approximation.

3.2 Event selection and reconstruction

Since this analysis adds constraints to the reconstruction used for the dilepton analysis, the selected event sample is a sub-sample of the dilepton sample and the reconstruction inherits many parts from the dilepton reconstruction. The additional constraints are designed to favour the decay $B^0 \rightarrow D^{*-}(\overline{D}^0\pi^-)\,\ell^+\nu_\ell$, (see on page 37), mainly by reconstructing the neutrino missing mass squared (MMS). The branching fraction of this decay is shown in Table 3.1 on page 43. In brief, the reconstruction consists in selecting two fast leptons and a slow pion associated with one of the leptons.

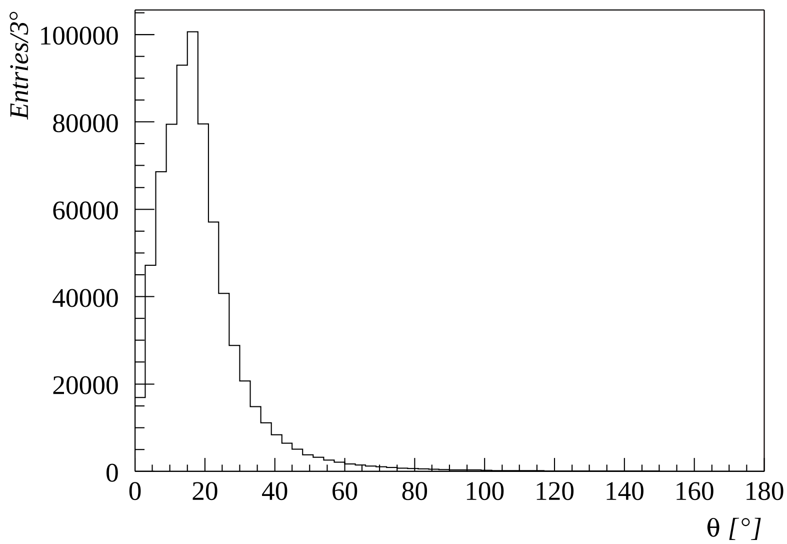

FIGURE 3.2 – *Distribution of the generated angle between the pion and the D^* in the $\Upsilon(4S)$ rest frame.*

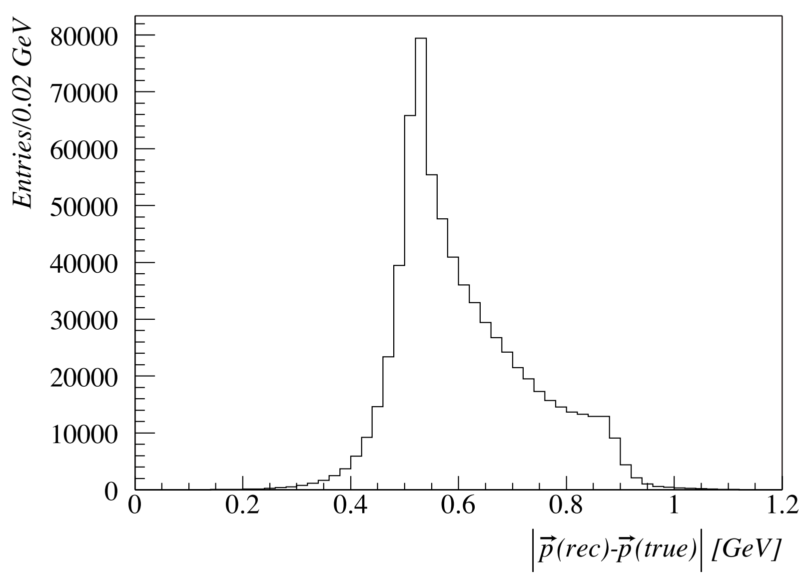

FIGURE 3.3 – *Vector difference between the generated momentum and the reconstructed momentum of the D^*.*

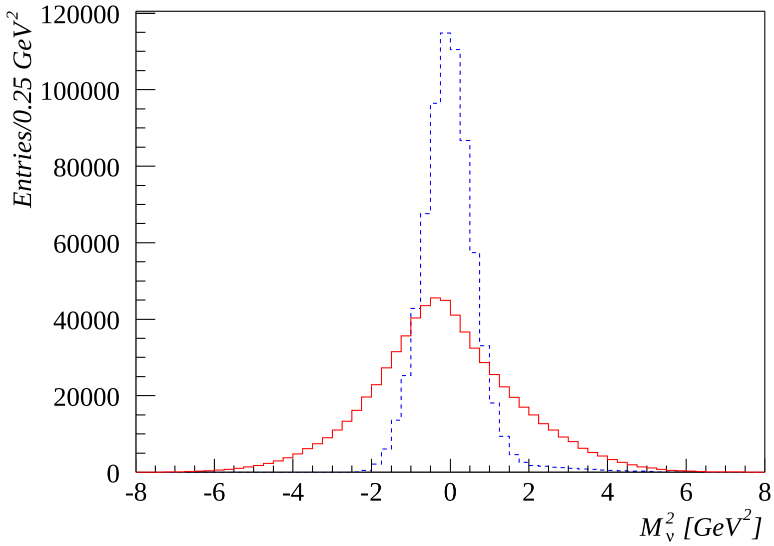

Figure 3.4 – *The missing mass squared calculated (a) only assuming that the B meson is at rest in the* $\Upsilon(4S)$ *rest frame (dashed histogram) and (b) using Equation 3.6 on page 39 (plain histogram).*

In this section, we classify events in three different categories:

1. *signal* events, where both candidate leptons directly come from the decay of a neutral B meson (primary leptons), regardless of the origin of the selected pion;

2. *B background* events, where both candidate leptons come from the decay chain of charged or neutral B mesons, but at least one lepton is not a primary lepton. This includes fake leptons (hadrons identified as leptons) and secondary leptons (e.g. from charmed meson decays);

3. *continuum* events, where candidate leptons come from non-resonant events.

The selection has been tuned to maximise the signal over background ratio in the region $M_\nu^2 > -2$ GeV^2 (MMS signal region), as well as the signal reconstruction efficiency.

Although this has little impact on the reconstruction, it should be mentioned that in addition to decay (3.1) on page 37, other decays have a peaking MMS. Neutral B mesons

TABLE 3.1 – *Branching fractions of B meson decays with peaking MMS distributions [19, 37]. The second decay includes resonant and non-resonant modes with charged and neutral D^*s. The branching fraction of the subsequent D^* decay is also given.*

$B^0 \to D^{*-}l^+\nu_l$	$(5.53 \pm 0.23)\%$
$B \to \overline{D}^*\pi l^+\nu_l$	$(1.86 \pm 0.38)\%$
$D^{*-} \to \overline{D}^0\pi^-$	$(67.7 \pm 0.5)\%$

may indeed decay through the following cascade[2]:

$$B^0 \to D^{**-}(D^{*-}\pi^0)\,\ell^+\nu_\ell \tag{3.7}$$

and its non-resonant counter-part:

$$B^0 \to D^{*-}\pi^0\ell^+\nu_\ell \tag{3.8}$$

These events are regarded as signal events.

Similarly, charged B mesons can produce events with peaking MMS through the decays:

$$B^+ \to \overline{D}^{**0}(D^{*-}\pi^+)\,\ell^+\nu_\ell \tag{3.9}$$

and

$$B^+ \to D^{*-}\pi^+\ell^+\nu_\ell \tag{3.10}$$

These events fall in the B background category.

Branching fractions related to these decays are listed in Table 3.1. The total contribution of $B \to D^{*-}\pi l^+\nu_l$ resonant and non-resonant events to the peak (before selection) is $14 \pm 8\%$, $2/3$ of which are due to charged B mesons, because of isospin symmetry. The resonant modes, indeed, include:

$$\begin{array}{lcl}
B^0 \to D^{**-}\ell^+\nu_\ell & , & D^{**-} \to D^{*-}\pi^0 \\
B^0 \to D^{**-}\ell^+\nu_\ell & , & D^{**-} \to \overline{D}^{*0}\,\pi^- \\
B^+ \to \overline{D}^{**0}\ell^+\nu_\ell & , & \overline{D}^{**0} \to \overline{D}^{*0}\,\pi^0 \\
B^+ \to \overline{D}^{**0}\ell^+\nu_\ell & , & \overline{D}^{**0} \to D^{*-}\pi^+
\end{array} \tag{3.11}$$

[2]The term D^{**} refers to all excited D states with mass greater than the $D^*(2010)$ mass.

Conservation of the isospin predicts twice larger branching fraction for modes with a charged pion. Since we select modes containing charged D^*s, we obtain twice more charged B meson modes. The same argument holds for non-resonant decays. We assume $f_0 = f_+$ and $b_0 = b_+$, where f_0 and f_+ are the branching fraction of $\Upsilon(4S)$ to neutral and charged B meson pairs, respectively. b_0 and b_+ are the semi-leptonic branching fractions of neutral and charged B mesons.

3.2.1 Data set

All available data collected by summer 2003 were used in this analysis. The corresponding integrated luminosity is shown in Table 3.2 on the facing page. Experimental data include on-resonance data collected at $\sqrt{s}$ close to the $\Upsilon(4S)$ rest mass, and off-resonance data collected at $\sqrt{s}$ 60 MeV below the $\Upsilon(4S)$ rest mass. The e^+e^- cross-section is proportional to $1/s$. Quoted off-resonance luminosities have been corrected for the difference in $\sqrt{s}$. The number of continuum events in the on-resonance data can then simply be deduced from the number of off-resonance events multiplied by the luminosity ratio.

The total experimental data correspond to about 152 million $B\overline{B}$ pairs.

Different types of Monte Carlo events were generated by the Belle collaboration (see section 2.5 on page 35). There are:

- `mixed` events: $\Upsilon(4S) \to B_d^0\overline{B}_d^0$;
- `charged` events: $\Upsilon(4S) \to B^+B^-$;
- `charm` events: $e^+e^- \to c\overline{c}$;
- `uds` events: $e^+e^- \to q\overline{q}$, where q is u, d or s.

The two last types constitute continuum events.

Detector conditions are set in the Monte Carlo to match the different experiment conditions. As already mentioned, physical parameters are set to the world averages of year 2000. Randomly triggered experimental events are embedded in the simulated data to account for detector background. For various technical reasons (disk damage and software problem), only a small portion of the produced Monte Carlo sample could be used.

The amount of Monte Carlo events used in this analysis is listed in Table 3.3 on the facing page. The total corresponds to about 107 fb^{-1} or 80% of the experimental data.

TABLE 3.2 – *Integrated luminosity of the various run periods in fb^{-1}. The ratio of on-resonance to off-resonance data is shown for each experiment. Off-resonance luminosity has been corrected for the difference in cross-sections.*

Experiment	*On-res.*	*Off-res.*	*Ratio*
7	5.93	0.59	10.05
9	4.44	—	—
11	8.13	1.21	6.72
13	10.74	1.20	8.95
15	12.84	1.41	9.11
17	11.97	0.85	14.08
19	25.06	3.58	7.00
21	4.35	—	—
23	6.06	0.72	8.42
25	25.74	1.67	15.41
27	25.43	3.75	6.78
Total	139.71	14.97	9.33

TABLE 3.3 – *Number of million events processed from each Monte Carlo type and experiment. One million* `mixed` *or* `charged` *events correspond to approximately 1.8 fb^{-1}.*

Experiment	`mixed`	`charged`	`charm`	`uds`
19	12.21	9.01	28.16	32.79
21	4.44	4.44	4.10	6.55
23	11.47	11.47	26.47	42.34
25	31.51	34.31	69.63	117.27
Total	59.62	59.22	128.36	198.95

3.2.2 Event preselection

Experimental events triggered as “hadronic events” also contain processes such as τ pair production, Bhabha and radiative Bhabha (QED events), two-photon pair production and beam gas interactions. Selection criteria are, therefore, already applied at the last stage of data production in order to reject all non-hadronic processes and keep all $B\overline{B}$ events. These criteria are grouped under the name `HadronB` [38].

In the following, we define *good tracks* as tracks with $p_\perp > 100$ MeV, and projected closest distance of approach to the interaction point $|dr| < 2$ cm and $|dz| < 4$ cm. *Good clusters* are ECL clusters with energy greater than 100 MeV. Finally, *good photons* are good clusters that cannot be associated with tracks in the CDC.

The `HadronB` cuts require:

Track multiplicity The number of good charged tracks $nTrk$ must satisfy $nTrk \geq 3$.

Cluster multiplicity The number of good clusters with $-0.7 < \cos\theta < 0.8$ must be greater than or equal to 2. This removes QED events, as well as beam gas or two photon interactions.

Visible energy The sum of good charged tracks[3] and good photon energies, E_{vis}, must satisfy $E_{\text{vis}} \geq 0.2\sqrt{s}$.

Momentum balance The sum of z components of all good charged tracks and good photons P_z should be balanced around zero: we require $|P_z| < 0.5\sqrt{s}$.

Calorimeter energy sum The sum of energies of good clusters in the barrel region, E_{barrel}, must satisfy $0.1 < E_{\text{barrel}}/\sqrt{s} < 0.8$. This mainly removes QED events.

Average cluster energy The previous cut efficiently removes QED events where both electrons are deposited in the ECL. It is inefficient if one of the electrons passes outside the ECL acceptance. To compensate for this, a cut is placed on the average cluster energy: $E_{\text{sum}}/N_{\text{ECL}} < 1.0$ GeV.

Event primary vertex The vertex formed by geometrically fitting all good charged tracks must satisfy: $|dr| < 1.5$ cm and $|dz| < 3.5$ cm. This removes beam pipe and beam gas background.

[3] The track energy is calculated from the track momentum and the pion mass.

Conditional calorimeter energy sum We also cut sum of energies of good clusters in the detector (barrel and end-cap regions) to further reduce τ pair, beam gas and two photon events with low energy sum. In order to keep some continuum events, this cut is used in conjunction with a cut on the *heavy jet mass* M_{HJ}:

$$E_{\mathrm{sum}} > 0.18\sqrt{s} \quad \text{or} \quad M_{\mathrm{HJ}} > 1.8\ \mathrm{GeV}.$$

M_{HJ} is defined as follows: the event is split into two hemispheres by a plane perpendicular to the event thrust axis[4]. The invariant mass of tracks in each hemisphere is calculated assuming the pion mass for all tracks. The tracks on the side with the larger invariant mass form the heavy jet (see [39, page 23]).

Conditional normalised heavy jet mass The heavy jet mass was found to be shifted in the Monte Carlo with respect to the data. In order to avoid unpredictable effects of a precise cut on this quantity on hadronic events, M_{HJ} is normalised by the visible energy, which shows the same effect. The following cut is then applied:

$$M_{\mathrm{HJ}}/E_{\mathrm{vis}} > 0.18\sqrt{s} \quad \text{or} \quad M_{\mathrm{HJ}} > 1.8\ \mathrm{GeV}.$$

The heavy jet condition is again added to retain some continuum events.

3.2.3 Event selection

Since continuum events are unwanted in this analysis, further QED and beam gas reduction is performed together with continuum suppression. First, the `HadronB` cuts are tightened as follows:

– track multiplicity: $nTrk \geq 5$;

– visible energy: $E_{\mathrm{vis}} \geq 0.5\sqrt{s}$;

– momentum balance: $|P_z| \leq 0.33\sqrt{s}$.

Second, a cut on the second normalised Fox–Wolfram moment R_2 is applied. R_2 is related to the sphericity of an event: it is close to zero for $B\overline{B}$ events and close to one for jet-like continuum events. It is defined as follows [40]:

$$R_2 = H_1/H_0, \tag{3.12}$$

$$H_l \equiv \sum_{i,j} |\vec{p}_i^{\,*}||\vec{p}_j^{\,*}|P_l(\cos\theta_{ij}), \tag{3.13}$$

[4]The thrust axis $\vec{n}$ is defined by $\vec{n} = \max(\sum_i \vec{n}\cdot\vec{p}_i/\sum_i \vec{p}_i)$, where the $\vec{p}_i$ are the 3-momenta of the good charged tracks and good gammas.

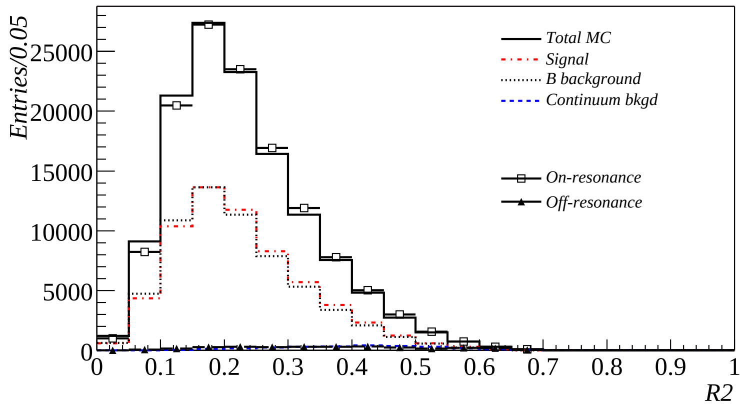

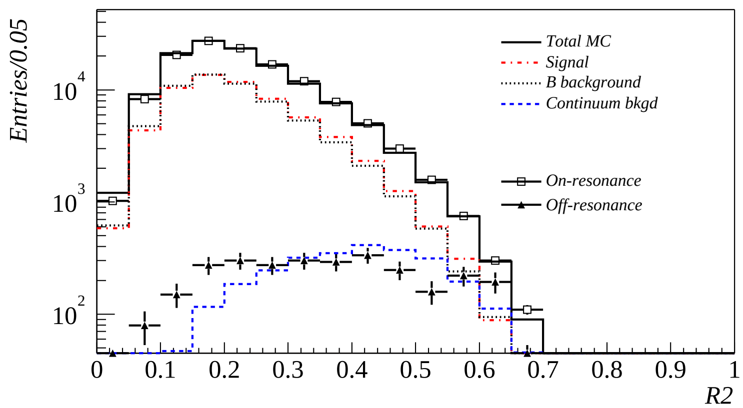

FIGURE 3.5 – *Distribution of the second normalized Fox-Wolfram moment R_2 after the whole selection. The lower plot has a logarithmic vertical scale.*

where P_l are the Legendre polynomials and the sum runs on all good charged tracks. We require $R_2 < 0.7$. The distribution of R_2 in fully selected events, including the selection described in the following sections, is shown in Figure 3.5.

Finally, only good charged tracks are used in the selection described in the following sections.

3.2.4 Particle identification

Electrons

The electron identification uses information from the CDC, ACC and ECL subsystems to construct five discriminants, which are then used in a likelihood function. An electron likelihood L_e and a non-electron likelihood $L_{\bar{e}}$ are separately calculated for each discriminant and combined into the following total likelihood [41]:

$$L_{\text{eid}} = \frac{\prod_{i=1}^{5} L_e^i}{\prod_{i=1}^{5} L_e^i + \prod_{i=1}^{5} L_{\bar{e}}^i} \tag{3.14}$$

The discriminants are:

1. *The matching between the position of the charged track extrapolated to the ECL and the position of a cluster in the ECL.* The position resolution for electron showers is considerably smaller than for hadronic showers. The matching χ^2 is defined by:

$$\chi^2 \equiv \left(\frac{\Delta\phi}{\sigma_{\Delta\phi}}\right)^2 + \left(\frac{\Delta\theta}{\sigma_{\Delta\theta}}\right)^2 \tag{3.15}$$

   where the σ are obtained by fits to the distributions of $\Delta\phi$ and $\Delta\theta$ for electrons. For each charged track, the matching cluster is the cluster with lowest χ^2. It is then used to calculate the E/p ratio (see below). If no cluster with $\chi^2 < 50$ is found, the track is considered to have no associated cluster in the ECL.

2. *The ratio of the energy measured by the ECL and the momentum measured in the CDC, E/p.* This quantity is very close to one for electrons, because of their small mass and all their energy is deposited in the ECL.

3. *The transverse shower shape.* The shape of the shower deposited in the ECL differs greatly for hadrons and electrons. This is quantified by the ratio E_9/E_{25}. E_9 is the sum of the energies deposited in a 3×3 array of crystals surrounding the crystal located at the centre of the shower, while E_{25} is that in a 5×5 array centred on the same crystal.

4. *Energy loss in the CDC.* A χ^2 variable is formed using the measured dE/dx, the expected dE/dx from the Bethe–Bloch formula [42, 43] and the expected resolution from beam test results:

$$\chi^2 \equiv \left(\frac{(dE/dx)_{\text{meas}} - (dE/dx)_{\text{exp}}}{\sigma_{\text{exp}}}\right)^2 . \tag{3.16}$$

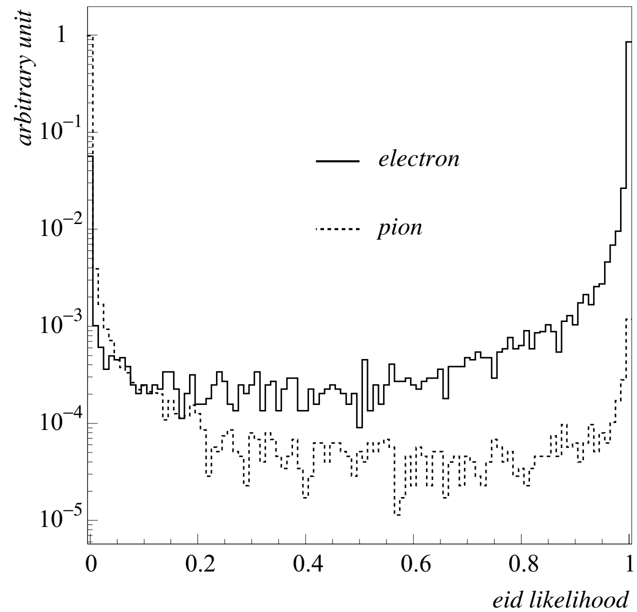

Figure 3.6 – *Likelihood distribution used for electron identification (from [41]).*

The probability density function (PDF) used for the corresponding likelihood is a Gaussian function of this χ^2.

5. *Light yield in the ACC.* The Cherenkov threshold in the ACC for electrons is only a few MeV, while that for pions is between 0.5 and 1.0 GeV, depending on the refractive index. The light yield then provides a good electron-pion separation for low momentum tracks. The electron and pion PDFs for this quantity are calculated from Monte Carlo distributions.

The PDFs for the three first discriminants are fitted to radiative Bhabha data (for electrons) and generic Monte Carlo (for hadrons). They are broken into six polar angle and ten momentum ranges to take into account the dependence on these two kinematic variables. The resulting likelihood distributions for electrons and pions are shown on Figure 3.6. We require $L_{\text{eid}} > 0.7$ for loose selection and $L_{\text{eid}} > 0.8$ for tight selection.

Additionally, in order to reject $\gamma \to e^+e^-$ conversions, the invariant mass M_{ee} of candidate electrons with any other oppositely charged track is calculated. M_{ee} is then required to be greater than 100 MeV for all combinations.

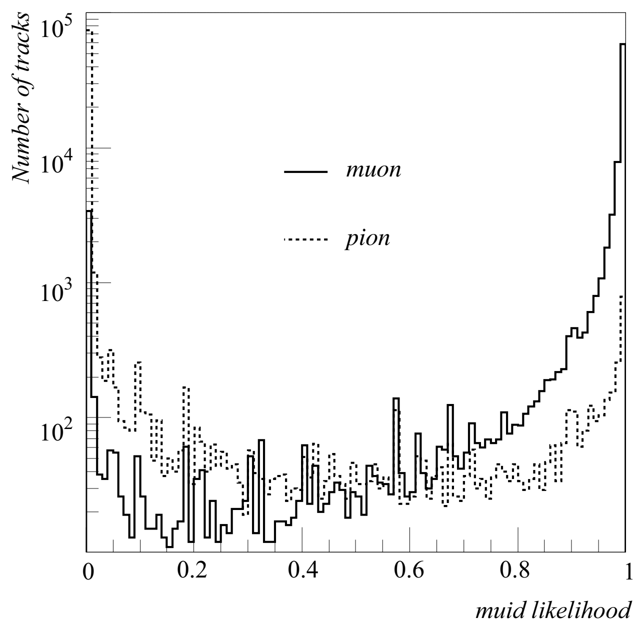

FIGURE 3.7 – *Likelihood distribution used for muon identification (from [44]).*

Muons

Muon identification is performed by extrapolating candidate tracks reconstructed in the CDC and SVD subsystems to the RPC layers of the KLM. Hits in the KLM are associated to a track if they are located within 25 cm or 5σ of the track's crossing point with the RPC plane. Two quantities are then used to construct the PDFs used in the muon likelihood: the difference between the expected and the observed range in the KLM[5], ΔR, and χ_r^2, the reduced χ^2 of the transverse deviation of all hits associated with the track. The expected range is calculated using `GEANT` and Kalman filtering.

The probability density functions for ΔR and χ_r^2 are constructed using simulated single-track events of muons, pions and kaons. The joint PDF is formed by the product of the separate PDF, which are expected to be uncorrelated: $p^i(\Delta R \chi_r^2) = p_1^i(\Delta R) + p_2^i(\chi_r^2)$, where i is μ, K or π. The muon likelihood for a given track is then given by:

$$L_{\text{muid}} = \frac{p^\mu}{p^\mu + p^K + p^\pi}. \tag{3.17}$$

The resulting likelihood distributions for muons and pions are shown We require $L_\mu > 0.8$

[5]The range of a track in the KLM is the number of RPC layers it crosses.

for loose selection and $L_\mu > 0.9$ for tight selection. Additionally, χ_r^2 is required to be less than 3.5, in order to reject "hit sharing" [45, p. 63–64].

3.2.5 First lepton selection

After the event selection, good charged tracks are parsed to find a first lepton candidate. The following criteria are applied:

- The projected closest distance of approach to the IP are required to satisfy: $|dz| < 2.0$ cm, $|dr| < 0.05$ cm. This rejects poorly reconstructed tracks as well as products of decays in flight.

- Tracks must have left at least one $r - \phi$ hit and two z hits in the SVD, to ensure good vertex resolution.

- If the electron likelihood is greater than 0.7 (loose selection), the candidate is considered to be an electron. If this requirement is not met, but the muon likelihood is greater than 0.8 (loose selection), it is considered to be a muon.

- The CMS momentum p^* must be greater than 1.8 GeV, in order to reject secondary leptons. An upper limit at 2.3 GeV is also set to reduce the continuum contribution. The distribution of this quantity is shown in Figure 3.8 on the next page.

- The invariant mass $M_{\ell\ell}$ of each candidate lepton with any oppositely charged track is calculated. If the result is compatible with the mass of the J/ψ meson, the entire event is rejected. The compatibility is defined by the following criteria for electron and muon candidates respectively:

$$-0.15 \text{ GeV} < (M_{e^+e^-} - M_{J/\psi}) < 0.05 \text{ GeV}$$
$$-0.05 \text{ GeV} < (M_{\mu^+\mu^-} - M_{J/\psi}) < 0.05 \text{ GeV}$$

  A looser cut is applied to electron candidates to account for possible bremsstrahlung energy loss. The distributions of $M_{\ell\ell}$ are shown in Figure 3.9 on page 54.

3.2.6 Soft pion selection

A charged track that has not passed the lepton identification of the first lepton selection is considered a pion candidate. In order to be selected as a soft pion, it must further pass the two following loose requirements:

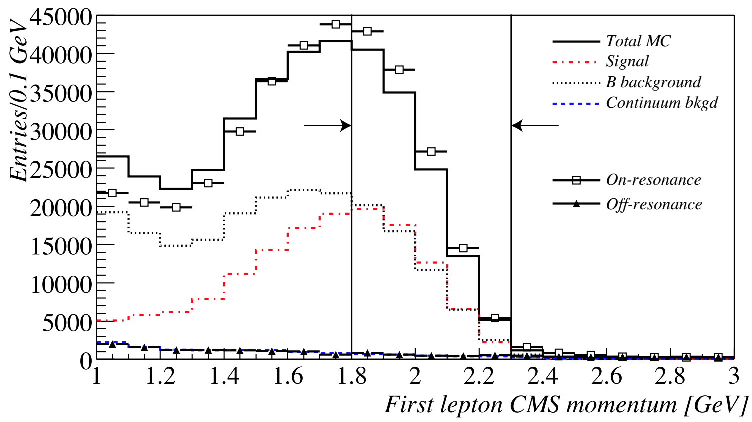

FIGURE 3.8 – *Distribution of the first lepton momentum in experimental data and Monte Carlo, after the whole selection except cuts on this quantity. The arrows indicate the cuts we apply.*

- $|dz| < 5$ cm and $|dr| < 2$ cm,
- $p^* < 1$ GeV.

3.2.7 Lepton-pion pair selection

Candidate leptons are associated with oppositely charged soft pions. The missing mass squared is calculated for each candidate pair, and is required to be greater than -15 GeV^2. If several pions can be associated to the same lepton, the pion with lowest momentum is chosen. The MMS distribution after the whole selection is shown in Figure 3.10 on page 55.

3.2.8 Second lepton selection

If at least one candidate lepton-pion pair has been found, another lepton is searched for. The selection is the same as for the first lepton, except for the following criteria:

- The CMS momentum must satisfy: 1.3 GeV $< p^* <$ 2.3 GeV. The distribution of this quantity is shown in Figure 3.11 on page 55.
- The electron likelihood must be greater than 0.8 (tight selection).
- The muon likelihood must be greater than 0.9 (tight selection).

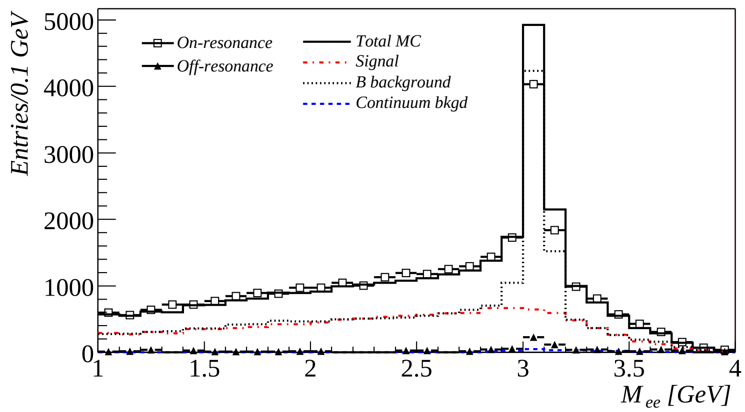

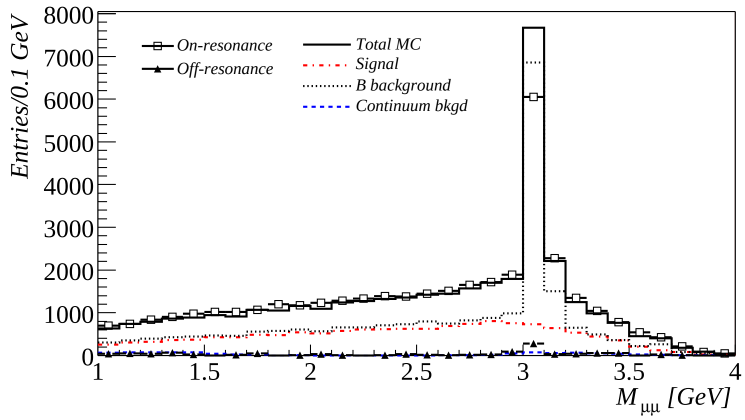

Figure 3.9 – *Invariant mass of the two leptons for $e^{\pm}e^{\mp}$ candidates (top) and $\mu^{\pm}\mu^{\mp}$ candidates (bottom) after the whole selection except the invariant mass cut.*

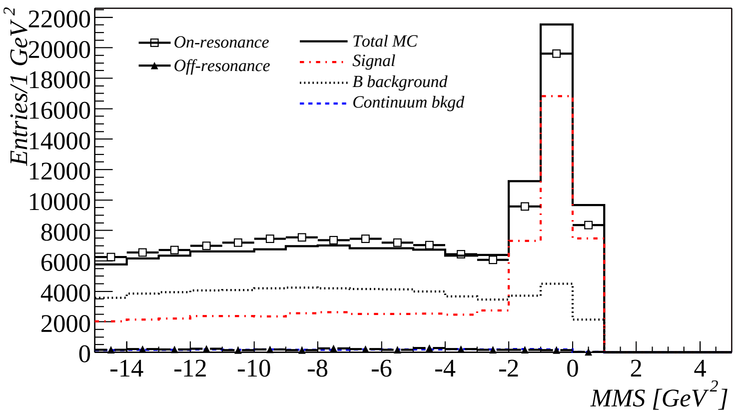

FIGURE 3.10 – *Missing mass squared of candidate lepton-pion pairs after the whole selection.*

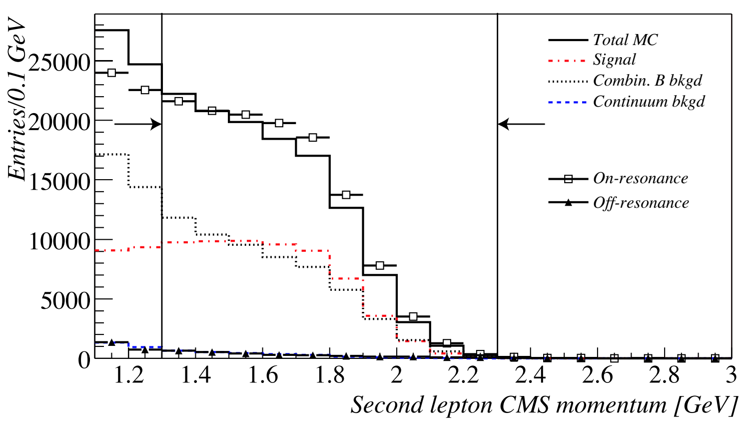

FIGURE 3.11 – *Distribution of the second lepton momentum in experimental data and Monte Carlo, after the whole selection except cuts on this quantity. The arrows indicate the cuts we apply.*

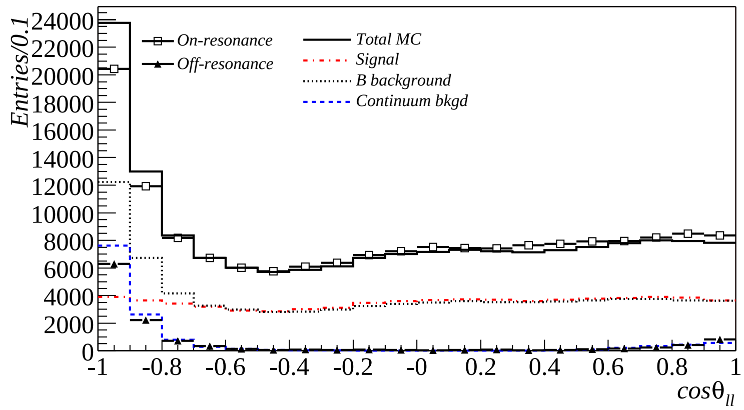

Figure 3.12 – *Cosine of the opening angle between the two lepton candidates in the CMS, after the complete selection except the limits on* $\cos\theta_{\ell\ell}$.

The momentum lower limit is much tighter for the first lepton in order to enhance the MMS constraint. The lepton identification is, however, a little worse for softer leptons. In addition, the soft pion association improves the first lepton identification. Tighter identification cuts are, therefore, applied to the second lepton.

3.2.9 Dilepton selection

Pairs of leptons (dileptons) are formed by combining second lepton candidates with first lepton candidates associated with a pion.

Limits are set on the cosine of the angle $\theta_{\ell\ell}$ between the two lepton tracks in the CMS. This helps reducing continuum events, which have a jet-like shape and thus peak at $\cos\theta_{\ell\ell} = \pm 1$. Correlated leptons coming from the same B mainly peak at $\cos\theta_{\ell\ell} = -1$ and are also efficiently rejected by these limits. Signal leptons are not correlated and therefore have a flat $\cos\theta_{\ell\ell}$ distribution. We require $-0.8 < \cos\theta_{\ell\ell} < 0.95$. The distribution of $\cos\theta_{\ell\ell}$ before applying this cut is shown in Figure 3.12.

If several dilepton candidates pass all the requirements we only keep the one with the first lepton of highest p^* (and that with the second lepton of highest p^* in case of identical first lepton).

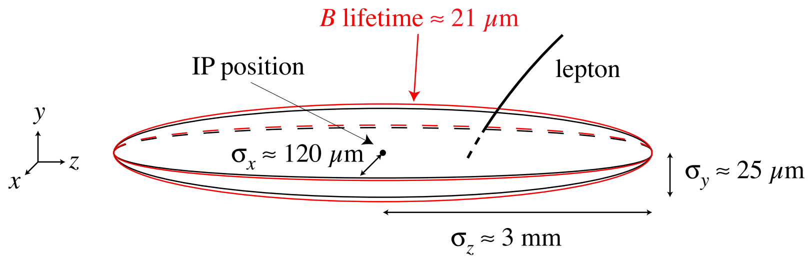

FIGURE 3.13 – *Illustration of the z position measurement of a B decay vertex. The mean errors on the IP position are shown.*

3.2.10 Δz measurement

The z-coordinate of each B meson decay vertex is inferred from the production point of each candidate lepton. The track of each candidate lepton is geometrically fitted with the event-by-event IP profile using the `kfitter` package [46,47]. The mean position of the IP is determined from hadronic events, every 10 thousand events. Its mean error is determined for each run (corresponding to one beam fill). The candidate lepton track is then constrained to be consistent with the IP profile, smeared by 21 μm in the $r-\phi$ plane to take into account the transverse B decay length, as shown in Figure 3.13.

Δz is obtained by subtracting the measured z position corresponding to the second lepton from the z position corresponding to the first lepton:

$$\Delta z = z_1 - z_2, \tag{3.18}$$

where the first lepton has been associated with a soft pion. The pion track is not used to estimate Δz (but it is used to estimate the missing mass squared, as explained in Section 3.1.1 on page 38).

3.2.11 Selection result

Events with $|\Delta z| > 2$ mm are eliminated. We then define two selection regions in the MMS distribution: the side-band region (used in the MMS fit described below) ranges from -15 to -2 GeV^2; the signal region (used in the MMS fit and the Δz fit) ranges from -2 to 5 GeV^2. Events falling outside these two regions are eliminated.

The selection results after all cuts have been applied are shown in Table 3.4 on the following page. Altogether, 13,553 events with two leptons of same charge and 54,913

Table 3.4 – *Number of events selected in the data of experiments 7 to 27 in events with leptons of same sign or events with leptons of opposite sign, in the signal region (top) and the MMS region (bottom).*

Type	*On-resonance*		*Off-resonance*	
	Same-sign	Opposite-sign	Same-sign	Opposite-sign
		Signal region		
ee	2824	11928	0	18
$\mu\mu$	3980	16095	11	22
$e\mu$	3332	12985	2	16
μe	3417	13905	2	7
$\ell\ell$	13553	54913	15	63
		MMS region		
ee	7481	42825	7	127
$\mu\mu$	10937	58555	64	223
$e\mu$	8949	45525	30	79
μe	9225	50178	24	82
$\ell\ell$	36592	197083	125	511

events with two leptons of opposite charge have been selected in the signal region from the data of experiments 7 to 27.

Chapter 4

Fit design and results

THIS chapter presents the procedure used to extract Δm_d from the distributions of Δz. The results of the fits are also given, together with various consistency checks. Systematic errors are then estimated. Finally, the results are summarised and discussed.

An unbinned maximum likelihood fit is performed on the Δz distributions. The general form of the likelihood is:

$$\mathcal{L}(\Delta m_d, \vec{a}) = \prod_k \sum_i \alpha_i \left[\mathcal{P}_i \otimes \mathcal{R}_i\right] (\Delta z_k; \Delta m_d, \vec{a}), \tag{4.1}$$

where k runs over all events in the MMS signal region, i represents a given category of events, α_i is the fraction of this category in the full sample, $\mathcal{P}$ and $\mathcal{R}$ represent the time evolution and the detector response functions respectively, and $\vec{a}$ is the vector of all parameters except Δm_d. The different terms are detailed in the following sections.

4.1 Event classification

4.1.1 Definitions

The various categories we consider are based on two characteristics of the candidate leptons: their charge and their origin. They all correspond to different time evolutions and response functions.

The charges of the two candidate leptons define two types of events: same-sign events (SS) where the two candidate leptons have the same charge, and opposite-sign events (OS) where the two candidate leptons have opposite charge. This distinction exists on an event-by-event basis in real data as well as in Monte Carlo data.

Within each of these two types, the source of the lepton pair defines classes, which can be distinguished on an event-by-event basis only in Monte Carlo data. These classes are:

- *neutral* events: $\Upsilon(4S) \to B^0\overline{B}^0$;
- *charged* events: $\Upsilon(4S) \to B^+B^-$;
- *continuum* events (non-resonant e^+e^- interactions).

In addition, candidate leptons from neutral and charged events are classified into three different categories depending on the lepton origin. Let $\vec{x}_l$ be the (true) position of the production vertex of a candidate lepton, and $\vec{x}_B$ the (true) position of the decay vertex of the corresponding B. There are:

- *Primary* candidate leptons originating from the B decay vertex ($\vec{x}_l = \vec{x}_B$). They mainly consist of $B \to X\,\ell$, but can also come from $c\overline{c}$ resonances (e.g. $B \to J/\psi\,(\to \ell\,\ell\,)\,X$).
- *Secondary* candidate leptons, originating from a non-B decay vertex ($\vec{x}_l = \vec{x}_B + \vec{d}_D$). These are mainly leptons coming from charmed mesons produced by the decay chain: $B \to D\,(\to X\,\ell\,)\,Y$. It also includes candidate leptons from tau, kaon or pion decays, and candidate leptons produced in secondary interactions with the detector or the beam pipe.

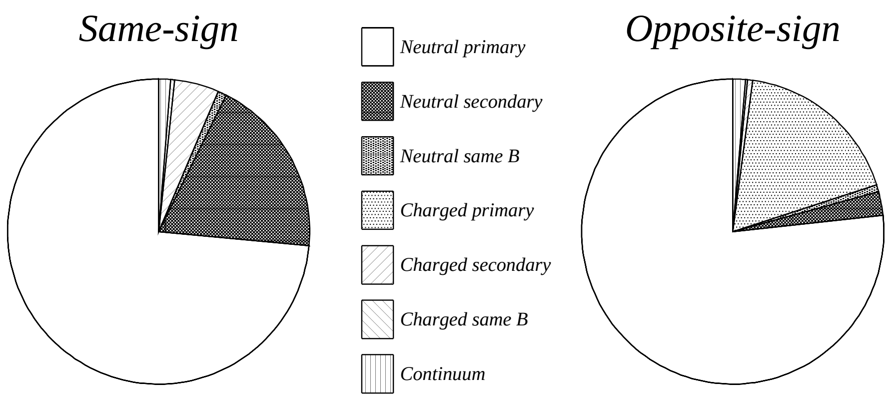

FIGURE 4.1 – *Pie charts of the various event categories in same-sign (left) and opposite-sign (right) types, as calculated in the Monte Carlosample.*

Categories are defined as follows:

1. *Primary* events, where both candidate leptons are primary and come from two different *B* decays.

2. *Secondary* events, where at least one candidate lepton is a secondary lepton and where the candidate leptons are coming from different *B* decays.

3. *Same B* events, where the candidate leptons come from the same *B*.

The list of categories is summarised in Table 4.1 on the next page together with their relative size, after all cuts (including tight MMS cuts) have been applied. The fractions are taken from Monte Carlo data. The relative size of the categories can be seen on Figure 4.1. Since there are almost no primary leptons from charged same-sign events, they are grouped with the secondary leptons into a “charged SS different *B*” category.

4.1.2 Fractions of categories

The relative fraction of each category is determined in the data from different quantities. As already stated, the signs of the leptons define OS and SS events.

Off-resonance data is analysed exactly the same way as on-resonance and Monte Carlo data in order to evaluate the fraction of continuum. This fraction is equal to the number of events selected from off-resonance data, scaled by the ratio of on-resonance to off-

Table 4.1 – *List of event categories and corresponding sizes calculated from Monte Carlo data after the full selection. The relative size of a category is given with respect to the class (neutral or charged) it belongs to. Quoted uncertainties are from the Monte Carlo statistics.*

Type	*Class*	*Category*	
Same-sign (19.37±0.21)%	Neutral (93.56±0.30)%	primary	(78.59±0.52)%
		secondary	(20.39±0.51)%
		same *B*	(1.02±0.13)%
	Charged (5.18±0.27)%	different *B*	(91.20±1.53)%
		same *B*	(8.80±1.53)%
	Continuum (1.26±0.14)%		
Opposite-sign (80.63±0.21)%	Neutral (79.94±0.24)%	primary	(95.93±0.13)%
		secondary	(3.17±0.12)%
		same *B*	(0.90±0.06)%
	Charged (18.72±0.24)%	primary	(95.92±0.28)%
		secondary	(2.95±0.24)%
		same *B*	(1.13±0.15)%
	Continuum (1.34±0.07)%		

resonance integrated luminosities (see Table 3.2 on page 45), and divided by the number of on-resonance events selected:

$$\alpha_{\mathrm{cont}} = \frac{N(\mathrm{off})}{N(\mathrm{on})}\frac{\mathcal{L}(\mathrm{on})}{\mathcal{L}(\mathrm{off})} \tag{4.2}$$

The fraction of neutral and charged events in the OS and SS classes is determined from experimental data using a fit to the MMS distributions, as explained below.

The fractions β_j of categories *within* charged and neutral classes are extracted from the Monte Carlo data, separately for same-sign and opposite-sign events. In the case of neutral events, these fractions depend on the mixing probability $\chi_d = \Delta m_d \tau_0$. They are extrapolated for any test value of χ_d from the Monte Carlo value χ_d^{MC} in the following way:

$$\beta_j = \frac{N_j^{\mathrm{SF}}}{N_0} \cdot \frac{\chi_d}{\chi_d^{\mathrm{MC}}} + \frac{N_j^{\mathrm{OF}}}{N_0} \cdot \frac{1-\chi_d}{1-\chi_d^{\mathrm{MC}}} \tag{4.3}$$

where j designates primary, secondary or same B categories, N_0 is the total number of neutral events in the corresponding event type (same-sign or opposite-sign), $N_0 = \sum_j (N_j^{\mathrm{SF}} + N_j^{\mathrm{OF}})$. N_j^{SF} is the number of same-flavour events in the category, and N_j^{OF} is the number of opposite-flavour events in the category. The same formula applies for same-sign and opposite-sign events. The fractions β_j are then multiplied by the corresponding class fraction obtained from the MMS fit to get the fractions α_i used in the likelihood expression of Equation (4.1) on page 59.

4.1.3 Missing mass squared fit

The fraction of neutral and charged events is determined by a binned likelihood fit of Monte Carlo MMS distributions to real data MMS distributions for SS and OS separately. The fit uses the `HMCMLL` routine of `CERNLIB` [48], which also considers the statistical errors of the Monte Carlo distributions. The distribution shapes come from the Monte Carlo: only the fractions are allowed to float in the fit, except the continuum fraction, which is fixed to the value calculated using Equation (4.2).

The neutral MMS distribution depends on Δm_d. In order to account for this dependence, neutral Monte Carlo events are reweighted in a similar way to sub-categories (see Equation (4.3)): neutral SS and OS distributions are separated into same-flavour and opposite-flavour distributions. The same-flavour distribution is multiplied by $\chi_d/\chi_d^{\mathrm{MC}}$, and the opposite-flavour distribution by $(1-\chi_d)/(1-\chi_d^{\mathrm{MC}})$. This is illustrated on Figure 4.2 on the next page. Since χ_d is small, the effect is much clearer for same-sign events.

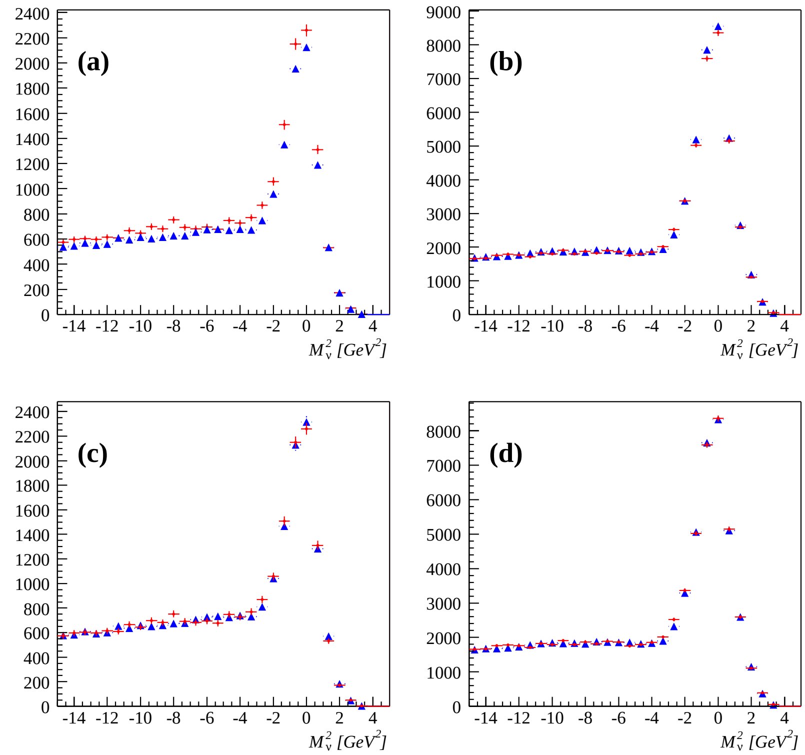

Figure 4.2 – *Reweighting of the neutral MMS distributions to take into account their dependence on* Δm_d*. Monte Carlo samples with* $\Delta m_d = 0.467\ ps^{-1}$ *(triangles) and* $\Delta m_d = 0.520\ ps^{-1}$ *(crosses) are compared* before *reweighting, for (a) neutral SS events and (b) neutral OS events. The comparison* after *reweighting the first Monte Carlo sample to* $\Delta m_d = 0.520\ ps^{-1}$ *is shown for (c) neutral SS events and (d) neutral OS events.*

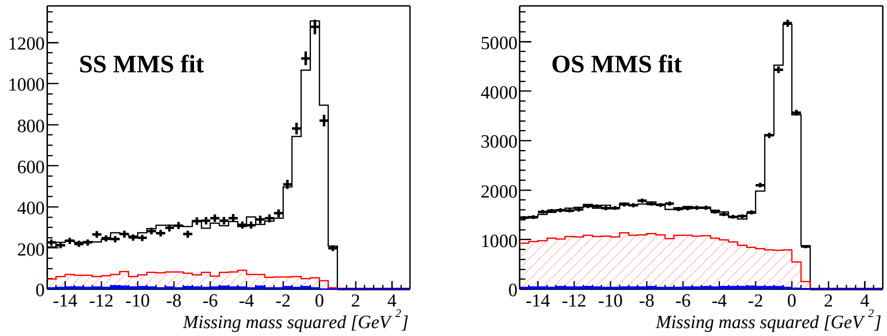

FIGURE 4.3 – *Fit of half of the available Monte Carlo sample to the other half for (a) SS events and (b) OS events. The result of the fit shows the continuum contribution (filled entries), the charged events contribution (hatched entries) and the neutral events contribution (empty entries). No reweighting has been made (the Monte Carlo value of χ_d is assumed).*

TABLE 4.2 – *Comparison between input and fitted Monte Carlo fractions.*

	Fractions in SS events		Fractions in OS events	
Class	*Input*	*Fitted*	*Input*	*Fitted*
Neutral	0.747	0.734 ± 0.015	0.511	0.510 ± 0.006
Charged	0.212	0.224 ± 0.015	0.454	0.456 ± 0.006
Continuum	0.042	0.042 (fixed)	0.034	0.034 (fixed)

The fit consistency was first checked by fitting half of the available sample Monte Carlo to the other half. The result is shown in Figure 4.3. Fitted and input values are compared in Table 4.2.

4.2 Time evolution

The time evolution functions $\mathcal{P}$ of the likelihood reflect the actual time dependence of the B mesons the leptons come from. In other words, this part of the likelihood does not take into account a possible distortion of this evolution by secondary leptons. (This will be accounted for in the resolution functions $\mathcal{R}$.) It does however contain mistag information, in the case of neutral events. The possible time dependence distributions thus reduce to three:

- Same-flavour (SF) and opposite-flavour (OF) events, in the "primary" or "secondary" categories of neutral events follow the distributions (see Equation (1.59) on page 14):

$$\mathcal{P}_{\mathrm{SF}}(\Delta t; \Delta m_d) = \frac{\exp\left(-\frac{|\Delta t|}{\tau_0}\right)}{4\tau_0} [1 - \cos(\Delta m_d \Delta t)] \frac{1}{\chi_d} \tag{4.4}$$

$$\mathcal{P}_{\mathrm{OF}}(\Delta t; \Delta m_d) = \frac{\exp\left(-\frac{|\Delta t|}{\tau_0}\right)}{4\tau_0} [1 + \cos(\Delta m_d \Delta t)] \frac{1}{1-\chi_d} \tag{4.5}$$

  where $\Delta t = t_1 - t_2$ is the true time difference between the two B mesons and τ_0 is the lifetime of the neutral B meson. These functions are normalised with the mixing probability χ_d (see on page 14).

  Defining ω_{SS} (ω_{OS}) as the fraction of OF (SF) events in the SS (OS) types, the time distributions for SS and OS events are:

$$\mathcal{P}_{\mathrm{SS}}(\Delta t; \Delta m_d, \omega_{\mathrm{SS}}) = (1 - \omega_{\mathrm{SS}}) \mathcal{P}_{\mathrm{SF}} + \omega_{\mathrm{SS}} \mathcal{P}_{\mathrm{OF}} \tag{4.6}$$

$$\mathcal{P}_{\mathrm{OS}}(\Delta t; \Delta m_d, \omega_{\mathrm{OS}}) = (1 - \omega_{\mathrm{OS}}) \mathcal{P}_{\mathrm{OF}} + \omega_{\mathrm{OS}} \mathcal{P}_{\mathrm{SF}} \tag{4.7}$$

  In the following, the quantities ω_{SS} and ω_{OS} are called "wrong-tag fractions". These are mainly due to J/ψ or fake leptons. Because of these fractions of wrongly-tagged events, SF and OF events differ from SS and OS events, respectively. What we call wrong-tag fractions, however, should not be confused with "mistag probabilities", i.e. the probability that an SF (OF) event is measured as an SS (OS) event.

- Charged B meson and charmed meson decays:

$$\mathcal{P}_{\exp}(\Delta t; \tau) = \frac{1}{2\tau} \exp\left(-\frac{|\Delta t|}{\tau}\right) \tag{4.8}$$

  This describes charged events and a fraction of continuum events. The lifetime τ corresponds to charged B meson or charmed mesons lifetimes.

- Prompt component:

$$\mathcal{P}_{\delta}(\Delta t) = \delta(\Delta t) \tag{4.9}$$

  Leptons coming from the same vertex (continuum or "same B" events) are described by this distribution.

The time distribution of events is inferred from the vertex position difference, assuming:

$$\Delta t = \frac{\Delta z}{\beta\gamma c}, \tag{4.10}$$

where $\beta\gamma = 0.425$ represents the Lorentz boost of the $\Upsilon(4S)$ rest frame with respect to the laboratory. The effect of the transverse motion of B mesons in the $\Upsilon(4S)$ rest frame is discussed in sub-section 4.7.2 on page 90.

4.3 Detector response function

The detector response functions of the likelihood take into account the imperfect resolution on the B meson decay vertex position measurement.

4.3.1 Detector resolution

The precision on the z position of the lepton production vertex itself is limited by the detector resolution, which affects all categories of leptons, regardless of their origin. The reconstructed position $z_l^{\rm rec}$ differs from the true position $z_l^{\rm true}$ by $\delta z_l = z_l^{\rm rec} - z_l^{\rm true}$ $(l = 1, 2)$. The detector resolution on Δz is then expressed by a sum of two Gaussian distributions, one for the core part, one for the tail part of the resolution:

$$\mathcal{R}_{\rm det}(\delta\Delta z; \sigma_z) = (1 - f_{\rm tail})\, G(\delta\Delta z; s_{\rm main}\sigma_z) + f_{\rm tail}\, G(\delta\Delta z; s_{\rm tail}\sigma_z) \tag{4.11}$$

where $\delta\Delta z = (z_1^{\rm rec} - z_2^{\rm rec}) - (z_1^{\rm true} - z_2^{\rm true})$, $f_{\rm tail}$ is the fraction of tail in the resolution, $s_{\rm main}$ and $s_{\rm tail}$ are global scale factors common to all tracks, $\sigma_z = \sqrt{\sigma_{z_1}^2 + \sigma_{z_2}^2}$ is the quadratic sum of event-by-event estimated errors on the lepton z vertex coordinates z_1 and z_2, and

$$G(x; \sigma) = \frac{1}{\sqrt{2\pi}\sigma} \exp\left(-\frac{x^2}{2\sigma^2}\right).$$

For notational simplicity, let $\overrightarrow{\rm res} = (f_{\rm tail}, s_{\rm main}, s_{\rm tail})$ be the vector of detector resolution parameters.

$J/\psi \to l^+ l^-$ events are used to obtain the resolution parameters. These events have passed exactly the same selection as the other events, except that the J/ψ veto and the cut on the opening angle between the two leptons are not applied. Figure 4.4 on the next page shows the agreement between the Δz distributions of primary events and J/ψ events.

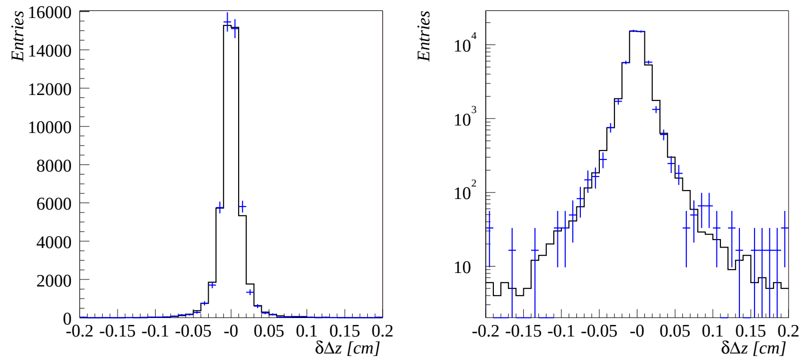

Figure 4.4 – *Comparison of $\delta\Delta z$ Monte Carlo distributions for primary events (histogram) and J/ψ events (crosses) scaled to the number of primary events.*

A J/ψ signal region and a J/ψ side-band region are defined in the two distributions of the invariant mass $M_{l^+l^-}$:

– Signal region: $3.00\ \mathrm{GeV}/c^2 < M_{e^+e^-} < 3.14\ \mathrm{GeV}/c^2$

$3.05\ \mathrm{GeV}/c^2 < M_{\mu^+\mu^-} < 3.14\ \mathrm{GeV}/c^2$

– Side-band region: $3.18\ \mathrm{GeV}/c^2 < M_{l^+l^-} < 3.50\ \mathrm{GeV}/c^2$

Figure 4.5 on the facing page shows the e^+e^- and $\mu^+\mu^-$ mass distributions in experimental data and Monte Carlo. The superimposed mass distributions for $e^\pm\mu^\mp$ candidates give a very good description of the shape of the background (non J/ψ events) in both the e^+e^- and $\mu^+\mu^-$ samples. Hence, the ratio α between the number of background events in the signal region and that in the side-bands can be taken from the $e^\pm\mu^\mp$ sample.

Events falling in the J/ψ side-band region are used to describe the background in the signal region. The side-band $\Delta z/\sigma_z$ distributions are scaled by α and subtracted from the signal region distributions. The resulting $\Delta z/\sigma_z$ distributions for e^+e^- and $\mu^+\mu^-$ are added. $\Delta z/\sigma_z$ is then fitted with a double Gaussian. (This is equivalent to fitting $\mathcal{R}_{\mathrm{det}}$ to Δz.) The result of the fit is shown in Figure 4.6 on page 70.

The parameters of $\mathcal{R}_{\mathrm{det}}$ are listed in Table 4.3 on the facing page.

4.3.2 Non-primary decays

The production vertex of a lepton and the decay vertex of the B meson it comes from only coincide in the case of "primary leptons", by definition. All other categories must therefore be compensated for the $\vec{d}_D$ shift (see sub-section 4.1.1 on page 60). This is done with the

TABLE 4.3 – *Parameters of the detector resolution fitted from experimental and Monte Carlo data.*

Parameter	*Real data*		*Monte Carlo*	
f_{main}	0.970	±0.004	0.970	±0.002
s_{main}	1.199	±0.011	1.138	±0.007
s_{tail}	5.3	±0.3	6.34	±0.27

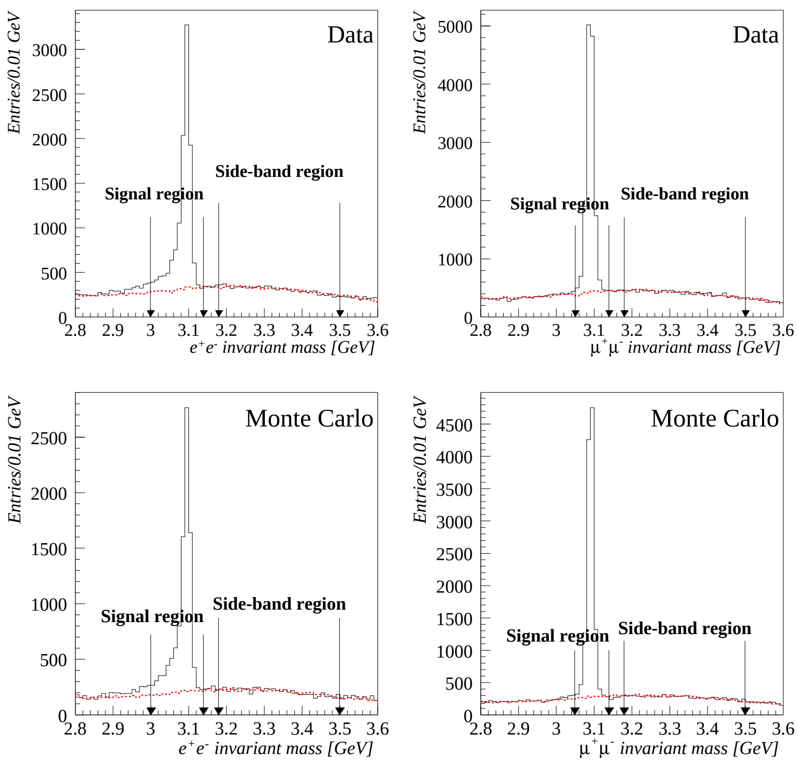

FIGURE 4.5 – *Invariant mass distributions of e^+e^- and $\mu^+\mu^-$ pair candidates (plain histograms, e^+e^- on the left, $\mu^+\mu^-$ on the right). Upper plots show experimental data distributions, lower plots show Monte Carlo distributions. In each case, the distribution of $e^\pm\mu^\mp$ events (dashed histograms) is superimposed, after normalisation to the side-band region.*

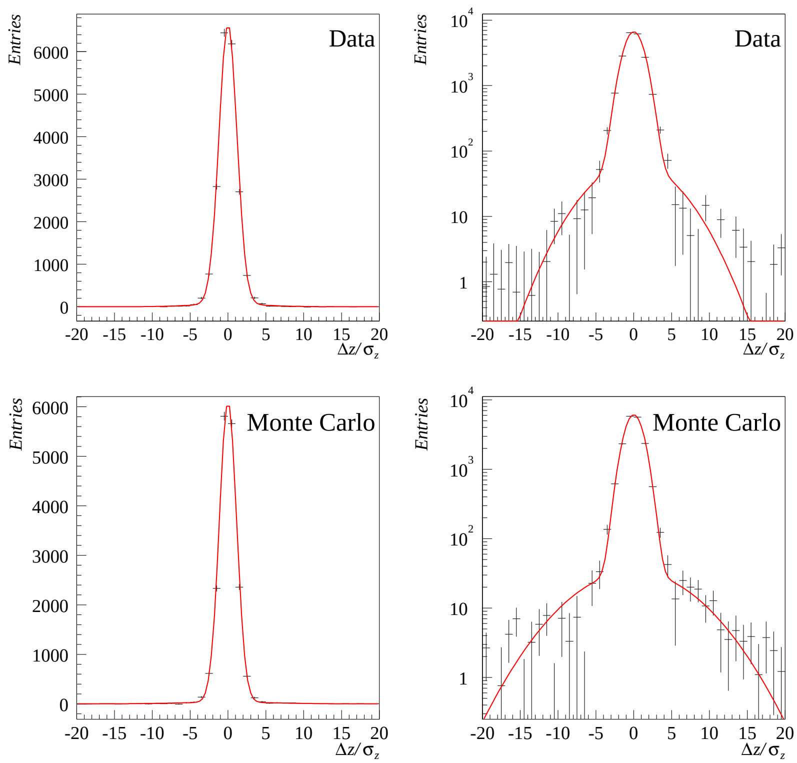

Figure 4.6 – $\Delta z/\sigma_z$ *distribution of* J/ψ *events after background subtraction, on a linear (left) and a logarithmic scale. The fitted double Gaussian curve is superimposed. Upper plots show experimental data distributions, lower plots show Monte Carlo distributions.*

following general function for “non-primary” leptons (see [49]):

$$\mathcal{R}^{l}_{\rm np}(\delta z_l;\tau_n,\tau_p) = f_p\, E_p\left(\delta z_l;\tau_p\right) + (1-f_p)\, E_n\left(\delta z_l;\tau_n\right) \tag{4.12}$$

where:

$$E_p(x;\tau) = \begin{cases} \frac{1}{\tau}\exp\left(-\frac{x}{\tau}\right) & \text{if } x > 0 \\ 0 & \text{otherwise} \end{cases}$$

$$E_n(x;\tau) = \begin{cases} \frac{1}{\tau}\exp\left(-\frac{x}{\tau}\right) & \text{if } x \le 0 \\ 0 & \text{otherwise} \end{cases}$$

with $\tau > 0$. Studies have shown that the effect of track fit errors σ_z had to be included in the τ parameters of E_p and E_n:

$$\tau_p = \tau_p^0 + \tau_p^1\, s\,\sigma_z \tag{4.13}$$

$$\tau_n = \tau_n^0 + \tau_n^1\, s\,\sigma_z \tag{4.14}$$

Here, s denotes the same global scale factor as in $\mathcal{R}_{\rm det}$. Since $\mathcal{R}_{\rm det}$ has two components, corresponding to $s_{\rm main}$ and $s_{\rm tail}$, there will also be two components in $\mathcal{R}_{\rm np}$: $\mathcal{R}^{\rm main}_{\rm np}$ with $s = s_{\rm main}$ and $\mathcal{R}^{\rm tail}_{\rm np}$ with $s = s_{\rm tail}$.

Finally, since each lepton can be a secondary lepton with different characteristics, two different $\mathcal{R}^{l}_{\rm np}$ contributions must be added to describe the total distribution $\mathcal{R}_{\rm np}$:

$$\mathcal{R}_{\rm np}(\delta\Delta z;\overrightarrow{\rm np}) = \alpha\mathcal{R}^{1}_{\rm np}(\delta\Delta z;\overrightarrow{\rm np}^1) + (1-\alpha)\mathcal{R}^{2}_{\rm np}(\delta\Delta z;\overrightarrow{\rm np}^2) \tag{4.15}$$

The parameters $\overrightarrow{\rm np} = (\overrightarrow{\rm np}^1,\overrightarrow{\rm np}^2,\alpha)$, where $\overrightarrow{\rm np}^l = (f_p,\tau_p^0,\tau_p^1,\tau_n^0,\tau_n^1)^l$ $(l = 1,2)$, are determined in a global fit including the full response function, as explained below.

4.3.3 Response function

The full response function $\mathcal{R}_{\rm tot}$ for each category is a convolution of the above functions:

- Primary events (3 parameters):

$$\mathcal{R}_{\rm tot}\left(\delta\Delta z;\sigma_z,\overrightarrow{\rm res}\right) = \mathcal{R}_{\rm det}\left(\delta\Delta z;\sigma_z,\overrightarrow{\rm res}\right) \tag{4.16}$$

- Non-primary events (12 additional parameters):

$$\mathcal{R}_{\rm tot}\left(\delta\Delta z;\sigma_z,\overrightarrow{\rm res},\overrightarrow{\rm np}\right) = \left\{\mathcal{R}_{\rm det}\otimes\left(f_\delta\delta + (1-f_\delta)\mathcal{R}_{\rm np}\right)\right\}\left(\delta\Delta z;\sigma_z,\overrightarrow{\rm res},\overrightarrow{\rm np}\right) \tag{4.17}$$

where f_δ is the fraction of a Dirac component, which is added to take into account primary leptons (in "same B" or "different B" categories) or leptons coming from the same vertex (in continuum events).

Parameters for $\mathcal{R}_{\text{det}}$ can be extracted from data, as described in sub-section 4.3.1 on page 67. All the parameters necessary to describe non-primary decays are extracted from Monte Carlo. A fit of the corresponding $\mathcal{R}_{\text{tot}}$ is performed on each category we consider, with $\mathcal{R}_{\text{det}}$ parameters extracted from the Monte Carlo. In the case of the charged different B category the time evolution $\mathcal{P}$ can be included in $\mathcal{R}_{\text{np}}$, since both $\mathcal{P}$ and $\mathcal{R}_{\text{np}}$ consist of exponentials.

The result of the $\mathcal{R}_{\text{tot}}$ fit is shown on Figures 4.7 to 4.10 on pages 74–77. The full list of parameters (except the $\mathcal{R}_{\text{det}}$ part) is given in Table 4.4 on the next page. Asymmetries in these distributions come from the tighter momentum cut on the first lepton which greatly reduces secondary first leptons. Second leptons then have a larger reconstructed z in average, and the distributions are stretched to positive values.

4.4 List of likelihood terms

The probability density functions used for each category are listed here.

4.4.1 Same-sign events

1. Primary neutral events:

$$P^{\text{SS}}_{\text{prim}}\left(\Delta z; \Delta m_d, \omega^{\text{SS}}_{\text{prim}}, \sigma_z, \overrightarrow{\text{res}}\right) = \mathcal{P}_{\text{SS}}\left(\frac{\Delta z}{\beta\gamma c}; \Delta m_d, \omega^{\text{SS}}_{\text{prim}}\right) \otimes \mathcal{R}_{\text{det}}(\delta\Delta z; \sigma_z, \overrightarrow{\text{res}}) \tag{4.18}$$

2. Secondary neutral events:

$$P^{\text{SS}}_{\text{sec}}\left(\Delta z; \Delta m_d, \omega^{\text{SS}}_{\text{sec}}, \sigma_z, \overrightarrow{\text{res}}, \overrightarrow{\text{np}}^{\text{SS}}_{\text{sec}}\right) = \mathcal{P}_{\text{SS}}\left(\frac{\Delta z}{\beta\gamma c}; \Delta m_d, \omega^{\text{SS}}_{\text{sec}}\right) \otimes \left[\mathcal{R}_{\text{det}} \otimes \mathcal{R}_{\text{np}}\right]\left(\delta\Delta z; \sigma_z, \overrightarrow{\text{res}}, \overrightarrow{\text{np}}^{\text{SS}}_{\text{sec}}\right) \tag{4.19}$$

TABLE 4.4 – *Full list of parameters for the description of the response function in non-primary events. The low statistics and large number of parameters cause some parameters to vanish for less significant categories.*

	$\overrightarrow{\mathrm{np}}^1$					$\overrightarrow{\mathrm{np}}^2$						
Category	f_p	τ_p^0	τ_p^1	τ_n^0	τ_n^1	f_p	τ_p^0	τ_p^1	τ_n^0	τ_n^1	α	f_δ
Neutral SS sec.	0.429	0.253	−0.453	0.937	0.303	0.111	−0.059	1.506	0.389	−0.356	0.557	0.000
Neutral SS same *B*	0.000			−0.044	0.581						1.000	0.000
Charged SS diff. *B*	0.518	1.758	0.207	1.858	−0.202	0.403	1.759	0.205	1.857	−0.202	0.669	0.097
Charged SS same *B*	0.000			0.411	−0.381	0.000			3.489	−2.159	0.900	0.000
Continuum SS	0.451	2.840	−1.430	0.548	0.474	0.451	2.840	−1.430	0.548	0.474	0.872	0.413
Neutral OS sec.	0.738	0.010	−0.005	0.766	0.195	0.380	−1.657	0.247	0.724	0.221	0.901	0.000
Neutral OS same *B*	0.285	−0.955	0.954	0.619	−0.145	0.051	0.113	1.058	−0.275	2.036	0.897	0.147
Charged OS sec.	0.221	−0.291	−0.692	0.317	−0.166	0.151	−0.176	−0.885	−1.537	3.421	0.895	0.000
Charged OS same *B*	0.000			0.334	−0.340						1.000	0.460
Continuum OS	0.000			5.917	−2.508	0.515	−0.922	2.819	0.921	0.356	0.086	0.546

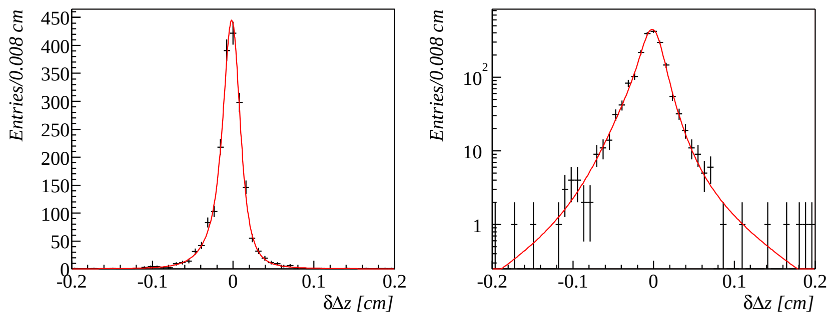

(a) Neutral SS secondary

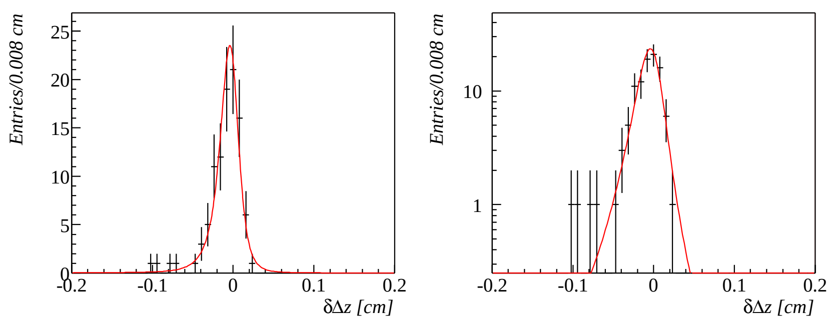

(b) Neutral SS same B

FIGURE 4.7 – *Distribution of $\Delta z^{rec} - \Delta z^{gen}$ for non-primary same-sign leptons (part 1), represented on a linear scale (left) and a logarithmic scale (right). The points are Monte Carlo data and the curve is the result of the $\mathcal{R}_{tot}$ fit.*

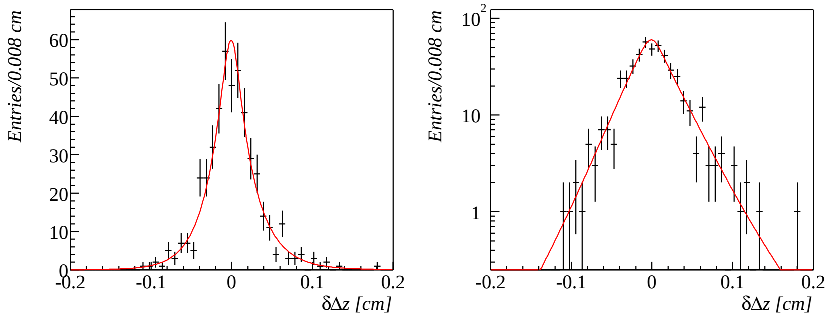

(a) Charged SS (leptons from different *B* mesons)

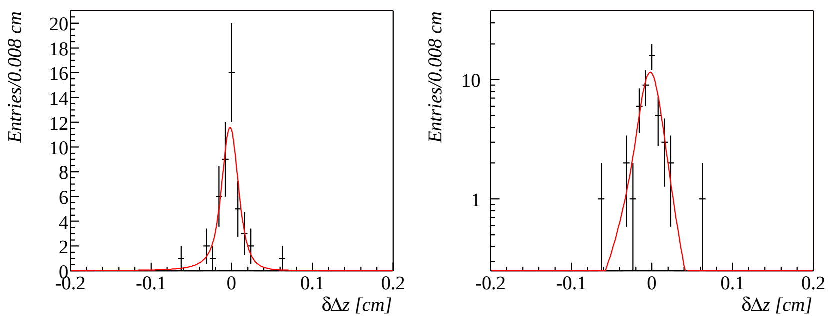

(b) Charged SS same *B*

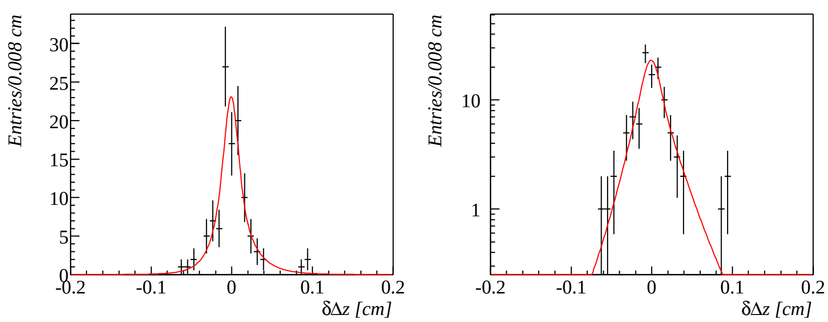

(c) Continuum SS

FIGURE 4.8 – *Distribution of $\Delta z^{rec} - \Delta z^{gen}$ for non-primary same-sign leptons (part 2), presented on a linear scale (left) and a logarithmic scale (right). The points are Monte Carlo data and the curve is the result of the $\mathcal{R}_{tot}$ fit.*

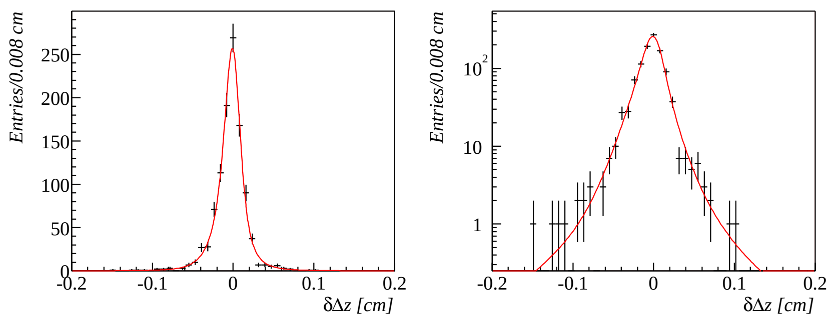

(a) Neutral OS secondary

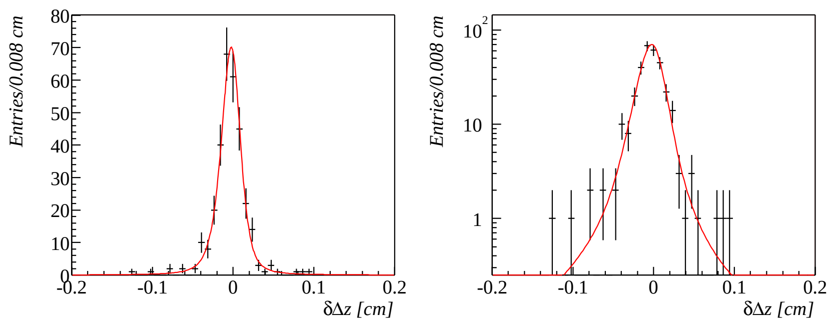

(b) Neutral OS same B

FIGURE 4.9 – *Distribution of $\Delta z^{rec} - \Delta z^{gen}$ for non-primary opposite-sign leptons (part 1), represented on a linear scale (left) and a logarithmic scale (right). The points are Monte Carlo data and the curve is the result of the $\mathcal{R}_{tot}$ fit.*

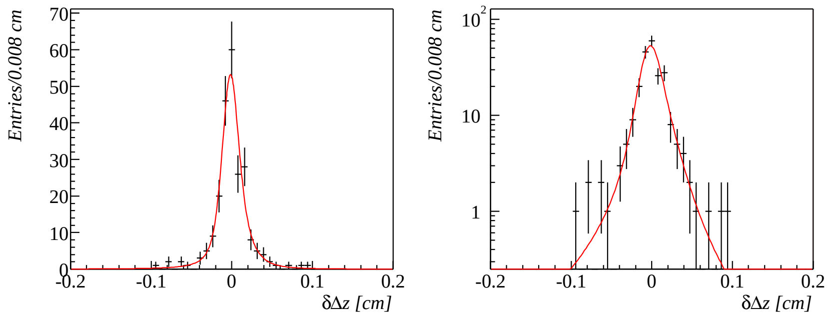

(a) Charged OS secondary

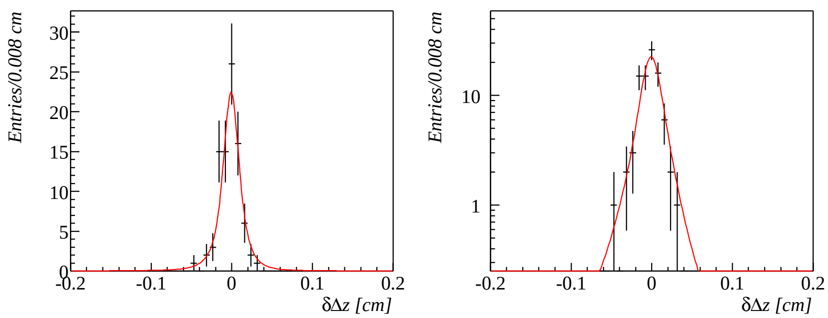

(b) Charged OS same *B*

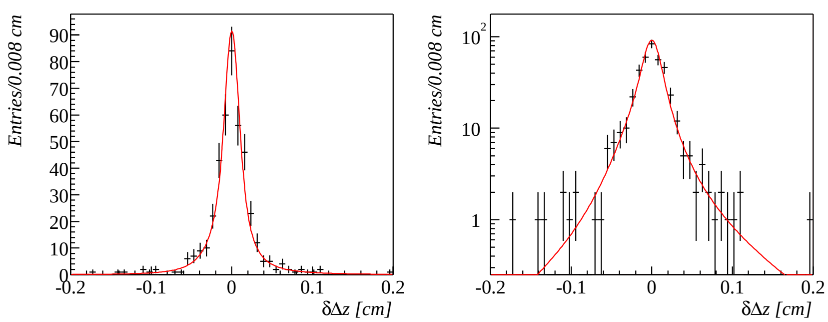

(c) Continuum OS

FIGURE 4.10 – *Distribution of $\Delta z^{rec} - \Delta z^{gen}$ for non-primary opposite-sign leptons (part 2), represented on a linear scale (left) and a logarithmic scale (right). The points are Monte Carlo data and the curve is the result of the $\mathcal{R}_{tot}$ fit.*

3. Same B neutral events:

$$P^{\mathrm{SS}}_{\mathrm{SB}}\Big(\Delta z;\sigma_z,\overrightarrow{\mathrm{res}},\overrightarrow{\mathrm{np}}^{\mathrm{SS}}_{\mathrm{SB}}\Big) = \Big[\mathcal{R}_{\mathrm{det}}\otimes\mathcal{R}_{\mathrm{np}}\Big]\Big(\Delta z;\sigma_z,\overrightarrow{\mathrm{res}},\overrightarrow{\mathrm{np}}^{\mathrm{SS}}_{\mathrm{SB}}\Big) \tag{4.20}$$

4. Different B charged events:

$$\begin{aligned} P^{\mathrm{SS}}_{\pm}\Big(\Delta z;\sigma_z,\overrightarrow{\mathrm{res}},\overrightarrow{\mathrm{np}}^{\mathrm{SS}}_{\pm}\Big) &= \Big[\mathcal{P}_{\mathrm{exp}}\otimes\mathcal{R}_{\mathrm{det}}\otimes\mathcal{R}'_{\mathrm{np}}\Big]\Big(\Delta z;\sigma_z,\overrightarrow{\mathrm{res}},\overrightarrow{\mathrm{np}}'_{\pm}\Big) \\ &= \Big[\mathcal{R}_{\mathrm{det}}\otimes\mathcal{R}_{\mathrm{np}}\Big]\Big(\Delta z;\sigma_z,\overrightarrow{\mathrm{res}},\overrightarrow{\mathrm{np}}^{\mathrm{SS}}_{\pm}\Big) \end{aligned} \tag{4.21}$$

5. Same B charged events:

$$\begin{aligned} &P^{\mathrm{SS}}_{\mathrm{SB}\pm}\Big(\Delta z;\sigma_z,\overrightarrow{\mathrm{res}},\overrightarrow{\mathrm{np}}^{\mathrm{SS}}_{\mathrm{SB}},f_\delta\Big) = \\ &\qquad f_\delta\,\mathcal{R}_{\mathrm{det}}(\Delta z;\sigma_z,\overrightarrow{\mathrm{res}}) + (1-f_\delta)\Big[\mathcal{R}_{\mathrm{det}}\otimes\mathcal{R}_{\mathrm{np}}\Big]\Big(\Delta z;\sigma_z,\overrightarrow{\mathrm{np}}^{\mathrm{SS}}_{\mathrm{SB}}\Big) \end{aligned} \tag{4.22}$$

6. Continuum events:

$$\begin{aligned} &P^{\mathrm{SS}}_{\mathrm{co}}\Big(\Delta z;\sigma_z,\overrightarrow{\mathrm{res}},\overrightarrow{\mathrm{np}}^{\mathrm{SS}}_{\mathrm{co}},f_\delta\Big) = \\ &\qquad f_\delta\,\mathcal{R}_{\mathrm{det}}(\Delta z;\sigma_z,\overrightarrow{\mathrm{res}}) + (1-f_\delta)\Big[\mathcal{R}_{\mathrm{det}}\otimes\mathcal{R}_{\mathrm{np}}\Big]\Big(\Delta z;\sigma_z,\overrightarrow{\mathrm{res}},\overrightarrow{\mathrm{np}}^{\mathrm{SS}}_{\mathrm{co}}\Big) \end{aligned} \tag{4.23}$$

4.4.2 Opposite-sign events

1. Primary neutral events:

$$P^{\mathrm{OS}}_{\mathrm{prim}}\Big(\Delta z;\Delta m_d,\omega^{\mathrm{OS}}_{\mathrm{prim}},\sigma_z,\overrightarrow{\mathrm{res}}\Big) = \mathcal{P}_{\mathrm{OS}}\left(\frac{\Delta z}{\beta\gamma c};\Delta m_d,\omega^{\mathrm{OS}}_{\mathrm{prim}}\right)\otimes\mathcal{R}_{\mathrm{det}}(\delta\Delta z;\sigma_z,\overrightarrow{\mathrm{res}}) \tag{4.24}$$

2. Secondary neutral events:

$$\begin{aligned} &P^{\mathrm{OS}}_{\mathrm{sec}}\Big(\Delta z;\Delta m_d,\omega^{\mathrm{OS}}_{\mathrm{sec}},\sigma_z,\overrightarrow{\mathrm{res}},\overrightarrow{\mathrm{np}}^{\mathrm{OS}}_{\mathrm{sec}}\Big) = \\ &\qquad \mathcal{P}_{\mathrm{OS}}\left(\frac{\Delta z}{\beta\gamma c};\Delta m_d,\omega^{\mathrm{OS}}_{\mathrm{sec}}\right)\otimes\Big[\mathcal{R}_{\mathrm{det}}\otimes\mathcal{R}_{\mathrm{np}}\Big]\Big(\delta\Delta z;\sigma_z,\overrightarrow{\mathrm{res}},\overrightarrow{\mathrm{np}}^{\mathrm{OS}}_{\mathrm{sec}}\Big) \end{aligned} \tag{4.25}$$

3. Same B neutral events:

$$P_{\mathrm{SB}}^{\mathrm{OS}}\left(\Delta z;\sigma_z,\overrightarrow{\mathrm{res}},\overrightarrow{\mathrm{np}}_{\mathrm{SB}}^{\mathrm{OS}},f_\delta\right) = \\ f_\delta\,\mathcal{R}_{\mathrm{det}}(\Delta z;\sigma_z,\overrightarrow{\mathrm{res}}) + (1-f_\delta)\left[\mathcal{R}_{\mathrm{det}}\otimes\mathcal{R}_{\mathrm{np}}\right]\left(\Delta z;\sigma_z,\overrightarrow{\mathrm{np}}_{\mathrm{SB}}^{\mathrm{OS}}\right) \tag{4.26}$$

4. Primary charged events:

$$P_{\pm}^{\mathrm{OS}}\left(\Delta z;\sigma_z,\overrightarrow{\mathrm{res}}\right) = \left[\mathcal{P}_{\mathrm{exp}}\otimes\mathcal{R}_{\mathrm{det}}\right]\left(\Delta z;\sigma_z,\tau_{B^\pm},\overrightarrow{\mathrm{res}}\right) \tag{4.27}$$

5. Secondary charged events:

$$P_{\pm}^{\mathrm{OS}}\left(\Delta z;\sigma_z,\overrightarrow{\mathrm{res}},\overrightarrow{\mathrm{np}}_{\pm}^{\mathrm{OS}}\right) = \left[\mathcal{P}_{\mathrm{exp}}\otimes\mathcal{R}_{\mathrm{det}}\otimes\mathcal{R}_{\mathrm{np}}\right]\left(\Delta z;\sigma_z,\overrightarrow{\mathrm{res}},\overrightarrow{\mathrm{np}}_{\pm}^{\mathrm{OS}}\right) \tag{4.28}$$

6. Same B charged events:

$$P_{\mathrm{SB}\pm}^{\mathrm{OS}}\left(\Delta z;\sigma_z,\overrightarrow{\mathrm{res}},\overrightarrow{\mathrm{np}}_{\mathrm{SB}}^{\mathrm{OS}},f_\delta\right) = \\ f_\delta\,\mathcal{R}_{\mathrm{det}}(\Delta z;\sigma_z,\overrightarrow{\mathrm{res}}) + (1-f_\delta)\left[\mathcal{R}_{\mathrm{det}}\otimes\mathcal{R}_{\mathrm{np}}\right]\left(\Delta z;\sigma_z,\overrightarrow{\mathrm{np}}_{\mathrm{SB}}^{\mathrm{OS}}\right) \tag{4.29}$$

7. Continuum events:

$$P_{\mathrm{co}}^{\mathrm{OS}}\left(\Delta z;\sigma_z,\overrightarrow{\mathrm{res}},\overrightarrow{\mathrm{np}},f_\delta\right) = \\ f_\delta\,\mathcal{R}_{\mathrm{det}}(\Delta z;\sigma_z,\overrightarrow{\mathrm{res}}) + (1-f_\delta)\left[\mathcal{R}_{\mathrm{det}}\otimes\mathcal{R}_{\mathrm{np}}{}_{\mathrm{co}}^{\mathrm{OS}}\right]\left(\Delta z;\sigma_z,\overrightarrow{\mathrm{res}},\overrightarrow{\mathrm{np}}_{\mathrm{co}}^{\mathrm{OS}}\right) \tag{4.30}$$

4.5 Corrections to the Monte Carlo

Simulated and experimental data slightly differ because the detector is not perfectly modelled by the `GEANT` program. In addition, physical quantities used by the `QQ` event generator correspond to the 2000 version of the *Review of Particle Physics*. Since Monte Carlo is used to extract fractions of categories, two corrections are made to the simulated data.

4.5.1 Branching fractions

The branching fraction for $B^0 \to D^{*-}\,\ell^+\nu_\ell$ events has significantly changed between the 2000 and 2003 averages:

$$\begin{aligned} \mathcal{B}(B^0 \to D^{*-}\,\ell^+\nu_\ell)_{\mathrm{QQ}} &= 0.0495 \\ \mathcal{B}(B^0 \to D^{*-}\,\ell^+\nu_\ell)_{\mathrm{PDG03}} &= 0.0553 \pm 0.0023 \end{aligned}$$

This is taken into account by reweighting these events by 1.12 ± 0.05 (the error will be used in the estimation of systematic errors).

4.5.2 Lepton and pion momentum distributions

Since MMS highly depends on momenta, discrepancies between Monte Carlo and data momentum distributions have a large effect on MMS distributions. Momentum distributions are, therefore, compared after the whole selection and the branching fractions reweighting, as shown in Figure 4.11 on the facing page. A reweighting factor is calculated for each bin of these histograms. Monte Carlo events are then reweighted according to the first lepton, second lepton and soft pion momentum used to calculate MMS.

4.6 Summary and results

The Monte Carlo $\Delta z/\sigma_z$ distribution for J/ψ events is fitted to get the Monte Carlo $\mathcal{R}_{\mathrm{det}}$ parameters. This $\mathcal{R}_{\mathrm{det}}$ is then convolved with the total $\mathcal{R}_{\mathrm{np}}$, which is used to describe events with non-primary leptons. Parameters of $\mathcal{R}_{\mathrm{np}}$ for all categories are then extracted from the corresponding Monte Carlo events (section 4.3.2 on page 68). These events have passed the whole selection.

The experimental data $\Delta z/\sigma_z$ distribution for J/ψ events is also fitted to get the $\mathcal{R}_{\mathrm{det}}$ parameters (section 4.3.1 on page 67). These parameters and $\mathcal{R}_{\mathrm{np}}$ parameters are then fixed in the Δm_d fit.

The B meson lifetimes are fixed to values given by the Heavy Flavor Averaging group (HFAG) [50] for summer 2003: $\tau_0 = 1.534 \pm 0.013$ ps, $\tau_\pm = 1.653 \pm 0.014$ ps.

Fractions of sub-categories (primary, secondary and same B) inside neutral and charged events are taken from the Monte Carlo (section 4.1.2 on page 61). They are recalculated

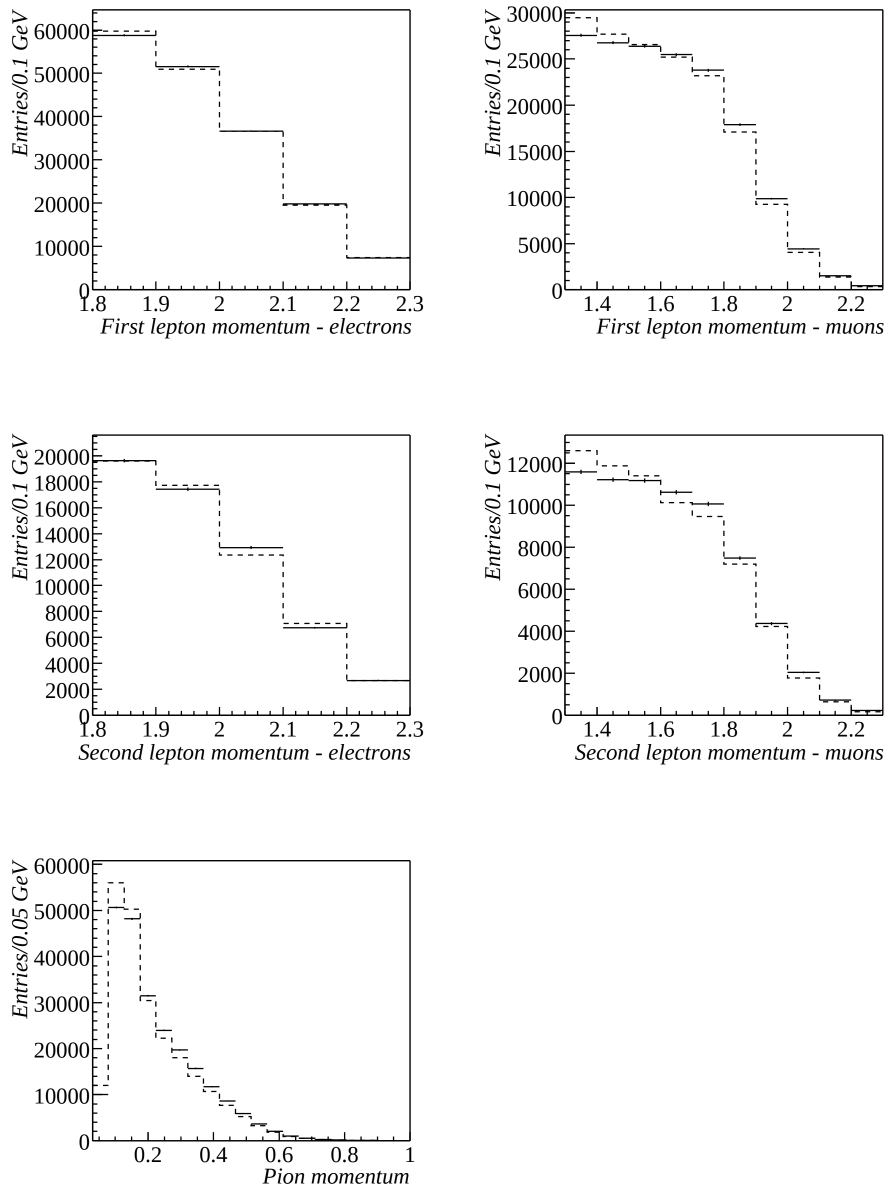

FIGURE 4.11 – *Momentum distribution for the first lepton candidate (electrons and muons), the second lepton candidates (electrons and muons) and the pion. The data points are compared with Monte Carlo (dashed) histograms.*

each time the value of Δm_d changes in the likelihood fit, according to Equation (4.3) on page 63.

The fraction of continuum events is set from the number of off-resonance events that have passed the selection, scaled by the ratio of on-resonance and off-resonance luminosities.

Neutral and charged fractions are determined from the experimental data using the MMS fit (section 4.1.3 on page 63). This MMS fit is performed each time the value of Δm_d changes during the likelihood fit.

Finally, three out of the four wrong-tag fractions are set to the Monte Carlo values in a way similar to other fractions (see Equation (4.3) on page 63):

$$\omega_i = \frac{N_i^{\mathrm{OF}} \cdot \frac{1-\chi_d}{1-\chi_d^{\mathrm{MC}}}}{N_i^{\mathrm{OF}} \cdot \frac{1-\chi_d}{1-\chi_d^{\mathrm{MC}}} + N_i^{\mathrm{SF}} \cdot \frac{\chi_d}{\chi_d^{\mathrm{MC}}}} \tag{4.31}$$

where i designates the neutral SS secondary, OS primary or OS secondary categories. These fractions proved to be beyond the sensitivity of the fit.

The likelihood $\mathcal{L}$ (Equation (4.1) on page 59) is calculated on all selected experimental events. Using `MINUIT`, we try to minimise the quantity:

$$-2\ln\mathcal{L}\left(\Delta m_d, \omega_{\mathrm{prim}}^{\mathrm{SS}}\right) + \Delta\overrightarrow{\mathrm{res}}^{T} \cdot \left(V^{-1}\right) \cdot \Delta\overrightarrow{\mathrm{res}} \tag{4.32}$$

where the mass difference Δm_d and the wrong-tag fraction for the neutral SS primary events, $\omega_{\mathrm{prim}}^{\mathrm{SS}}$, are floated. Initial values for these parameters are set to the current world average and the reweighted Monte Carlo value, respectively. The detector resolution parameters $\overrightarrow{\mathrm{res}}$ are constrained to the values obtained from the J/ψ fit by an additional Gaussian term, in order to include the statistical error on the determination of these parameters. V^{-1} is the covariance matrix obtained from the J/ψ fit, and $\Delta\overrightarrow{\mathrm{res}}$ is the vector difference between test values and J/ψ fit values.

4.6.1 Consistency check

We performed a fit to the Monte Carlo sample, in which the value of Δm_d is known. To do so, `mixed`, `charged`, `charm` and `uds` were split in two sets, set 1 and set 2. The samples of each sets were added to form "on-resonance" Monte Carlo, consisting of 13% `mixed`, 13% `charged`, 28% `charm` and 46% `uds` events. Separate samples of one set were then used to fit the combined Monte Carlo of the other set. Fit results are presented on Figures 4.12

TABLE 4.5 – *Result of the fit on the two Monte Carlo subsets compared to input values. The input values and errors for detector resolution parameters correspond to the outcome of the J/ψ fit. Only statistical errors are shown.*

Parameters	*Input*	*Set 1*	*Set 2*
Δm_d [ps^{-1}]	0.467	0.470 ± 0.010	0.477 ± 0.009
$\omega_{\mathrm{SS}}^{\mathrm{prim}}$	0.031	0.020 ± 0.017	0.037 ± 0.017
f_{main}	0.970 ± 0.002	0.971 ± 0.002	0.974 ± 0.002
s_{main}	1.138 ± 0.007	1.134 ± 0.007	1.132 ± 0.007
s_{tail}	6.3 ± 0.3	6.0 ± 0.3	6.0 ± 0.3

to 4.15 on pages 84–85 and summarised in Table 4.5. Fitted values are consistent with the input value of $\Delta m_d = 0.467\ \mathrm{ps}^{-1}$.

4.6.2 Fit result

Minimising expression (4.32) on the preceding page on all selected events of experiments 7 to 27 (150 million $B\overline{B}$ events), we found: $\Delta m_d = 0.519 \pm 0.006\ \mathrm{ps}^{-1}$ (statistical error only). The fit results are summarised in Table 4.7 on page 87 and presented on Figures 4.17 to 4.19 on pages 88–89. The corresponding fractions of events are listed in Table 4.6 on page 86.

4.6.3 Additional checks

The robustness of the fit was tested on experimental data by two additional checks. First, a separate fit of SS and OS events was performed. Second, the neutral B meson lifetime τ_0 was released. The results are presented in Table 4.7 on page 87. The fitted values of Δm_d, $\omega_{\mathrm{SS}}^{\mathrm{prim}}$ and the detector resolution parameters are consistent with the outcome of the nominal fit. The fitted value of τ_0 is consistent with the current world average: $\tau_0 = 1.534 \pm 0.013$ ps.

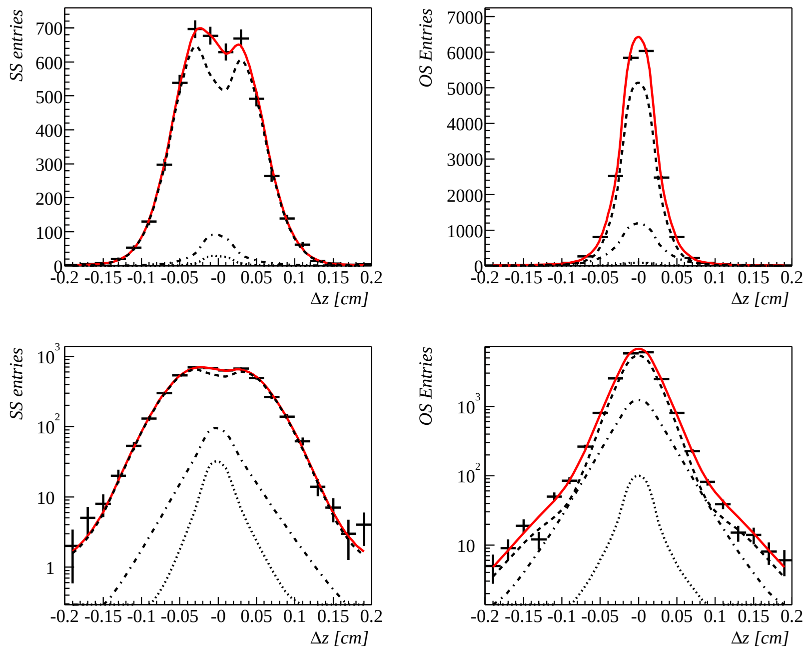

Figure 4.12 – *Δz distributions of same-sign (left) and opposite-sign (right) events in the Monte Carlo set 1. The superimposed solid curve is the total fit result, i.e. the sum of the fitted distributions of neutral events (dashed curve), charged events (dashed-dotted curve) and continuum events (dotted curve). Upper plots have a linear vertical scale.*

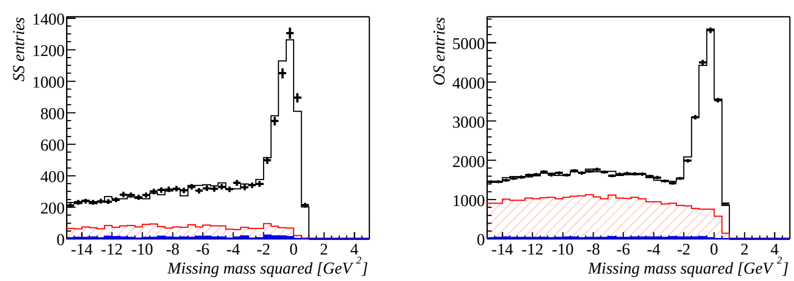

Figure 4.13 – *MMS distributions of same-sign (left) and opposite-sign (right) events in the Monte Carlo set 1. The superimposed histogram is the result of the fit, including the continuum contribution (filled entries), the charged events contribution (hatched entries) and the neutral events contribution (empty entries).*

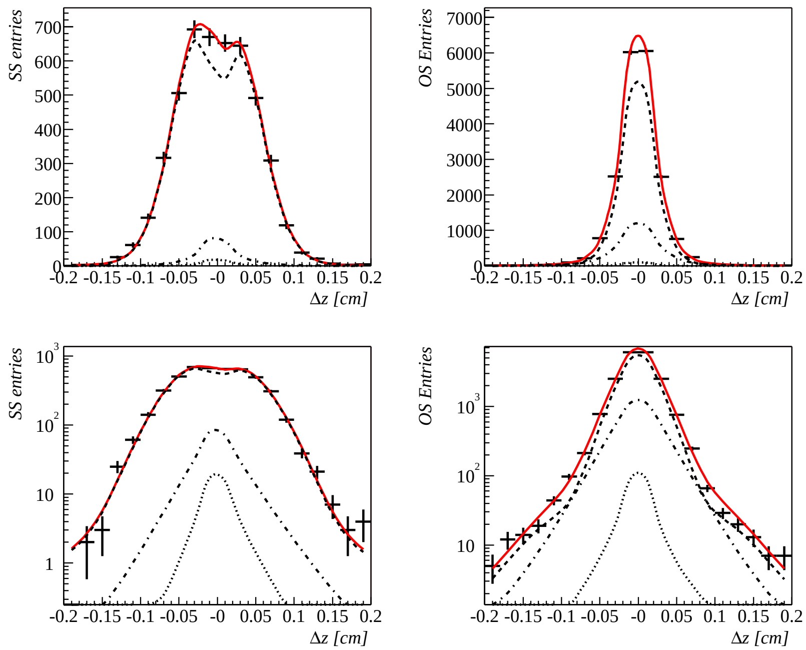

FIGURE 4.14 – *Δz distributions of same-sign (left) and opposite-sign (right) events in the Monte Carlo set 2. The superimposed solid curve is the total fit result, i.e. the sum of the fitted distributions of neutral events (dashed curve), charged events (dashed-dotted curve) and continuum events (dotted curve). Upper plots have a linear vertical scale.*

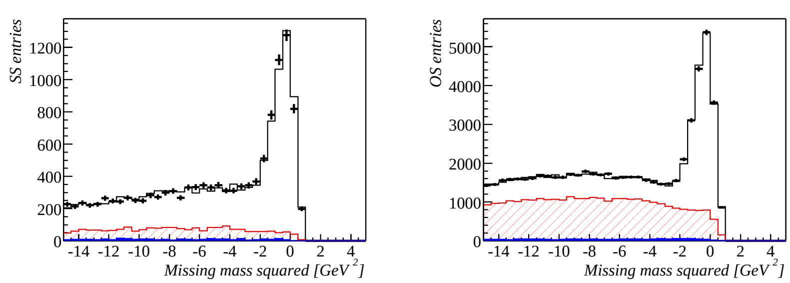

FIGURE 4.15 – *MMS distributions of same-sign (left) and opposite-sign (right) events in the Monte Carlo set 2. The superimposed histogram is the result of the fit, including the continuum contribution (filled entries), the charged events contribution (hatched entries) and the neutral events contribution (empty entries).*

Table 4.6 – *List of event categories and corresponding sizes obtained with the value of Δm_d fitted to data. The relative size of a category is given with respect to the class it belongs to. Quoted uncertainties come from the Monte Carlo statistics.*

Type	*Class*	*Category*	
Same-sign	Neutral	primary	(78.53±0.38)%
(19.37±0.16)%	(93.73±0.22)%	secondary	(20.43±0.37)%
		same B	(1.03±0.09)%
	Charged	different B	(91.20±1.15)%
	(4.82±0.19)%	same B	(8.80±1.15)%
	Continuum		
	(1.45±0.11)%		
Opposite-sign	Neutral	primary	(95.99±0.10)%
(80.63±0.16)%	(81.14±0.17)%	secondary	(3.13±0.08)%
		same B	(0.88±0.05)%
	Charged	primary	(95.94±0.21)%
	(17.36±0.17)%	secondary	(2.94±0.18)%
		same B	(1.12±0.11)%
	Continuum		
	(1.50±0.05)%		

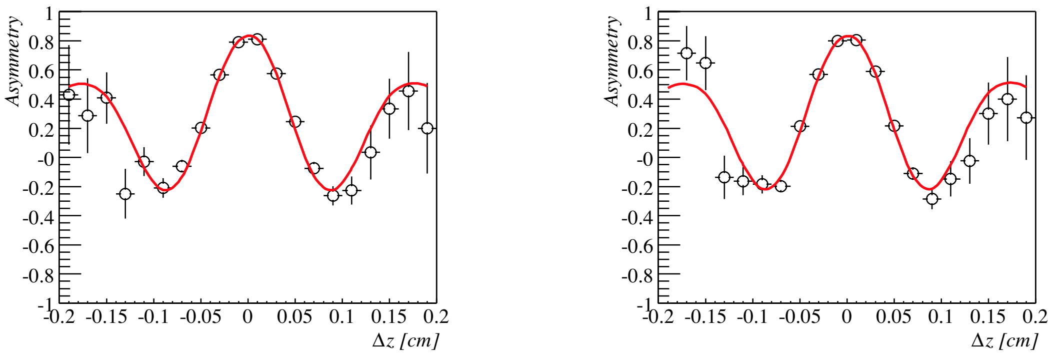

FIGURE 4.16 – *Mixing asymmetry in the Monte Carlo set 1 (left) and 2 (right). The result of the fits is superimposed.*

TABLE 4.7 – *Result of the nominal fit compared with additional check fits on SS events only, OS events only, and with floated neutral B meson lifetime.*

Parameters	*Nominal*	*SS only*	*OS only*	*Lifetime*
Δm_d [ps^{-1}]	0.519 ± 0.006	0.513 ± 0.009	0.527 ± 0.008	0.521 ± 0.007
τ_0 [ps]	1.534 (fixed)	1.534 (fixed)	1.534 (fixed)	1.546 ± 0.011
$\omega_{\mathrm{SS}}^{\mathrm{prim}}$	0.012 ± 0.006	0.015 ± 0.01	—	0.016 ± 0.012
f_{main}	0.963 ± 0.004	0.964 ± 0.003	0.962 ± 0.004	0.963 ± 0.004
s_{main}	1.161 ± 0.008	1.186 ± 0.009	1.161 ± 0.008	1.160 ± 0.009
s_{tail}	4.32 ± 0.21	4.64 ± 0.21	4.20 ± 0.22	4.29 ± 0.22

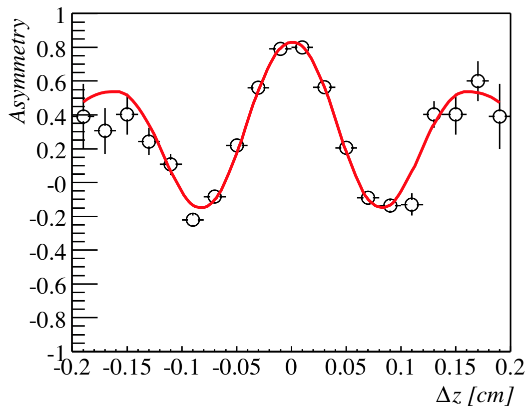

FIGURE 4.17 – *Mixing asymmetry in the experimental data. The result of the fit is superimposed.*

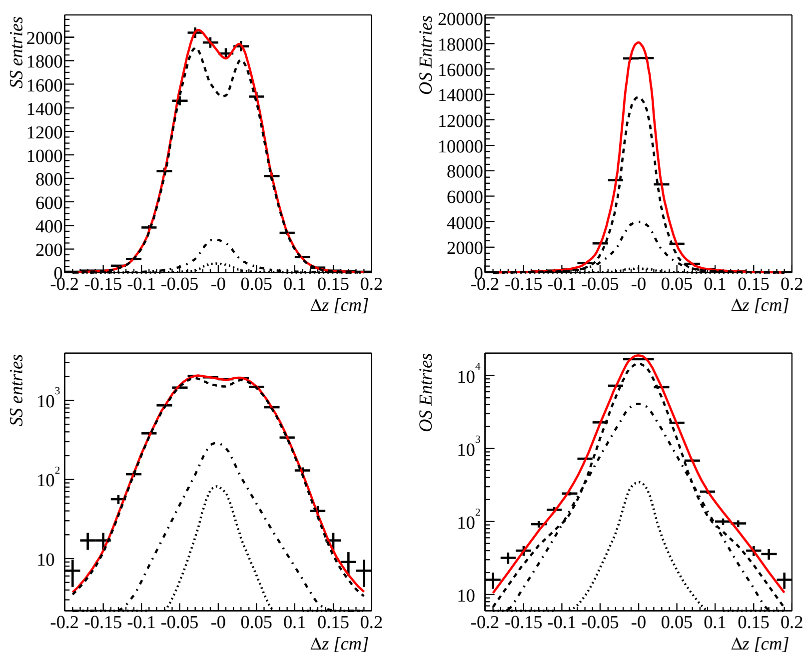

FIGURE 4.18 – *Δz distributions of same-sign (left) and opposite-sign (right) events in the data of experiments 7 to 27. The superimposed solid curve is the total fit result, i.e. the sum of the fitted distributions of neutral events (dashed curve), charged events (dashed-dotted curve) and continuum events (dotted curve). Upper plots have a linear vertical scale.*

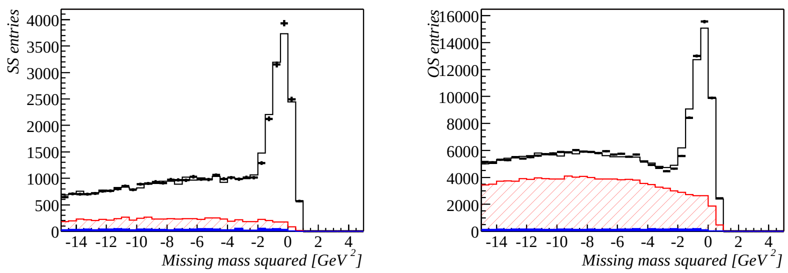

FIGURE 4.19 – *MMS distributions of same-sign (left) and opposite-sign (right) events in the the data of experiments 7 to 27. The superimposed histogram is the result of the fit, including the continuum contribution (filled entries), the charged events contribution (hatched entries) and the neutral events contribution (empty entries).*

4.7 Systematic errors

4.7.1 Physics parameters

The B lifetimes τ_0 and $\tau_\pm$ are used as input parameters in the fit and are set to the current world averages. The error on these averages are propagated to Δm_d by varying each lifetime by plus and minus one standard deviation and repeating the fit.

Monte Carlo is reweighted to account for the difference between the current world average of $\mathcal{B}(B^0 \to D^{*-}\, \ell^+\, \nu_\ell)$ and the event generator value (see section 4.5.1 on page 80). The reweighting factor is 1.12 ± 0.05, where the error corresponds to the error on the world average. This error is propagated by varying the reweighting factor by plus and minus one standard deviation and repeating the fit, in a similar way as for the lifetimes.

4.7.2 Detector resolution

The statistical error in the determination of the detector resolution parameters is automatically included in the fit by an additional Gaussian constraint (see Equation (4.32) on page 82). Two effects should, however, be taken into account in the systematic error. First, the B mesons momentum in the $\Upsilon(4S)$ frame is neglected when the time difference Δt is approximated by $\Delta z/\beta\gamma c$ (Equation (4.10) on page 67). Second, the resolution on Δz is estimated from J/ψ events.

In the Monte Carlo, the generated decay vertex position of the B mesons is known. The distribution of $\Delta z^{\text{meas}} - \Delta z^{\text{gen}}$, where Δz^{meas} is the measured Δz and Δz^{gen} is the generated Δz, gives the true Δz resolution. True resolution parameters are extracted from this distribution in the same way as for $\mathcal{R}_{\text{det}}$. The Monte Carlo sample is then split into 20 subsamples, and the fit is repeated for each subsample, alternately with $\mathcal{R}_{\text{det}}$ parameters and true resolution parameters. $\mathcal{R}_{\text{np}}$ parameters were refitted with the true resolution before performing the second series of fit. A histogram is then filled with the differences between the two fitted values of Δm_d (see Figure 4.20 on the facing page). The mean value of this histogram provides the systematic error due to the first effect mentioned above. We find $\langle \delta\Delta m_d \rangle = -1.67 \pm 0.57\ \text{ns}^{-1}$. We add this shift to the systematic error.

The second effect proved to be impossible to determine in the same way. Results obtained with this method were clearly inconsistent with the Monte Carlo input value of Δm_d: the average bias was more than $+0.030\ \text{ps}^{-1}$. In order to take the kinematic approximation

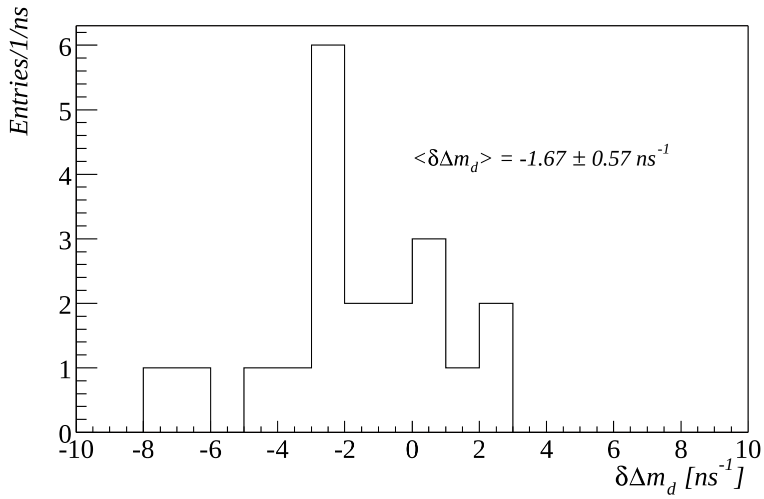

FIGURE 4.20 – *Histogram of the differences between fitted values of Δm_d with the nominal resolution and the true resolution, for each of the 20 Monte Carlo subsets.*

into account, we thus estimated the overall fit bias from the Monte Carlo. The outcome of the fit on the two Monte Carlo subsets (see Table 4.5 on page 83) shows an average bias of $+6.5 \pm 6.5$ ns^{-1} with respect to the input value of 0.467 ps^{-1}. The fitted value of Δm_d was corrected for this bias and the error was added to the systematic error. This correction takes into account all possible bias included in the Monte Carlo.

4.7.3 Non-primary decays

The Δz distributions of non-primary decays have an additional component $\mathcal{R}_{\rm np}$, whose parameters are determined by a fit to Monte Carlo. In order to propagate the errors of this fit to the Δm_d fit, each parameter should be varied, and the fit should be repeated.

Only neutral SS secondary events, however, represent a significant fraction of the total sample. All parameters of the corresponding $\mathcal{R}_{\rm np}$ were varied by plus or minus their statistical error and the Δm_d fit was repeated. The variations on Δm_d were then added using the covariance matrix of the $\mathcal{R}_{\rm np}$ fit.

All other non-primary categories represent less than 5% of the event type they belong to. The effect of the error on the corresponding $\mathcal{R}_{\rm np}$parameters is, therefore, expected to be negligible.

4.7.4 Event fractions

The event fractions are extracted from Monte Carlo data in two different ways: classes fractions come from the MMS fit; categories fractions and wrong-tag fractions directly come from corresponding Monte Carlo fractions reweighted according to the test value of Δm_d.

The MMS fit returns the ratio of neutral to charged event fractions with an error. The error takes into account statistical errors on the Monte Carlo and the experimental data. Since the Monte Carlo sample is significantly smaller than the real data sample, this error is dominated by the Monte Carlo statistics and is considered as a systematic error. In order to estimate it, we repeat the Δm_d fit twice, always using the returned fraction plus (resp. minus) the returned error.

As for categories and wrong-tag fractions, we estimate the corresponding error from the Monte Carlo statistical error. Each fraction is varied by plus or minus one standard error and the fit is repeated.

The fraction of continuum is determined from the number of selected events in the off-resonance sample. The corresponding statistical error is propagated to Δm_d by varying this fraction by plus or minus one standard error and repeating the fit.

We also estimated systematic effects of the Monte Carlo by fitting without momentum reweighting, by varying the Monte Carlo fake rates by ±5% and by varying the branching fractions of $D \to X\ell\nu_\ell$ decays by plus and minus their error. The resulting shifts in the fitted value of Δm_d were all less than 0.05%. We, therefore, assumed that systematic effects of the Monte Carlo were negligible with respect to the errors due to limited Monte Carlo statistics.

4.7.5 Summary

Systematic errors are summarised in Table 4.8 on the facing page. We add them in quadrature and find the final result, after correcting for the fit bias:

$$\Delta m_d = 0.513 \pm 0.006\,(\text{stat}) \pm 0.008\,(\text{syst})\ \text{ps}^{-1}. \tag{4.33}$$

TABLE 4.8 – *Summary of Δm_d systematic errors. The total shows the sum in quadrature of all errors. Note that the unit is ns^{-1}.*

Source	*Effect on Δm_d [ns^{-1}]*	
Neutral B lifetime	−2.85	+2.66
Charged B lifetime	+0.39	−0.40
$\mathcal{B}(B^0 \to D^{*-}\, \ell^+\, \nu_\ell)$	−0.02	+0.01
$\mathcal{R}_{\text{det}}$	+1.67	
$\Delta z/\beta\gamma c$	+6.45	
Neutral SS secondary $\mathcal{R}_{\text{np}}$	−0.41	+0.85
Fractions		
SS classes	−0.62	+0.61
OS classes	−0.30	+0.30
Continuum	+0.56	+0.59
SS neutral	+3.48	−3.42
SS charged	−0.09	+0.09
OS neutral	−1.29	+1.29
OS charged	−0.06	+0.06
Wrong-tag fractions	−0.19	+0.19
Total	−8.21	+8.16

4.8 Discussion of the result

The above result is in agreement with the current world average compiled by the *Heavy Flavor Averaging Group* for Summer 2003: $\Delta m_d = 0.502 \pm 0.007$ ps^{-1}(including statistical and systematic errors).

The measurement presented in this work is the most accurate single measurement of Δm_d to date. Adding systematic and statistical errors in quadrature amounts to an error comparable to the error on the world average. This measurement, therefore, significantly improves the knowledge of Δm_d.

systematic errors, however, are of the same order as statistical errors. One reason is the huge experimental data sample used for this measurement. Another reason is, conversely, the small amount of Monte Carlo statistics available, compared to experimental data. This results in large systematic errors in the determination of parameters from the Monte Carlo, especially the fractions of same-sign neutral events. Finally, the lifetime of the neutral B meson also represents a large source of systematic error. As shown in Table 4.7 on page 87, releasing this parameter simply transfers the corresponding systematic error to a statistical error on Δm_d. Indeed, adding in quadrature the 0.006 ps^{-1} error on the nominal fit outcome to the 0.003 ps^{-1} systematic error due to τ_0 equals the 0.007 ps^{-1} statistical error of the simultaneous Δm_d and τ_0 fit.

Previous time-dependent Δm_d measurements contributing to the world average are compared with this measurement in Figure 4.22 on page 96. The most significant contributions come from the two B-factories of the BaBar and Belle collaborations. These include[1]:

– exclusive analyses: fully reconstructed hadronic decays [52, 53] and $B^0 \to D^* \ell \nu_\ell$ decays [54, 55];

– inclusive reconstruction of $B^0 \to X \ell \nu_\ell$ decays (dilepton analyses) [56, 57];

– partial reconstruction of $B^0 \to D^* \pi$ decays [58].

All these analyses were performed on a sample of similar size, about five times smaller than the sample used in the present analysis. The corresponding mixing asymmetries are compared in Figure 4.21 on the next page. The excellent purity of the soft pion sample allows a clear asymmetry curve compared to most other measurements.

[1]See Reference [51] for a review of all measurements at B-factories.

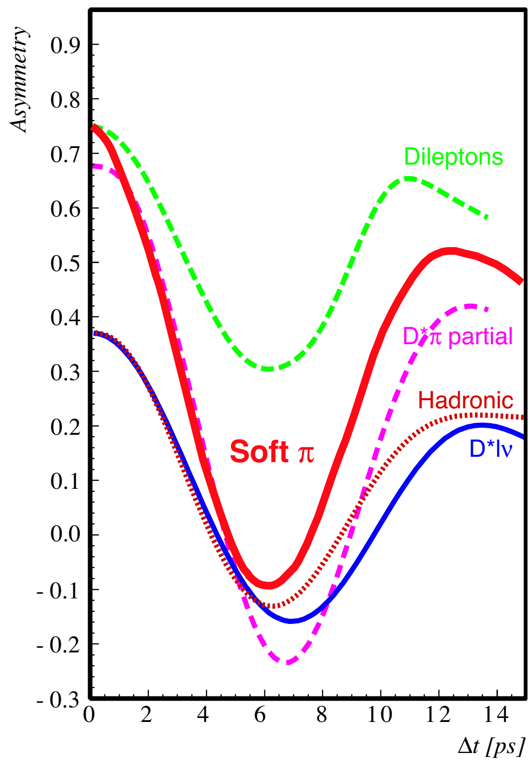

FIGURE 4.21 – *Comparison of mixing asymmetries of all Belle measurements.*

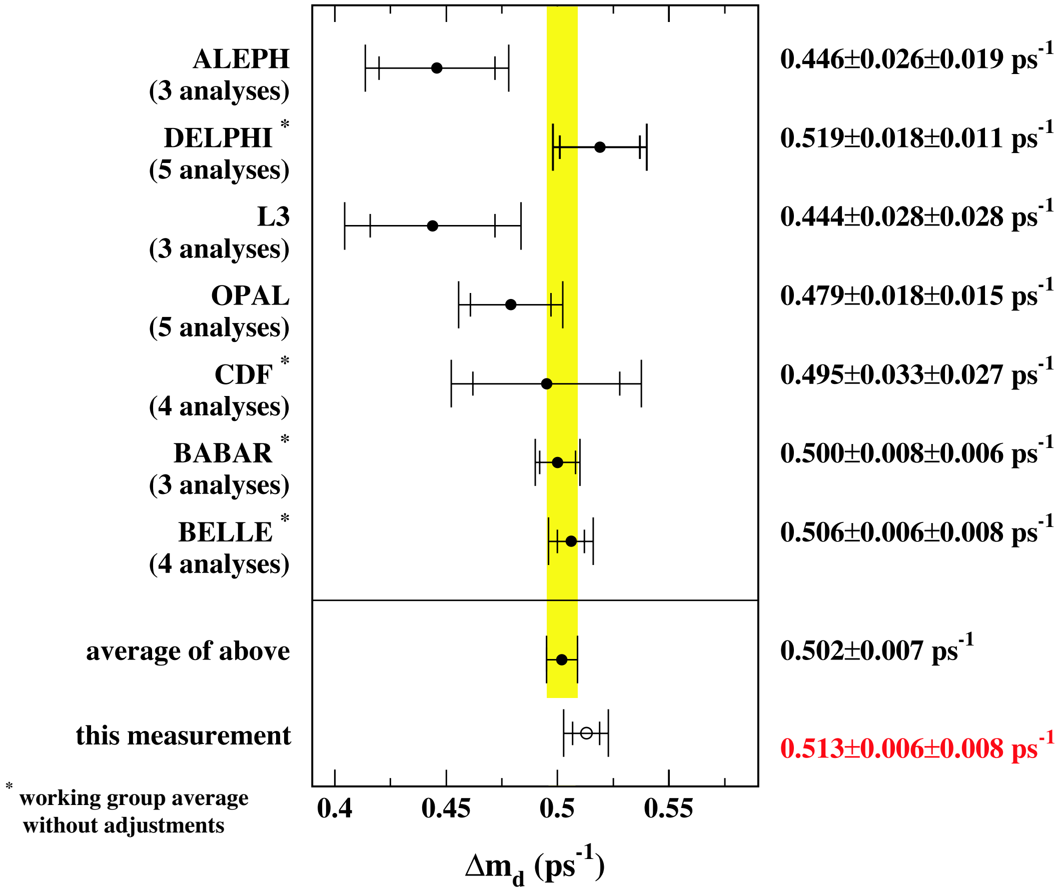

Figure 4.22 – *Summary of previous time-dependent Δm_d measurements, compared with the measurement presented in this work (HFAG averages for Summer 2003).*

This work began as a refinement of the Belle dilepton analysis. In spite of the much larger amount of available statistics, the selected number of events proves to be significantly smaller in this work than in the dilepton analysis; the selection efficiency ratio between the two is 5%. The main reason, in addition to the soft pion selection, is the very tight cut on the first lepton momentum. The amount of selected charged B events is, however, reduced by a factor of six in the SS sample, and by a factor of three in the OS sample. Neutral background and continuum events are greatly reduced by the partial reconstruction as well. Altogether, the signal over background ratio is increased by a factor 2.3–2.4. As a result, the statistical error and systematic errors are reduced by a factor 1.3.

Concerning implications in the “quest” for CP violation, Δm_d is an essential ingredient for the calculation of indirect *CP* violation parameters. It, however, only contributes to a small part of the overall systematic errors on such measurements (see for example [59]). No significant improvement is expected with the improvement of Δm_d measurements. On the other hand, Δm_d is directly related to the CKM matrix element V_{td}, which primarily accounts for CP violation in the Standard Model:

$$|V_{td}| \propto \sqrt{\Delta m_d}\sqrt{B_B} f_B.$$

Unfortunately, theoretical uncertainties on $\sqrt{B_B} f_B$ amount to 20%. Although improvements are expected from lattice calculations [60], the error on Δm_d is again negligible. This will change in a near future, with the measurement of Δm_s at hadron colliders. The following quantity will then be available experimentally:

$$\frac{|V_{td}|}{|V_{ts}|} = \xi \sqrt{\frac{m_{B_d}}{m_{B_s}}} \sqrt{\frac{\Delta m_d}{\Delta m_s}}, \quad \xi = \frac{\sqrt{B_B} f_B}{\sqrt{B_{B_s}} f_{B_s}}.$$

In the ratio ξ, theoretical uncertainties are reduced by a factor 2. A high accuracy on Δm_d will, therefore, be of great importance after the measurement of Δm_s.

Finally, recent measurements have set limits on $|q/p|$ and $\Delta\Gamma$ [61]. These limits are beyond the sensitivity of our measurements and justify the hypotheses we made on the time-dependent mixing probability functions (see Equation 1.31 on page 11).

Conclusion

The measurement of the $B^0\overline{B}^0$ mixing parameter Δm_d was carried out on a sample of 152 million $B\overline{B}$ pairs collected by the Belle detector over 3 years (2000–2003). Semi-leptonic events were selected by looking for two leptons of high momentum, as in the previous dilepton analyses. In order to reduce the charged B meson background, additional constraints were set to favour the decay $B^0 \to D^*(D^0\pi)\,\ell\,\nu_\ell$, which only exists at first order in the neutral B meson sector. This method was originally used in time-integrated decays by the CLEO collaboration. Because of the very large available sample of $B\overline{B}$ pairs, selection criteria could be tightened to purify the events from secondary decays. The number of fully selected same-sign and opposite-sign events are, respectively:

$$\begin{aligned} N_{\mathrm{SS}} &= 13,553 \\ N_{\mathrm{OS}} &= 54,913 \end{aligned}$$

with a signal over background ratio of 2.8 for same-sign events and 3.5 for opposite-sign events.

An unbinned likelihood fit was then simultaneously performed on the Δz distributions of same-sign and opposite-sign events to extract Δm_d. Various time-dependent probabilities were used to describe the signal and the multi-fold background. The detector resolution was deduced from events compatible with a J/ψ decay, where Δz is known to be zero. Finally, since the pion selection induces an asymmetry between the two leptons, rather complicated analytical functions had to be added to describe non-primary decays in the likelihood. The parameters of these functions were determined from Monte Carlo data. The contribution of each component was determined from Monte Carlo as well, either through a fit to the partially reconstructed neutrino missing mass squared, or directly from reweighted Monte Carlo samples. The fit parameters were: Δm_d, the wrong-tag fraction of primary same-sign neutral events and the parameters of the detector resolution. We made various consistency checks on the Monte Carlo and on the experimental data. Systematic effects were also estimated. We found:

$$\Delta m_d = 0.513 \pm 0.006(\text{stat}) \pm 0.008(\text{syst}).$$

This is the most precise Δm_d measurement at present. It is in agreement with previous results, and significantly contributes to the world average of this parameter.

Within a few years, the error on Δm_d may become a limiting factor on the determination of related CKM matrix parameters, especially after the measurement of Δm_s, the strange B^0 meson counterpart of Δm_d. Higher accuracy will then be required. Reducing the statistical error will certainly be made possible by the high expected statistics from B-factories. The reduction of systematic errors, however, may prove to be more difficult.

As far as this analysis is concerned a more precise determination of the B meson lifetimes would have a significant effect. Alternatively, the neutral B meson lifetime could be simultaneously measured, thus transferring this systematic error to the statistical error, which scales with the amount of available statistics. The small amount of available Monte Carlo with respect to the experimental data is another crippling source of error that should be soon corrected with the production of new Monte Carlo. A larger Monte Carlo sample may also help understand the background better and, perhaps, simplify the shape of non-primary decay functions. Finally, future measurements using this method should optimise the selection criteria. Most limits used in this analysis were set before the complete analysis, including the fit, had been performed. More feedback from the fitting stage to the selection stage could help increase the reconstruction efficiency without worsening the signal over background ratio.

Da steh ich nun, ich armer Tor!
Und bin so klug als wie zuvor;
Heiße Magister, heiße Doktor gar [. . .]
Daß ich erkenne, was die Welt
Im Innersten zusammenhält,
Schau alle Wirkenskraft und Samen
Und tu nicht mehr in Worten kramen.

— Goethe, *Faust*, First part

Appendix A
The Micromegas detector

MICROMEGAS, a novel and promising gaseous detector, has been studied in the framework of this thesis as a candidate for the LHCb inner tracker.

Micromegas was introduced in 1995 [62] to answer the demand for high-resolution tracking detectors with very high rate capabilities. The coming generation of accelerators, in particular LHC at C , indeed require such fast and robust devices. The research and development of this detector has opened the way to a very large range of applications, not only in high-energy physics, but also in astrophysics, medical imaging or neutron physics (see for example [63–65]).

The main characteristics of Micromegas are summarised in the first section of this appendix. In spite of its many interesting features, Micromegas showed a great sensitivity to highly ionising particles in intense flux of hadron beams, leading to discharge phenomena. A detailed study of breakdowns is reported in the second section.

> Il s'appelait Micromégas, nom qui convient fort à tous les grands.
>
> — Voltaire, *Micromégas*, Chapitre 1

A.1 The MICROMEsh GAseous Structure

Micromegas is a parallel-plate avalanche gas chamber, with a single amplification stage. It

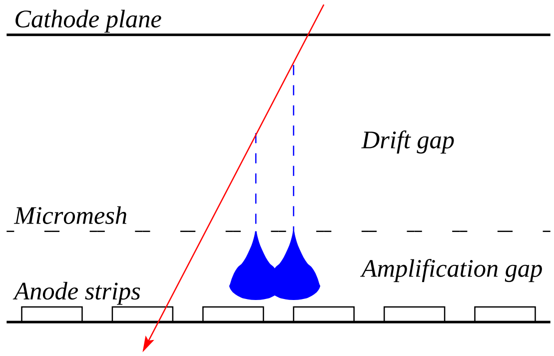

FIGURE A.1 – *Simplified scheme of Micromegas. A particle crosses the chamber and creates two electron-ion pairs. The drift of electrons and the amplification avalanches are shown.*

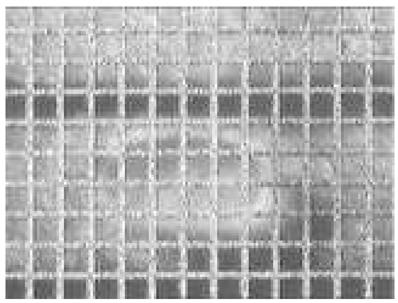

FIGURE A.2 – *Top view of the amplification gap showing the mesh, a spacer and strips (enlarged 80 times).*

consists of a conversion and drift space, limited by a cathode plane and a micromesh, on top of a narrow amplification gap located between the micromesh and anode readout strips. As represented on figure A.1, crossing particles create electron-ion pairs in the upper gap. The free electrons then drift toward the amplification gap, where a strong electric field generates an avalanche which is finally collected on the strips as an induction signal.

The anode is a simple printed circuit board with copper strips on an epoxy substrate. The micromesh is a thin (3 μm) electro-formed Nickel grid of $39 \times 39\ \mu\text{m}^2$ holes at a 50.8 μm pitch. It is stretched and laid down on small polyamid spacers deposited on the strips to precisely maintain the size of the 100 μm amplification gap (see figure A.2). The cathode is made of a thin aluminized Mylar® foil placed 3 mm above the mesh.

The electric field is remarkably homogeneous throughout the whole chamber. It ex-

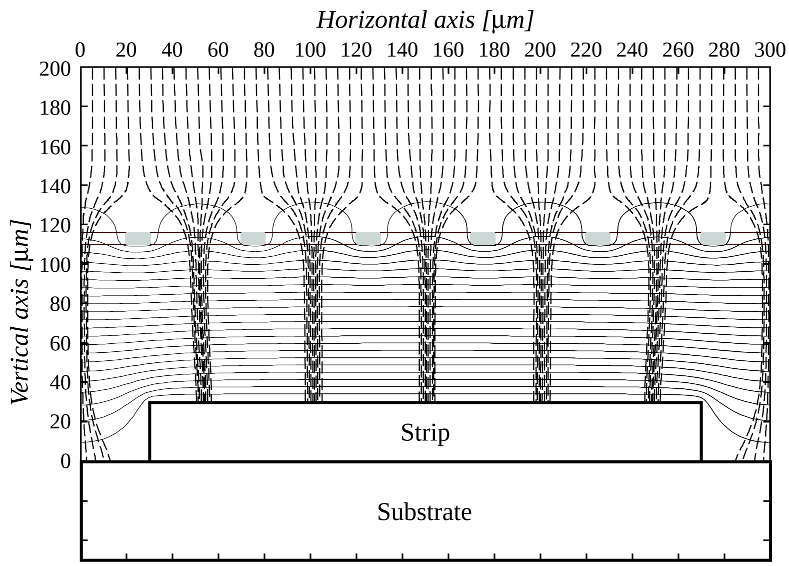

FIGURE A.3 – *Electron drift lines (dashed) and equipotential lines near the strips simulated using Maxwell and Garfield.*

hibits a funnel-like shape at the junction of the drift and amplification gaps, as shown on figure A.3. In this region, drift lines of electrons coming from the conversion gap are narrowed toward the centre of the mesh holes, thus ensuring a complete permeability of the grid to electrons created by the ionisation. The size of the drift line tube in the amplification gap depends on the electric field ratio between the two regions of the chamber. The field configuration and drift lines were calculated using Maxwell [66] and Garfield [67]. The geometry corresponds to a drift gap of 3 mm, an amplification gap of 110 μm, with strips of 240 μm width and 30 μm height placed every 300 μm. The substrate has the electrical properties of Vacrel®, strips are defined as Copper, and the mesh and the cathode are defined as Nickel. The cathode voltage is set to -1000 V, the mesh voltage to -450 V and the strips are grounded.

Finally, the chamber is filled with a mixture of a light, noble gas (e.g. Argon) and a polyatomic gas (e.g. isobutane i-C_4H_{10}). The light gases indeed allow avalanche multiplication at lower electric fields than complex gases. In addition, molecules of noble gas won't capture free electrons, except if they have been ionised. However, light gases easily fall into a permanent discharge operation: the ionised molecules return to their ground state by emitting photons which have enough energy to generate a new multiplication. The polyatomic gas, called "quencher", regulates this behaviour, mainly by absorbing the emitted photons in rotational and vibrational energy states, or by dissociation and elastic collisions. Typical mixtures used in Micromegas consist of 10%–20% quencher added to a noble gas.

A.2 Breakdown study

Although Micromegas showed outstanding performances in relatively clement environments, allowing a spatial resolution of 14 μm [69], breakdown phenomena in high flux beams of hadrons have appeared to be the main limiting factor of gain and rate. Three different causes of breakdown were identified [70]: spontaneous breakdown due to local defects, rate-induced breakdowns and breakdowns generated by high ionisations in hadron beams. Beam tests at the Paul Scherrer Institut (PSI) were undertaken in order to understand better the underlying mechanism of the last category of breakdown. In this section, we describe the experimental setup used in these tests, and give the results and their physical interpretation.

A.2.1 Experimental setup

The PSI accelerator facility delivers high intensity pion beams of low momentum. The beam magnets were adjusted to select 215 MeV/*c* positive pions and 350 MeV/*c* negative pions, which is close the minimum ionisation energy for pions. Typical beam sizes of 5.5 cm FWHM in both transverse directions were recorded using two 5×5 mm^2 scintillators

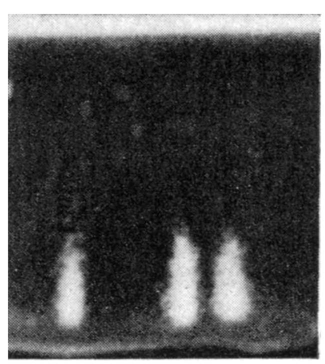

Figure A.4 – *Photography of electron avalanches in a gas chamber [68].*

in coincidence (see figure A.5). The scintillators were mounted on a remote controlled scanner, allowing a precise determination of the beam profile. The total particle rate in the chamber could then be calculated by integrating the measured rate at a given position to the whole detector area, with a precision of 20% or better. The highest intensity of 60 MHz was obtained with the positive pion beams.

The Micromegas detector used in these tests had an active area of 15×15 cm^2, a strip pitch of 200 μm, an amplification gap of 75 μm and a conversion gap of 6 mm. This large conversion gap, as compared to standard 3 mm gaps, was meant to compensate for the lower primary charge yield in light gas mixtures. All strips were connected to the same high voltage through a 1 MΩ resistor (see figure A.6 on the next page). The mesh was grounded and the cathode was set to negative high voltage. 32 strips were equipped with a fast front-end electronic chip, the STAR4 amplifier developed at C [71], for efficiency measurements. Two plastic scintillators located on both sides of the chamber at the position of these strips were used in coincidence to trigger the read-out electronics and measure the number of incoming particles. They were covering an area of 2×100 mm^2 along the strips. Another set of 48 strips were summed at the input of a slow charge amplifier for measurements of gain and primary charge distribution (see below). The remaining strips were grouped by eight. The read-out electronics was successfully protected against sparks by double-stage circuits consisting in a pair of head-to-tail diodes.

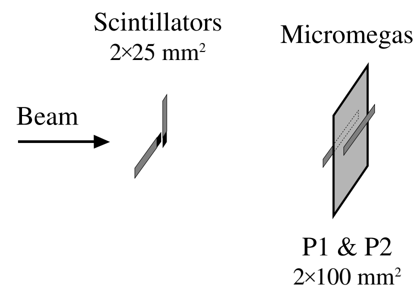

FIGURE A.5 – *Experimental setup used for beam tests at PSI.*

Several different gas mixtures were used during the tests. We will focus on two of them: 90% noble gas (Argon or Helium) with 10% isobutane.

A.2.2 Model of breakdown mechanism

According to Raether's experimental observations (see [68], p. 126), sparks occur in parallel plate chambers when the number of charge carriers in the avalanche exceeds a threshold R, of the order of 10^8. Since the total number of carriers in an avalanche is the product of the number of primary charges N_p and the gain G, a breakdown would occur when N_p

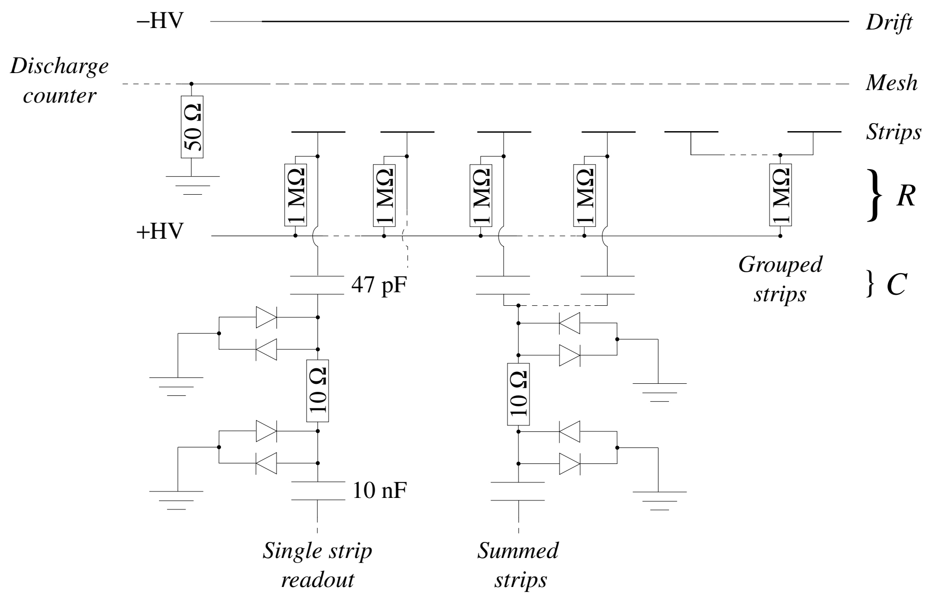

Figure A.6 – *Electronic setup used for beam tests at PSI.*

exceeds R/G. The discharge probability can then be predicted by knowing the probability density distribution $\phi(q)$ for the production of a total primary charge between q and $q + dq$. The discharge probability is indeed the probability that a primary charge greater than R/G is produced. It is simply given by

$$\mathcal{P}(\text{discharge}) = \int_{R/G}^{\infty} \phi(q)\, dq$$

assuming that $\phi(q)$ is normalised.

A precise measurement of $\phi(q)$ is needed in order to verify this model. This was done at low gain g, where no discharge occurs, by recording the amplitude spectrum of mesh signals through a calibrated charge amplifier. Alternatively, the signal of the 48 grouped strips was used. The total number N_{tot} of particles crossing the mesh, respectively the 48 strips, was also precisely determined. Each bin i of the spectrum then contained the number N_i of events having a total charge between Q_i and $Q_i + \Delta Q$. N_i/N_{tot} gave the probability for each incident particle to generate such a total charge. A fit to this normalised and discrete spectrum finally allowed us to extract $\phi(q \cdot g)/\Delta Q$, and thus $\phi(q)$.

This measurement depends on a precise knowledge of the gain over a wide range of amplification voltage. The standard gain calibration using a ^{55}Fe source does not allow us

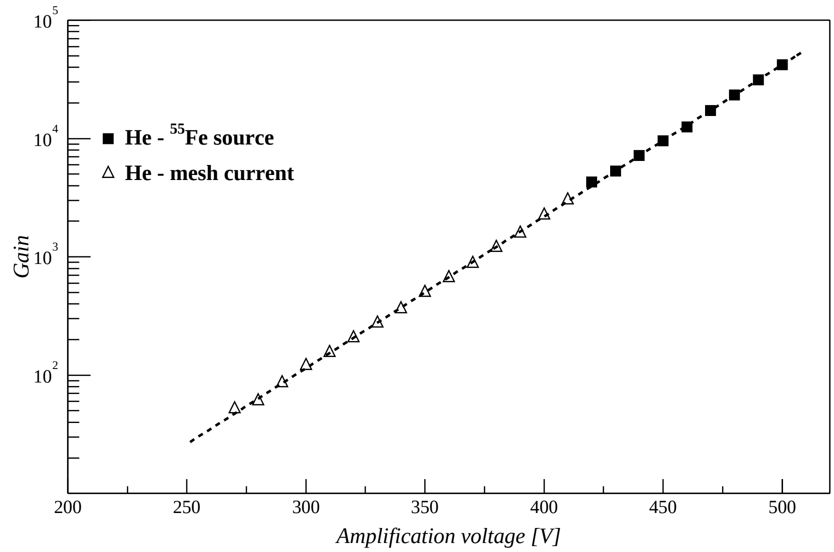

FIGURE A.7 – *Gain of the detector as a function of the mesh voltage. The calibration was performed using an iron source or by measuring the mesh current.*

to cover lower gains used to measure $\phi(q)$. This, however, can be achieved by measuring the current I in the chamber: $I = r \times N_p \times e \times G$, where r is the rate of incident particles and $N_p \times e$ is the average amount of primary charge produced in the conversion gap by minimum ionising particles. The current is measured on the mesh, grounded through a 50 Ω resistor. This of course only works if the discharge current is completely negligible. The result of this calibration for the Helium-isobutane mixture is shown on figure A.7. Both methods agree very well and are nicely fitted by an exponential.

A.2.3 Highly ionising particles and discharges

The distribution of primary charge per incident particle is shown on figure A.8 on the next page for two different gas mixtures. Two series of measurements have been made for each mixtures, leading to different bin sizes in the spectrum, which are accounted for in this plot. The probability density distribution is then obtained by fitting the following function to the data points:

$$\phi(q) = \exp\left[p_0 + p_1 \times \ln(q) + p_2 \times \ln^2(q) + p_3 \times \ln^3(q)\right]$$

where the p_i's are the fit parameters.

Assuming that discharge occurs whenever N_p exceeds R/G, one can now predict the

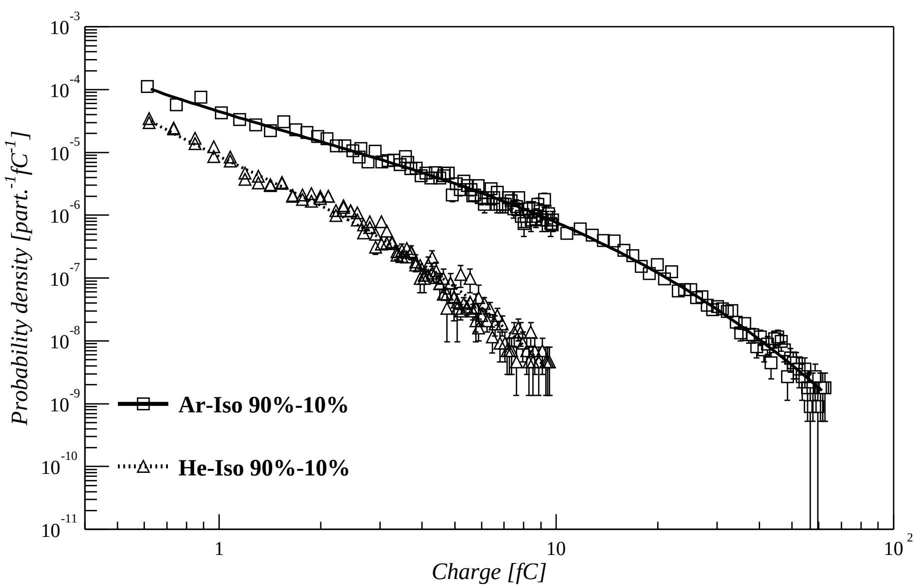

Figure A.8 – *The probability density distribution of the charge per particle deposited in the conversion gap, measured at very low gain. Curves are fitted to the data (see text).*

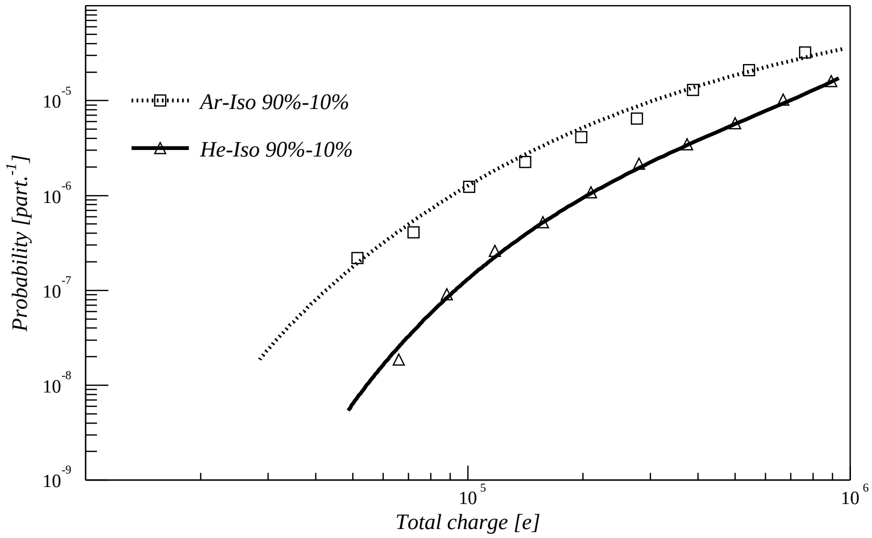

FIGURE A.9 – *Discharge probability per incident pion as a function of the total charge in the electron avalanche induced by the incident particle. Points are measurements; curves are predictions based on the Raether model.*

discharge probability by integrating the fitted $\phi(q)$ distributions. The result is shown on figure A.9, with $R = 1.5 \cdot 10^8$. The agreement between curves and data points indicates that discharges are really induced by highly ionising particles. It should be added that these HIPs cannot come from the tail of the energy loss distribution of minimum ionising particles (MIPs). The measured Landau distribution of MIPs indeed has a negligible rate at such high values. HIPs are therefore believed to come from nuclear reactions of the incident particles with the gas or the chamber material.

A.2.4 Detection efficiency

The detection efficiency of the detector has also been measured for the two gas mixtures. The read-out of the 32 instrumented strips was triggered by scintillators P1 and P2 in coincidence (see figure A.5 on page 105), which also counted the number of incoming particles. Events were analysed off-line: signals with an amplitude of more than 3σ rms noise above the strip-by-strip pedestals were identified as hits. Clusters were then formed and events with at least one cluster were considered to be detected. The efficiency was then roughly calculated by simply dividing the total number of triggers by the number of "detected" events. This crude method was used to estimate the beginning of the efficiency plateau and compare with the previously measured discharge rates. The result of these measurements is shown in figure A.11 on the facing page.

Both mixtures show a very similar efficiency plateau starting around a primary charge of 2×10^5. This corresponds to a discharge probability of about 10^{-6}. Such a high rate at the beginning of the plateau, as compared to other measurements [70] has several explanations. First of all, PSI pions are minimum ionisation particles. In addition, the electronic setup with capacitors coupled to the strips reduces the signal amplitude. And finally, the fast electronics used in these tests induced a high ballistic loss: only a small portion of the total charge deposited was really integrated, because of the drift time of electrons in the conversion space.

Figure A.10 – *Picture of a 1 mm tall spark in a gas chamber [68].*

A.3 Conclusion

Micromegas has been studied as a candidate for LHCb's inner tracking system. In spite of its many features in high intensity beams (mainly speed and robustness), Micromegas showed a large rate of discharge. A detailed study of this phenomenon in MIP beams led to the conclusion that nuclear reactions of incident particles in the detector were causing very high charge deposits which then generated discharges, in agreement with observations made in parallel-plate chambers. Because of this topological drawback, the rate of discharges would be of the order of 100 Hz at LHC, if the conditions of the PSI tests are representative.

Other tests [72] have shown that the discharge rate could be significantly reduced by preamplifying the signal in the conversion region. In the meanwhile, however, silicon microstrip detectors were adopted as the baseline technology for the full LHCb inner tracker.

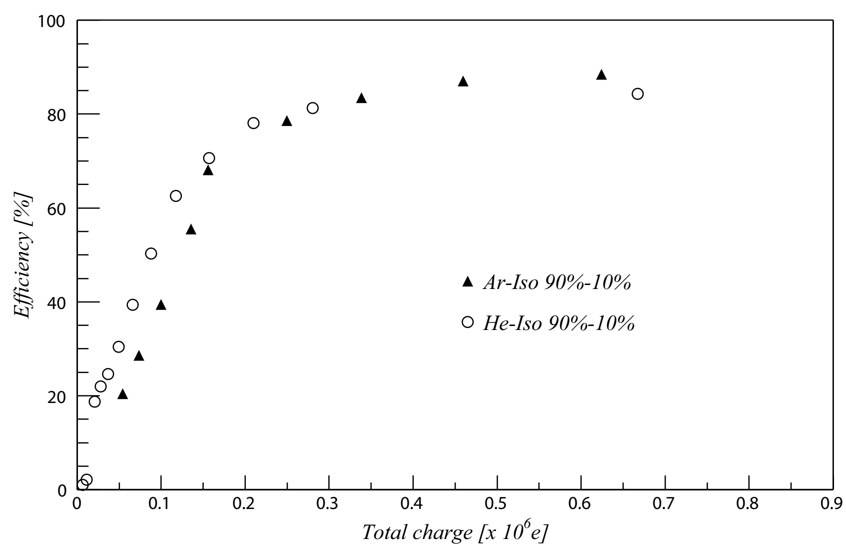

FIGURE A.11 – *Discharge probability as a function of the total charge in an electron avalanche.*

Bibliography

[1] J. H. C , J. W. C , V. L. F , R. T . Evidence for the 2π decay of the K_2^0 meson. *Phys. Rev. Lett.*, 13(4):138–140, July 1964.

[2] F.J. R . Measurement of Δm_d with Belle. *Nucl. Phys. B Proc. Suppl.*, 117:485–488, 2003.

[3] CLEO collaboration, J. B . Two measurements of $B^0\overline{B}^0$ Mixing. *Phys. Rev. Lett.*, 71(11):1680–1684, September 1993.

[4] M.S. S . Measurement of Neutral B meson properties. PhD thesis, Harvard University, May 1995.

[5] I.C. L . Measurement of B^0 Meson Properties. PhD thesis, Virginia Polytechnic Institute and State University, June 1999.

[6] J. B . CP violation, B mixing and B lifetime results from the BaBar experiment. May 2001, hep-ex/0105073, Invited talk at the 36th Rencontres de Moriond on QCD and Hadronic Interactions.

[7] G.C. B , L. L , J.P. S . CP Violation. Oxford University Press, 1999.

[8] O. S . $B^0-\overline{B}^0$ mixing. *Phys. Rev.*, D66(01001), July 2002, in Reference [19].

[9] A. M , M. S , K. A , Y. S . Simulation studies on CP and CPT violation in $B\overline{B}$ mixing. *Phys. Rev.*, D58(036003), July 1998.

[10] V. W E. W . Berechnung der natürlichen Linienbreite auf Grund der Diracschen Lichttheorie. *Zeitschrift für Physik*, 63:54–73, May 1930.

[11] V. W E. W . Über die natürliche Linienbreite in der Strahlung des harmonischen Oszillators. *Zeitschrift für Physik*, 65:18–29, August 1930.

[12] N. C . Unitary symmetry and leptonic decays. *Phys. Rev. Lett.*, 10(12):531–533, June 1963.

[13] M. K T. M . *CP*-Violation in the Renormalizable Theory of Weak Interaction. *Progress of Theoretical Physics*, 49(2):652–657, February 1973.

[14] L. W . Parametrization of the Kobayashi-Maskawa Matrix. *Phys. Rev. Lett.*, 51(21):1945–1947, November 1983.

[15] Z.Z. X . Time dependence of coherent $P^0\overline{P}^0$ decays and CP violation at asymmetric B factories. *Phys. Rev.*, D53(1), January 1996.

[16] CFS collaboration. Observation of a Dimuon Resonance at 9.5 GeV in 400-GeV Proton-Nucleus Collision. *Phys. Rev. Lett.*, 39(5):252–255, August 1977.

[17] S. O . φ-Meson and Unitary Symmetry Model. *Physics Letters*, 5(2):165–168, May 1963.

[18] T. B K. H . B Mesons. *Prog. Part. Nucl. Phys.*, 35:81–220, July 1995.

[19] K. H . (P D G). Review of Particle Physics. *Phys. Rev.*, D66(010001), 2002, and 2003 partial update for edition 2004 (URL: `http://pdg.lbl.gov`).

[20] KEKB B-Factory Design Report. *KEK-Report*, 95–7, 1995, National Laboratory for High Energy Physics.

[21] Belle collaboration, A. A . The Belle detector. *Nucl. Instr. & Meth. in Phys. Res.*, A(479):117–232, 2002.

[22] G. T . The Belle silicon vertex detector: present performance and upgrade plans. *Nucl. Instr. & Meth. in Phys. Res.*, A(501):22–31, 2003.

[23] Y. O . Track parametrization. *Belle note*, 148, June 1997.

[24] B T G . Charged Particle Tracking in Belle. *Belle note*, 327, August 2000.

[25] H. H . A high-resolution cylindrical drift chamber for the KEK B-factory. *Nucl. Instr. & Meth. in Phys. Res.*, A(455):294–304, 2000.

[26] T. I . Aerogel Cherenkov counter for the BELLE detector. *Nucl. Instr. & Meth. in Phys. Res.*, A(453):321–325, 2000.

[27] H. K . The BELLE TOF system. *Nucl. Instr. & Meth. in Phys. Res.*, A(453):315–320, 2000.

[28] K. M . Belle electromagnetic calorimeter. *Nucl. Instr. & Meth. in Phys. Res.*, A(494):298–302, 2002.

[29] A. A . The K_L/μ detector subsystem for the BELLE experiment at the KEK B-factory. *Nucl. Instr. & Meth. in Phys. Res.*, A(449):112–124, 2000.

[30] M.Z. W . Beam test of the BELLE extreme forward calorimeter at KEK. *Nucl. Instr. & Meth. in Phys. Res.*, A(455):319–323, 2000.

[31] Y. U . Development of the central trigger system for the BELLE detector at the KEK B-factory. *Nucl. Instr. & Meth. in Phys. Res.*, A(438):460–471, 1999.

[32] S. N . PANTHER — User's manual —. *Belle note*, 130, November 1996.

[33] F. R . The year 2001 DST production scheme. *Belle note*, 486, November 2001.

[34] QQ — The CLEO event generator. `http://www.lns.cornell.edu/public/CLEO/soft/QQ`.

[35] D.E. G . Review of Particle Physics. *The European Physical Journal*, C15(1), 2000.

[36] A . GEANT — Detector Description and Simulation Tool. *CERN Program Library Long Writeup*, W5013, 1993.

[37] DELPHI collaboration, P. A . Measurement of the $\overline{B} \to D^{(*)}\pi\ell\overline{\nu}_\ell$ branching fraction. *Physics Letters*, B475:407–428, 2000.

[38] B. C . HadronB. *Belle note*, 390, January 2001.

[39] B. C . Measurement of the Number of $B\overline{B}$ Events in Experiment 5 Data and the $B\overline{B}$ Cross Section at KEKB. *Belle note*, 296, March 2000.

[40] G.C. F S. W . Observables for the Analysis of Event Shapes in e^+e^- Annihilation and Other Processes. *Phys. Rev. Lett.*, 41(23):1581–1585, December 1978.

[41] K. H . Electron identification in Belle. *Nucl. Instr. & Meth. in Phys. Res.*, A(485):490–503, 2002.

[42] H. B . Zur Theorie des Durchgangs schneller Korpuskularstrahlen durch Materie. *Ann. d. Physik*, 5:325–400, April 1930.

[43] F. B . Bremsvermögen von Atomen mit mehreren Elektronen. *Zeitschrift für Physik*, 81:363–376, December 1932.

[44] A. A . Muon identification in the Belle experiment at KEKB. *Nucl. Instr. & Meth. in Phys. Res.*, A(491):69–82, 2002.

[45] N. H . Neutral B meson mixing and CPT violation with the Belle Experiment. PhD thesis, University of Melbourne, September 2002.

[46] J. T . Kinematic Fitting. *Belle note*, 194, 1998.

[47] J. T . Kfitter Usage and Effect. *Belle note*, 193, 2000.

[48] R. B C. B . Fitting using finite Monte Carlo Samples. *Comp. Phys. Comm.*, (77):219, 1993.

[49] H. T . Proper-time Resolution Function for Measurement of Time Evolution of B Mesons at the KEK B-Factory. January 2003, hep-ex/0301026, submitted to *Nucl. Instr. and Meth.* A.

[50] H F A G (HFAG). URL: `http://www.slac.stanford.edu/xorg/hfag/`.

[51] F.J. R . Advances in Δm_d measurements. *ECONF*, C0304052:WG210, 2003, hep-ex/0306061, Invited talk at 2nd Workshop on the CKM Unitarity Triangle, Durham, England, 5-9 Apr 2003.

[52] BABAR collaboration, A. A . Measurement of $B^0 - \overline{B}^0$ Flavor Oscillation in Hadronic B^0 Decays. *Phys. Rev. Lett.*, 88(221802), 2002.

[53] Belle collaboration, T. T . Measurement of the oscillation frequency for $B^0 - \overline{B}^0$ mixing using hadronic B^0 decays. *Phys. Lett.*, B542:207–215, 2002.

[54] BABAR collaboration, B. A . Simultaneous measurement of the B^0 meson lifetime and mixing frequency with $B^0 \to D^{*-}\ell^+\nu_\ell$ decays. *Phys. Rev.*, D67:072002, 2003.

[55] Belle collaboration, K. H , M. H , . Measurement of the $B^0 - \overline{B}^0$ mixing parameter Δm_d using semileptonic B^0 decays. *Phys. Rev. Lett.*, 89(25):251803, December 2002.

[56] BABAR collaboration, B. A . Measurement of the $B^0 - \overline{B}^0$ oscillation frequency with inclusive dilepton events. *Phys. Rev. Lett.*, 88(22):221803, 2002.

[57] Belle collaboration, N.C. H . Studies of $B^0 - \overline{B}^0$ mixing properties with inclusive dilepton events. *Phys. Rev.*, D67:052004, 2003.

[58] Belle collaboration, Y. Z . Measurement of the $B^0 - \overline{B}^0$ mixing rate with $B^0(\overline{B}^0) \to D^{*\mp}\pi^\pm$ partial reconstruction. *Phys. Rev.*, D67:092004, 2003.

[59] Belle collaboration, K. A . Evidence for CP-violating asymmetries in $B^0 \to \pi^+\pi^-$ decays and constraints on the CKM angle ϕ_2. *Phys. Rev.*, D68(012001), 2003.

[60] D. B . Status of the computation of $f_{B_{s,d}}$, ξ and $\hat{g}$. April 2003, hep-ph/0310072.

[61] BABAR collaboration, B. A . Limits on the Decay-Rate Difference of Neutral B Mesons and on CP, T, and CPT Violation in $B^0\overline{B}^0$ Oscillations. November 2003, hep-ex/0311037.

[62] Y. G . MICROMEGAS: a high-granularity position-sensitive gaseous detector for high particle-flux environment. *Nucl. Instr. & Meth. in Phys. Res.*, A(387):88–91, 1996.

[63] P. G . Identification of solar neutrinos by individual electron counting in HELLAZ. *Nucl. Instr. & Meth. in Phys. Res.*, A(433)1–2:554–559, August 1999.

[64] S. A . Experimental studies of a Micromegas neutron detector. *Nucl. Instr. & Meth. in Phys. Res.*, A(481)1–3:120–129, April 2002.

[65] A. M . Tracking with 40x40 cm^2 Micromegas detectors in the high energy, high luminosity C experiment. *Nucl. Instr. & Meth. in Phys. Res.*, A(478)1–2:210–214, February 2002.

[66] Maxwell and HFSS at Cern. URL: `http://wwwinfo.cern.ch/ce/ae/Maxwell/`.

[67] R V . Garfield, a drift-chamber simulation program. *Cern Program Library*, W5050, 1999.

[68] H. R . Electron Avalanches and Breakdown in Gases. Butterworths, London, 1964.

[69] J. D ´, Y. G , H. Z , A. B , J.-P. P , F.R . Spatial resolution in Micromegas detectors. *Nucl. Instr. & Meth. in Phys. Res.*, A(459)3:523–531, March 2001.

[70] A. B , J.-P. P , F. R , J. D ´, Y. G , A. D , Y. P - . Study of sparking in Micromegas chambers. *Nucl. Instr. & Meth. in Phys. Res.*, A(488)1–2:162–174, August 2002.

[71] P. J . A transimpedance amplifier using a novel current mode feedback loop. *Nucl. Instr. & Meth. in Phys. Res.*, A(377)2–3:435–439, August 1996.

[72] A. D . Performance of Micromegas with preamplification at high intensity hadron beams. *Nucl. Instr. & Meth. in Phys. Res.*, A(478)1–2:205–209, February 2002.

[73] J.P. P F. R . PSI run report of the Micromegas detector, March 28 – April 13 1999. *LHCb note*, LHCb 99-029, 1999.

[74] LHCb collaboration. LHCb Inner Tracker Technical Design Report. *CERN/LHCC*, 2002(029), November 2002.

[75] V. Z . The luminosity measurement at the Belle detector. *Nucl. Instr. & Meth. in Phys. Res.*, A(494):63–67, 2002.